

997680

**DAHLGREN DIVISION
NAVAL SURFACE WARFARE CENTER**

Dahlgren, Virginia 22448-5100



NSWCDD/TR-94/156

NSWC/DL TECHNICAL LIBRARY



2000350172

**COMPUTATIONS AND EXPERIMENTS OF
SHALLOW DEPTH EXPLOSION PLUMES**

**BY W. G. SZYMCZAK
SYSTEMS RESEARCH AND TECHNOLOGY DEPARTMENT**

**J. M. SOLOMON
ENIG ASSOCIATES, INC.**

AUGUST 1996

Approved for public release; distribution is unlimited.

NSWCDD-TR-94-156

Report Documentation Page			Form Approved OMB No. 0704-0188		
Public reporting burden for the collection of information is estimated to average 1 hour per response, including the time for reviewing instructions, searching existing data sources, gathering and maintaining the data needed, and completing and reviewing the collection of information. Send comments regarding this burden estimate or any other aspect of this collection of information, including suggestions for reducing this burden, to Washington Headquarters Services, Directorate for Information Operations and Reports, 1215 Jefferson Davis Highway, Suite 1204, Arlington VA 22202-4302. Respondents should be aware that notwithstanding any other provision of law, no person shall be subject to a penalty for failing to comply with a collection of information if it does not display a currently valid OMB control number.					
1. REPORT DATE AUG 1996		2. REPORT TYPE		3. DATES COVERED 00-00-1996 to 00-00-1996	
4. TITLE AND SUBTITLE Computations and Experiments of Shallow Depth Explosion Plumes			5a. CONTRACT NUMBER		
			5b. GRANT NUMBER		
			5c. PROGRAM ELEMENT NUMBER		
6. AUTHOR(S)			5d. PROJECT NUMBER		
			5e. TASK NUMBER		
			5f. WORK UNIT NUMBER		
7. PERFORMING ORGANIZATION NAME(S) AND ADDRESS(ES) Dahlgren Division,Naval Surface Warfare Center,Dahlgren,VA,22448-5100			8. PERFORMING ORGANIZATION REPORT NUMBER		
9. SPONSORING/MONITORING AGENCY NAME(S) AND ADDRESS(ES)			10. SPONSOR/MONITOR'S ACRONYM(S)		
			11. SPONSOR/MONITOR'S REPORT NUMBER(S)		
12. DISTRIBUTION/AVAILABILITY STATEMENT Approved for public release; distribution unlimited					
13. SUPPLEMENTARY NOTES					
14. ABSTRACT					
15. SUBJECT TERMS					
16. SECURITY CLASSIFICATION OF:			17. LIMITATION OF ABSTRACT Same as Report (SAR)	18. NUMBER OF PAGES 87	19a. NAME OF RESPONSIBLE PERSON
a. REPORT unclassified	b. ABSTRACT unclassified	c. THIS PAGE unclassified			

FOREWORD

This report was prepared in support of the Water Barrier Ship Self-Defense Concept, managed by C. E. Higdon of the Naval Surface Warfare Center, Dahlgren Division (NSWCDD), Dahlgren, Virginia, Code G42. Under the sponsorship of the Office of Naval Research (ONR), Arlington, Virginia, the Center is developing technology that has the potential to be very effective in defending Navy platforms against high speed low flying antiship missiles (ASMs). The concept uses a wall of water to provide a low cost, universal terminal defense system for ships. The wall of water or *water barrier* is formed from the shallow detonations of multiple underwater explosives to protect the ship from attacking ASMs. This concept can be employed to slow or stop debris and warhead fragments from missiles killed at very short range to preclude significant damage to the defending ship. Furthermore, the barrier would defeat the fuzing and structure of ASMs that have penetrated the inner self-defense layer.

The main thrust of this report is to provide validations of a hydrodynamics computer code for predicting explosion plume behavior. The results of experiments conducted at NSWC Carderock Division, Bethesda, Maryland, in May 1993, at a quarry in Arvon, Virginia in August 1994, and at the Briar Point facility of the Aberdeen Proving Grounds in June 1994, are used for the validation studies.

The research in this paper related to the Water Barrier Ship Self-Defense Concept was supported by D. Siegal (ONR, Code 351). The basic research required for the development of the computational method and some of the theory presented was supported, in part, by R. Lau (ONR, Code 311) and the NSWC Independent Research (IR) fund.

In addition to the sponsors of this research, the authors would like to acknowledge the work of J. Connor (NSWC Indian Head (IH) 9540A) for providing plume height measurements and underwater bubble and plume profiles; K. Boulais, J. Choe, and K. Erwin (NSWCDD, B42) for providing the microwave data measurements; and L. Lipton (NSWCIIH 450) for providing the density probe data. We also thank S. L. Drinnon (NSWCDD, B44) for assisting in preparing the presented data and to J. C. W. Rogers of the Polytechnic University, Brooklyn, New York, who provided insight into some aspects of the spherical bubble theory presented in Chapter 3 of this report. We are also grateful to G. Harris (NSWCIIH 460) and G. Young for providing some of the important technical reports listed in the references. Finally, the authors thank C. E. Higdon for not only presenting the problem and managing the effort, but also for proofreading this report.

This report has been reviewed by Tse-Fou Zien, Head, Advanced System Research and Technology Group.

Approved by:



MARY E. LACEY, Head
Systems Research and Technology Department

ABSTRACT

A mathematical model and computational code are validated for predicting shallow depth explosion plume behavior. The model is based on a generalized formulation of hydrodynamics and uses an incompressible liquid assumption. This formulation is well suited for predicting long-time bubble and plume dynamics. Initial conditions for the model are derived from spherically symmetric bubble theory, combined with empirical measurements. The effects of the spray dome caused by the reflection of the initial shock wave off the free surface is modeled empirically as a recess in the surface above the charge. Comparisons to photographs of experiments provide qualitative agreement. Quantitative measurements of plume heights and plume densities using conductivity probes and microwave absorption are also compared to the computational data. Results for both single- and multiple-charge shots are included.

CONTENTS

<u>Chapter</u>		<u>Page</u>
1	INTRODUCTION	1-1
2	THE NUMERICAL METHOD	2-1
	COMPUTATIONAL MODEL	2-1
3	BUBBLE THEORY AND BENCHMARK COMPUTATIONS	3-1
	SPHERICAL BUBBLE THEORY	3-1
	NUMERICAL ACCURACY AND CONVERGENCE	3-2
	EMPIRICAL RELATIONS AND APPROXIMATIONS	3-3
	FREE SURFACE EFFECTS	3-10
	NEW BUBBLE PARAMETERS	3-15
	SPARK BUBBLE COMPARISONS	3-18
4	COMPARISONS TO EXPERIMENTS	4-1
	COMPUTATIONAL GRIDS	4-2
	BUBBLE PROFILE COMPARISONS	4-4
	PLUME COMPARISONS	4-4
	MICROWAVE COMPARISONS	4-8
	DENSITY PROBE COMPARISONS	4-12
5	SUMMARY AND CONCLUSIONS	5-1
6	REFERENCES	6-1
	DISTRIBUTION	(1)

ILLUSTRATIONS

<u>Figure</u>	<u>Page</u>
3-1 DEPENDENCE OF THE RADIUS RATIO ON THE DEPTH WITH $\gamma = 1.3$ AND VARIOUS VALUES OF N_∞	3-20
3-2 RATIO BETWEEN THE RADIUS CONSTANT J_∞ AND $J_\alpha(d)$ WITH $\gamma = 1.3$ FOR VARIOUS VALUES OF N_∞	3-20
3-3 MEASURED VALUES OF J AND J_∞ FOR TNT CHARGES AT DIFFERENT DEPTHS	3-21
3-4 MEASURED AND THEORETICAL VALUES OF K FOR TNT CHARGES AT DIFFERENT DEPTHS	3-22
3-5 THEORETICALLY DETERMINED VALUES OF K_α AS A FUNCTION OF q FOR VARIOUS VALUES OF γ	3-23
3-6 DEPENDENCE OF J_∞ ON q FOR VARIOUS VALUES OF γ (BASED ON A VALUE A_{\max} MEASURED AT $d = 300$ FT)	3-23
3-7 COMPARISON OF THEORY TO COMPUTATIONS OF FREE SURFACE EFFECTS ON THE PERIOD IN THE ABSENCE OF GRAVITY	3-24
3-8 COMPUTATED EFFECTS OF THE FREE SURFACE ON THE MAXIMUM EQUIVALENT BUBBLE RADIUS IN THE ABSENCE OF GRAVITY	3-24
3-9 SPARK BUBBLE AT SCALED DEPTH $C = 0.56$	3-25
3-10 GRID SIZE EFFECTS ON DENSITY CONTOURS	3-26
3-11 COMPUTED AND MEASURED PLUME HEIGHTS FOR THE $C = 0.56$ SPARK BUBBLE	3-27
4-1 COMPARISON OF COMPUTED AND MEASURED BUBBLE AND PLUME OUTLINES FOR SHOT CD-9 AT TIME $t = 0.10$ SEC	4-16
4-2 COMPARISON OF COMPUTED AND MEASURED BUBBLE AND PLUME OUTLINES FOR SHOT CD-10 AT TIME $t = 0.10$ SEC FOR DIFFERENT VALUES OF ϵ_A	4-17
4-3 COMPUTED AND MEASURED PLUME HEIGHTS FOR CARDEROCK TEST POND SHOTS CD-9, CD-10, AND CD-13	4-18
4-4 COMPUTED AND MEASURED PLUME HEIGHTS FOR ARVONIA SHOTS ARV-1 AND ARV-2	4-19
4-5 COMPUTED PLUME FORMATIONS FOR ARVONIA SHOT ARV-1 USING AN INITIALLY RECESSED AND FLAT FREE SURFACE	4-20

ILLUSTRATIONS (Continued)

<u>Figure</u>		<u>Page</u>
4-6	COMPUTED AND MEASURED PLUME HEIGHTS FOR BRIAR POINT SHOTS BP-8 AND BP-9	4-21
4-7	COMPUTED AND MEASURED PLUME HEIGHTS FOR BRIAR POINT SHOTS BP-12 AND BP-14	4-22
4-8	PHOTOGRAPHS AND COMPUTATIONS OF SHOT BP-12	4-23
4-9	PHOTOGRAPHS AND COMPUTATIONS OF SHOT BP-14	4-24
4-10	EMPIRICAL MODEL OF SURFACE SHOCK EFFECTS FOR MULTIPLE CHARGE CONFIGURATIONS	4-25
4-11	PHOTOGRAPHS AND COMPUTATIONS OF SHOT BP-8	4-26
4-12	PHOTOGRAPHS AND COMPUTATIONS OF SHOT BP-9	4-27
4-13	MEASURED AND COMPUTED MICROWAVE DATA FOR SHOT ARV-1	4-28
4-14	MEASURED AND COMPUTED MICROWAVE DATA FOR SHOT ARV-2	4-28
4-15	MEASURED AND COMPUTED MICROWAVE DATA FOR MULTIPLE CHARGE SHOT ARV-3	4-29
4-16	MEASURED AND COMPUTED MICROWAVE DATA FOR SHOT BP-8 AT HEIGHTS OF 25 AND 12.5 FT	4-30
4-17	MEASURED AND COMPUTED MICROWAVE DATA FOR SHOT BP-9 AT HEIGHTS OF 25 AND 12.5 FT	4-31
4-18	MEASURED AND COMPUTED MICROWAVE DATA FOR MULTIPLE CHARGE SHOT BP-12 AT HEIGHTS OF 25 AND 12.5 FT	4-32
4-19	MEASURED AND COMPUTED MICROWAVE DATA FOR MULTIPLE CHARGE SHOT BP-14 AT HEIGHTS OF 25 AND 12.5 FT	4-33
4-20	INTEGRATED PROBE DATA FOR SHOT ARV-1	4-34
4-21	INTEGRATED PROBE DATA FOR SHOT ARV-2	4-34
4-22	INTEGRATED PROBE DATA FOR SHOT ARV-3	4-35
4-23	INTEGRATED PROBE DATA FOR SHOT BP-8	4-36
4-24	INTEGRATED PROBE DATA FOR SHOT BP-9	4-36
4-25	INTEGRATED PROBE DATA FOR SHOT BP-12	4-37
4-26	INTEGRATED PROBE DATA FOR SHOT BP-14	4-37

CHAPTER 1

INTRODUCTION

During the past 50 years a large amount of research has been focused on the phenomenon of plumes generated by underwater explosions. Reviews of much of this work can be found in the book by Cole,¹ and the reports of Young.^{2,3} These references provide observations and empirical formulas for large charges, which describe the general shape of the resulting plume, in particular, its height and width. Photographs of shallow depth spark induced bubbles presented by Blake and Gibson,⁴ clearly show a water jet rising above the surface during the first collapse of the bubble. Some interesting experiments were performed by Kedrinskii,⁵ who suspended an inverted flask with a "trap" above small charges and measured the total amount of water in the jets produced as a function of the charge depth. Besides this, very little is known quantitatively about the total amount of water in the plume as well as the structure of the plume. The lack of detailed plume knowledge is due primarily to the opaqueness of the spray caused by the initial "spalling" of the surface from the shock and the breakup of the ejected plumes. It is also due in part to a lack of efficient and robust computational procedures capable of predicting this complex phenomenon. The purpose of this report is to begin to provide details of the plume structure using both experimental measurements as well as computational predictions.

As described by Cole,¹ and updated with a more complete understanding by Snay⁶ and Kedrinskii,⁵ there are several distinct, but interrelated phenomena typical to shallow depth explosions. Upon detonation of the explosive, a spherical shock wave moving away from the charge is emitted. This wave reflects off the surface as a rarefaction wave which travels back down through the gas globe of detonation products. Due to the tension created behind the rarefaction wave, cavitation can occur and some of the water can be spalled upwards, creating a "spray dome." It is the height and width of this spray dome or "cupola" that is empirically fit to data by Kelsky et al.⁷ and Young,² at least at the early times.

The greatest interest of this report is the eruption of vertical and radial plumes caused by the dynamics of the pulsating bubble. This phase of the problem has also been controversial in conjectures of its cause, structure, and density. In particular, consider the case when the scaled depth $C = \frac{d}{A_{\max}}$, where d is the depth and A_{\max} is the maximum bubble radius, is less than one. Through the use of potential flow theory, as well as photographic evidence of spark bubbles (in which there are little or no shock effects), it has been clearly demonstrated that the initial or primary plume consists of a central column made up almost entirely of water rising above the surface.^{4,5,6,8} For large explosives, the velocity of the liquid jet rising above the surface has been

underpredicted by potential flow procedures. This discrepancy is very likely due to the initial spallation of the water which leaves an indentation in the liquid surface above the bubble. Potential flow theory has also shown that when an indented surface is assumed for the initial condition then the jet is intensified in its velocity.⁵

For values of $C > 0.5$, it has been observed that in the case of spark generated bubbles, the free surface is not broached by the bubble during its first complete pulsation.⁴ Secondary plumes ejected radially above the surface after the bubble collapse have been also been observed and are due to the second expansion of the bubble, which at this time forms an annular region.³ It will be demonstrated in this report that these secondary plumes can be reliably simulated by our computational method.

This report contains data from small-scale explosion tests performed at the Naval Surface Warfare Center - Carderock Division (NSWCDD), Bethesda, Maryland, Test Pond in May 1993, and at larger scales at Hi-Test Laboratories in a quarry in Arvon, Virginia in August 1993, and at the Briar Point facility of the Aberdeen Proving Grounds, Aberdeen, Maryland, in June 1994. The Carderock tests were photographed with cameras both above and below the surface of the water, so that the motion of the bubble could be observed in conjunction with the plume formation. Data from the Arvon and Aberdeen tests came not only from above surface photographs, but also from conductivity probes (held up by cables above the charges) and microwave absorption measurements through the plumes. In addition to using these measurements to demonstrate the feasibility of using the plume as an effective barrier, they are used to provide benchmark comparisons for validating numerical simulations.

A description of the numerical code used for the plume predictions is given in Chapter 2. The validity of the code on various benchmark problems is presented in Chapter 3 including a comparison of the computations to the photographs of spark bubble experiments from Reference 4. Some theory of underwater bubbles and the effects of the free surface are also given. This theory is used together with shallow-depth period and bubble-size measurements to derive empirical parameters for the charge types under consideration. These new parameters are more consistent with the observed data and can be expected to provide for more accurate initial conditions. Comparisons to the measured data together with the results of the numerical simulations are presented in Chapter 4. A brief summary of the results and conclusions is contained in Chapter 5.

CHAPTER 2

THE NUMERICAL METHOD

The numerical simulations used in this study were produced using the code *BUB2D* for both axially symmetric and two-dimensional problems. Both codes use an incompressible assumption for the regions containing water. One advantage of such an approach is that the time-step limitation is based only on the fluid velocity as compared to compressible formulations that have time-step limitations based on the much higher speed of sound of the water. This is particularly important for plume predictions since the dynamics of interest (formation rise and fall of the plume) occur on the order of seconds. The disadvantage of an incompressible approach is that the early time shock effects, in particular, the early time dome of spray ejected upward as a result of the shock reflecting off the surface, is not predicted.

COMPUTATIONAL MODEL

The computational model used in both the two- and three-dimensional codes is based on a generalized formulation of hydrodynamics.⁹⁻¹² This formulation uses a fixed spatial domain Ω , where the density ρ , velocity \mathbf{u} , and the pressure P are governed by the mass and momentum conservation equations

$$\rho_t + \nabla \cdot (\rho \mathbf{u}) = 0, \quad (2-1a)$$

$$(\rho \mathbf{u})_t + \nabla \cdot (\rho \mathbf{u} \mathbf{u}) = -\rho g \mathbf{k} - \nabla P, \quad (2-1b)$$

subject to the constraint

$$\rho \leq \rho_0. \quad (2-1c)$$

where g the gravitational constant, $-\mathbf{k}$ the unit vector in the direction of the gravitational force, and ρ_0 is the constant density of the incompressible liquid. In constructing solutions for the constrained system (2-1), it is assumed that liquid-on-liquid collisions behave inelastically, thereby causing a reduction in the total mechanical energy of the flow field. These energy losses are associated with breakdowns of the classical theory and may be attributed to turbulence.¹³

The density field divides Ω into two time-varying regions, namely, the *liquid region* $D(t) = \{\mathbf{x} \in \Omega: \rho(\mathbf{x}, t) = \rho_0\}$, and the *nonliquid region* where $\rho < \rho_0$. The interfaces separating these regions are the free surfaces. The numerical solution "captures" these surfaces as slightly smeared interfaces. The nonliquid regions are characterized by specifying uniform pressures in each of its connected subsets. For example, in the atmospheric region above the liquid the pressure is set to the

ambient air pressure. In an underwater bubble the pressure P_B may be determined using the adiabatic law

$$P_B = CV_B^{-\gamma}, \quad (2-2)$$

where V_B is the instantaneous bubble volume, C is a constant, and γ is the ratio of specific heats of the bubble gases.

Assume that the density and velocity, ρ^n, \mathbf{u}^n at time step n , and the pressure gradient at the previous half step, $\nabla P^{n-1/2}$ are known. This solution is evolved using the following three step time split procedure.

Convection

The solution is first advanced

$$(\rho^n, \mathbf{u}^n) \rightarrow (\tilde{\rho}, \tilde{\mathbf{u}})$$

by "solving" the conservation laws (2-1a,b) without including the ∇P term on the right-hand side of (2-1b) and without regard to the constraint (2-1c). This step is implemented numerically using a formally second-order Godunov-type method, which uses slope limiting in space and explicit predictor-corrector time stepping.

Redistribution of Density and Momenta

Next, the density and momenta are redistributed

$$(\tilde{\rho}, \tilde{\mathbf{u}}) \rightarrow (\bar{\rho}, \bar{\mathbf{u}})$$

so that the constraint (2-1c) is satisfied, the global conservation of mass and momenta are maintained, and the energy is nonincreasing. This step is of critical importance to the stability and convergence of the overall algorithm.¹⁴ The density is redistributed using an approximate solution to an obstacle problem. This solution is obtained using a constrained direction preconditioned conjugate gradient method. The momenta redistributions are determined as solutions of two elliptic self-adjoint problems. Discretizations of these problems yield systems of linear equations with diagonally dominant matrices, which are efficiently solved using a diagonally preconditioned conjugate gradient method. After this step, $\bar{\rho} = \rho^{n+1}$ and the new nonliquid region is then determined along with the pressure in each of its connected subsets. In the computational space the new liquid region, $\mathbf{D}^{n+1} = \mathbf{D}(t^{n+1})$, is defined to be the collection of grid cells $C_{i,j}$ such that

$$\rho_{i,j}^{n+1} \geq (1 - \epsilon_p) \rho_0, \quad (2-3a)$$

where $\rho_{i,j}^{n+1}$ is the density in cell $C_{i,j}$. A typical value used for ϵ_p is 0.04.

When computing shallow depth bubble dynamics, it was found that because of thin layers of water between the bubble and the air surfaces when the bubble is near its maximum volume, a value $\epsilon_p = 0.04$ would cause the bubble to "vent" into the air prematurely unless the grid size was excessively small. This situation was remedied by including an additional factor, ϵ_A . All cells $C_{i,j}$, that are adjacent to "air" cells are also included in the liquid region \mathbf{D}^{n+1} if

$$\rho_{i,j}^{n+1} \geq (1-\epsilon_A)\rho_0. \quad (2-3b)$$

A typical value used for ϵ_A is 0.5. Generally, this value was used for first 80 percent of the duration of the first bubble cycle. After this time, the value of ϵ_A would be reduced to 0.1. This was found to improve stability, as monitored by computing the total energy at each time step, for the long-time bubble dynamics.

After the redistribution step $\bar{\mathbf{u}} = \mathbf{u}^{n+1}$ in the new nonliquid region. However, $\bar{\mathbf{u}}$ is not consistent with (2-1b) in the new liquid region.

Pressure Projection

In this step the velocity is corrected

$$\bar{\mathbf{u}} \rightarrow \mathbf{u}^{n+1}$$

using the gradient of the new pressure, $P^{n+1/2}$. The pressure $P = P^{n+1/2}$ is the solution of

$$\tau \nabla \cdot \frac{1}{\rho^{n+1}} \nabla P = \nabla \cdot \bar{\mathbf{u}} \quad \text{in } \mathbf{D}^{n+1} \quad (2-4)$$

where τ is the time step. This equation is discretized using a finite element method with bilinear elements and the resulting linear system is solved using an incomplete Cholesky preconditioned conjugate gradient method. The new velocity

$$\mathbf{u}^{n+1} = \bar{\mathbf{u}} - \frac{\tau \nabla P^{n+1/2}}{\rho^{n+1}} \quad (2-5)$$

is divergence free in \mathbf{D}^{n+1} and thus is consistent with (2-1b).

To determine the pressure uniquely using (2-4), boundary conditions must be specified. On those portions of the boundary of \mathbf{D}^{n+1} that correspond to "wall" boundaries of Ω a Neumann condition is specified, namely

$$\tau \frac{\partial P}{\partial \mathbf{n}} = \rho^{n+1} \bar{\mathbf{u}} \cdot \mathbf{n}.$$

Note that this condition, together with (2-5), implies that $\mathbf{u}^{n+1} \cdot \mathbf{n} = 0$ along wall boundaries.

Multiple Bubble Logic

Dirichlet conditions on the pressure are specified along all boundaries of the nonliquid regions. This specification is complicated by the fact that there can be several different types of nonliquid regions that evolve with time. As mentioned earlier, the nonliquid regions can be designated as either "air" \mathbf{A} or "bubble" \mathbf{B} having specified pressures P_A and P_B , respectively. The air pressure P_A is assumed to be constant for all time. It is possible that the bubble region may become disconnected and in general we have

$$\mathbf{B}^n = \bigcup_{k=1}^{K^n} \mathbf{B}_k^n$$

where K^n is the number of distinct bubbles at time step n , and B_k^n denotes the disjoint connected region comprising bubble k at time step n . Each of these bubbles can have a different pressure P_k^n , and as long as these regions remain distinct, each bubble is assumed to behave adiabatically. When a bubble splits into two disjoint regions, say, $B_k^n \rightarrow B_l^{n+1} \cup B_m^{n+1}$, the pressure $P_l^{n+1} = P_m^{n+1}$ is computed assuming the volume changes occurred before the split, that is,

$$P_l^{n+1} = P_m^{n+1} = \frac{P_k^n (V_k^n)^\gamma}{(V_l^{n+1} + V_m^{n+1})^\gamma}.$$

Similarly, if two disjoint bubbles merge into a single connected region, say, $B_l^n \cup B_m^n \rightarrow B_k^{n+1}$ the new pressure is given by

$$P_k^{n+1} = \frac{(P_l^n V_l^n + P_m^n V_m^n)(V_l^n + V_m^n)^{\gamma-1}}{(V_k^{n+1})^\gamma}.$$

These formulas are easily extendible to general cases treating any finite number of bubbles merging and splitting.^{11,12} Note that whenever merging occurs the pressure of the new connected region changes instantaneously. Similarly, whenever a bubble comes in contact with the air region, the bubble is said to "vent" into the air and the pressure is instantaneously changed into the air pressure. This is obviously a crude approximation to what is physically occurring where the venting takes a finite amount of time, or the bubbles can partially vent. Nevertheless, as long as the venting process is not the critical phenomenon being studied, we can still hope to produce reasonable simulations to shallow depth explosion bubbles.

Another capability of the algorithm is the ability to predict the inception of cavitation.¹⁵ This is accomplished by adding another constraint, $P \geq P_C$ to (2-1), where P_C is a prescribed cavitation pressure. In this case, (2-4) is replaced by an obstacle problem for the pressure. In regions where $P = P_C$, and $\rho = \rho_0$, the divergence of the velocity can be positive. In such regions, it follows from (2-1a) that the density can decrease. When this occurs, and $\rho_{i,j}^{n+1} < (1-\epsilon_\rho)\rho_0$ the cell is designated as part of the "cavitation" region C. However, because of truncation error, it is also possible that $\bar{\rho}_{i,j} < (1-\epsilon_\rho)\rho_0$, while $P > P_C$ in the interior of the water region. This is referred to as "numerical cavitation" and is suppressed by simply setting $\rho_{i,j}^{n+1} = (1-\epsilon_\rho)\rho_0$ in the redistribution step. Although this step violates conservation of mass, it reduces the truncation error in the incompressible water region. For the computations presented in this study, the total percentage of mass added per bubble period was only about 0.005 percent.

CHAPTER 3

BUBBLE THEORY AND BENCHMARK COMPUTATIONS

This chapter presents the basic theory for underwater bubbles based on an incompressible liquid assumption, as well as the empirical formulas used to predict bubbles from different explosives. The empirical formulas are examined carefully since they represent approximations that are valid for moderately deep charges only. Some background information on the properties of our computational algorithm and a convergence study is also presented. Theoretical corrections to the bubble period in the proximity of the free surface are compared to computational results and provide an additional validation of our code for predicting free surface effects. Theory is presented which shows that with an incompressible water model and an adiabatic gas bubble, the maximum volume of the bubble will be reduced as the bubble is moved closer to the free surface in the absence of gravity. An empirical formula for the volume reduction is provided based on the computational results. The theory is also used in combination with bubble period and maximum size measurements to determine new bubble parameters. These new parameters are more consistent with shallow depth observations, than parameters derived from deeper charges. Finally, a comparison to an experiment performed by Blake and Gibson⁴ is used as a validation of the computational predictions of the detailed behavior of the plume formation and bubble collapse.

SPHERICAL BUBBLE THEORY

The equation of motion for a spherical bubble in an infinite incompressible medium, often referred to as the Rayleigh-Plesset equation,¹ is given by

$$a\ddot{a} + \frac{3}{2}\dot{a}^2 = \frac{1}{\rho_0}(P_B - P_\infty) \quad (3-1)$$

where $a = a(t)$ is the bubble radius at time t , $P_B = P_B(t)$ is the bubble pressure at time t , P_∞ is the pressure at infinity, and ρ_0 is the constant density of the incompressible medium. This equation can be derived from the conservation equations (2-1a,b) in the liquid region. Given an initial radius A^0 and an initial bubble pressure P_B^0 , the pressure at later times can be derived using the adiabatic assumption (2-2),

$$P_B(t) = \frac{P_B^0 (A^0)^{3\gamma}}{(a(t))^{3\gamma}}.$$

Let

$$\alpha = \frac{A_{\max}}{A_{\min}} \quad (3-2)$$

be the ratio of maximum to minimum bubble radii. If initially the bubble is at rest ($\dot{a}(0) = 0$) and $a(0) = A^0 = A_{\min}$, an integration of (3-1) yields

$$P_B^0 = P_{\infty}(1-\gamma) \left[\frac{1-\alpha^3}{1-\alpha^{3(1-\gamma)}} \right]. \quad (3-3)$$

Solutions to (3-1) are periodic and the period T_{∞} can be determined (e.g., Friedman¹⁶) using

$$T_{\infty} = 2I_1 \left(\frac{2}{3\rho_0} \right)^{-5/6} (2\pi\rho_0)^{-1/3} \frac{E^{1/3}}{P_{\infty}^{5/6}} \quad (3-4a)$$

where

$$I_1 = \int_{a_0}^{a_1} \frac{a^{3/2} da}{\sqrt{1 - a^3 - ka^{-3(\gamma-1)}}}, \quad (3-4b)$$

$$a_0 = \frac{A_{\min}}{L}, \quad a_1 = \frac{A_{\max}}{L} \quad (3-4c)$$

$$L = A_{\min} \left[1 + \frac{P_B^0}{P_{\infty}(\gamma-1)} \right]^{1/3}, \quad k = \frac{P_B^0}{P_{\infty}(\gamma-1)} \left[\frac{A_{\min}}{L} \right]^{3\gamma}, \quad (3-4d)$$

and

$$E = \frac{4\pi}{3} A_{\min}^3 \left[P_{\infty} + \frac{P_B^0}{\gamma-1} \right]. \quad (3-4e)$$

In the above, a_0 and a_1 are the nondimensionalized minimum and maximum radii and correspond to the roots of the denominator in the integrand of (3-4b), L is the length factor and E is the total energy.

NUMERICAL ACCURACY AND CONVERGENCE

The first set of benchmark computations are comparisons to the solution of a spherically symmetric bubble. For this test, the code *BUB2D* was used with the acceleration due to gravity set to zero, together with the assumption that the bubble gas is adiabatic ($\gamma = 1.3$). The initial conditions used were

$$A^0 = 1.0, \quad \frac{P_B^0}{P_{\infty}} = 342.864, \quad (3-5a)$$

which corresponds to the "free field" value $A_{\max} = 10$. Furthermore, we used

$$P_{\infty} = 10, \quad \rho_0 = 0.031081, \quad (3-5b)$$

so that the free field period is $T_{\infty} = 1.068407$. This value was determined by both using an adaptive Runge-Kutta 4-5 method¹⁷ with a tolerance of 10^{-10} , on problem (3-1) directly, as well as by using (3-4a) with the integral (3-4b) computed using the midpoint rule with repeated Richardson

extrapolation. Since the integrand has a singularity, the error of the midpoint rule can be shown to be of the form $Error = \sum_{i=1}^{\infty} C_i h^{r_i}$ where $r_i = i - 1/2$, instead of $r_i = 2i$ if the integrand was smooth.

This problem was computed in axially symmetric (r, z) coordinates. The grids consisted of a region of uniform cells of size $\Delta r = \Delta z = h$ in the region $r \leq 12$, and $Z_c \leq z \leq Z_c + 12$, where Z_c is the z location of the bubble center. Symmetry conditions were imposed along the axis $r = 0$ and along the horizontal line through the center of the bubble $Z = Z_c$. The grid was stretched radially to $r = R_L$, and upward to $Z_c + R_L$, using the same number of points and spacing in each direction. The time steps were selected using an adaptive approach based on changes in the bubble volume. The number of steps taken until the first period T (time of the bubble minimum volume) is denoted by N_T . The value $\epsilon_p = 0.04$ was used as the cutoff parameter (see (2-3)) for all the computations.

A summary of the results of the symmetric bubble simulations are displayed in Table 3-1.

TABLE 3-1. SYMMETRIC BUBBLE APPROXIMATIONS

h	R_L	N_T	A_{\max}^h	A_{\max}^h Error (%)	T^h	T^h Error (%)
0.8	50	273	9.312	6.88	0.9912	7.23
0.4	100	551	9.608	3.92	1.0274	3.84
0.2	200	1100	9.798	2.02	1.0479	1.92
0.1	400	2262	9.902	0.98	1.0591	0.87

In the sequence of calculations shown, the grid was refined in conjunction with increasing the location of the boundary R_L , as well as increasing the number of time steps N_T . Notice that the errors in both the period and maximum radius are approximately halved with each refinement of the grid. This is indicative of first-order convergence. We point out that first-order convergence is typical of a second-order method approximating a problem with a discontinuity (the density across the bubble surface). A first-order method would typically produce a convergence rate of one-half (i.e., two levels of refinement would be required to reduce the error by half). These results can also be used to approximate the error of less trivial problems, based on the relative grid size and number of time steps taken.

EMPIRICAL RELATIONS AND APPROXIMATIONS

To predict underwater explosion behavior, values for A_{\min} , α , and γ need to be determined as inputs. Since the explosive process itself is not being modeled, these values must be determined through empirical relationships.

The usual assumption for the energy of the spherical bubble is that it is proportional to the charge weight, that is

$$E = QW \quad (3-6)$$

where, W is the charge weight (mass) and Q is the energy per unit mass released by the explosive, after the shock has passed.¹⁶ It follows from (3-6), (3-4e), (3-3), and (3-2) that

$$A_{\max} = J_{\infty} \left[\frac{1 - \alpha^{3(1-\gamma)}}{1 - \alpha^{-3\gamma}} \right]^{1/3} \frac{W^{1/3}}{P_{\infty}^{1/3}} \equiv J_{\alpha} \frac{W^{1/3}}{P_{\infty}^{1/3}} \quad (3-7a)$$

where

$$J_{\infty} = \left[\frac{3Q}{4\pi} \right]^{1/3} \quad (3-7b)$$

is constant. In addition to (or in conjunction with) (3-6), three additional empirical relations describing the bubbles produced from explosive charges are often cited:^{1-3,18-25,29-32}

$$A_{\min} = JNW^{1/3} = qW^{1/3}, \quad (3-8)$$

$$A_{J,\max} = J \left[\frac{W}{P_{\infty}} \right]^{1/3}, \quad (3-9)$$

and

$$T_K = K \frac{W^{1/3}}{P_{\infty}^{5/6}} \quad (3-10)$$

In the above, J is the charge radius "constant," N is the charge radius ratio "constant," K is the period constant, and q is the minimum radius constant. Also, P_{∞} is taken to be the hydrostatic pressure at the charge depth. In units of feet and feet of water,

$$P_{\infty} = d + P_A \quad (3-11)$$

where d is the initial charge depth, and P_A is the air pressure. For sea water

$$P_A = P_A^{sea} = 33, \text{ feet of water.} \quad (3-12)$$

Equation (3-8) simply reflects the assumption that the initial bubble volume is proportional to the charge weight. Values for q are difficult to measure photographically, because of the deformation of the bubble upon its collapse. This deformation is reduced for very deep charges, but to our knowledge, it has been directly measured for spherical Pentolite charges²³ ($q = 0.272 \pm 0.005$). However, the value $q = 0.288$ was reported by Yennie and Arons²² for trinitrotoluene (TNT) charges using an indirect approach based on extrapolating a curve fit to bubble radius-time curves.

Arons et al.²⁰⁻²² also approximated the value $q = 0.286$ for TNT charges at a depth of 500 ft, using pressure pulse values and incompressible bubble theory. Snay and Christian²⁴ improved on this procedure by using the difference of the maximum and minimum bubble pulse pressure measured a given distance from the bubble center. For example, if $\Delta P(R) = P_{\max}(R) - P_{\min}(R)$ is the difference in the maximum to minimum values of the pressure at a distance R from the charge center (occurring at the time of the first bubble minimum and maximum, respectively) then it

follows from integrating the conservation of momentum equation together with (3-3) (cf. Reference 24*) that

$$\frac{\Delta P(R)}{P_{\infty}} \frac{R}{A_{\max}} = \left[(\gamma - 1) \left(\alpha^{-1} - \alpha^{-3\gamma} \right) \left[\frac{\alpha^3 - 1}{1 - \alpha^{3(1-\gamma)}} \right] - \alpha^{-1} + 1 \right] \equiv \Psi_3(\alpha, \gamma) \quad (3-13a)$$

and

$$\frac{P_{\max}(R) - P_{\infty}}{P_{\infty}} \frac{R}{A_{\max}} = (\gamma - 1) \left[\frac{\alpha^3 - 1}{1 - \alpha^{3(1-\gamma)}} \right] - 1 \equiv \Psi_2. \quad (3-13b)$$

Therefore, given measured values for $\Delta P(R)$ or $P_{\max}(R) - P_{\infty}$, and A_{\max} , as well as a value for γ , one can obtain α by solving (3-13a) or (3-13b) for α and determine q using (3-2) and (3-8). Computations of q using the data from Arons et al.²⁰⁻²² are listed below in Table 3-2 for TNT charges using both $\gamma = 1.25$ and $\gamma = 1.3$. For all cases the pressure was measured at a location $R = W^{1/3}/0.352$, and the maximum radii were determined using the approximate formula (3-9) with $J = 12.6$.

TABLE 3-2. DETERMINATION OF q USING PRESSURE MEASUREMENTS FOR TNT

W (lbs)	d (ft)	$\frac{\Delta P(R)}{P_{\infty}}$	$\frac{P_{\max}(R) - P_{\infty}}{P_{\infty}}$	q ($\gamma=1.25$)	q ($\gamma=1.30$)
0.505	250	9.52	8.88	0.303	0.321
2.507	250	8.72	8.09	0.319	0.338
0.505	500	5.60	5.10	0.297	0.314
2.507	500	5.39	4.89	0.305	0.322
12.01	500	5.31	4.80	0.308	0.325
Average Values				0.306	0.324

These values were obtained by inverting Ψ_3 using Newton's method and are correct to the number of digits displayed. (We actually iterated until the relative difference in the iterative approximations were less than 10^{-14}) We remark that the same values for q were obtained using (3-13b) and the data for $P_{\max}(R) - P_{\infty}$.

Note that the values listed are higher than the value $q = 0.286$ derived by Arons²¹ (using $\gamma = 1.25$) and reported in subsequent publications.^{24,25} This discrepancy is due to several approximations performed to simplify formula (3-13b) in Reference 21. We remark that in addition to the assumption that the bubble gases behave adiabatically throughout the bubble oscillation, the additional assumption that the bubble remains spherical was also used to derive (3-13). It is this latter assumption which is most suspect as the phenomena of non-spherical bubble collapse is well documented.^{4,8-11} The non-spherical collapse is caused by gravity effects and is less pronounced for

* The formulas (3-13a) and (3-13b) are equivalent to Equations 18 and 19 of Reference 24. This can be seen using Equations 11 and 14 from that same reference.

smaller charges and/or at deeper depths. Furthermore it could be expected that a non-spherical collapse would cause liquid collisions to occur (an upward moving water jet would collide with the upper bubble surface), which would reduce the energy,¹⁴ causing a lower pressure at the minimum volume than would occur with a spherical collapse. This phenomena appears to be indicated in the data listed in Table 3-2 where at each depth the smaller charges yielded larger values for the pressure differences.

The adiabatic exponent γ can be estimated from the properties of the explosion by products.²⁵ For example, if the percentages by weight of the by-products are known, then the adiabatic exponent for the mixture is simply the ratio of the weighted sums of specific heats. From the experimental data of Jones and Miller²⁶ as well as Ornellas²⁷ the by-products of TNT yield $\gamma = 1.29 \rightarrow 1.30$. This is slightly higher than the theoretical result of Jones and Miller who estimated $\gamma = 1.27$.²⁶ The chemical products for a variety of explosive types have been computed by Renner and Short²⁸ using an empirical model for the equation of state for predicting the detonation products. Table 3-3 contains a list of charge types and their adiabatic exponents determined from the data listed in Reference 28.

TABLE 3-3. VALUES OF γ FOR VARIOUS EXPLOSIVE TYPES

Explosive	Density (g/cm ³)	γ
TNT (cast)	1.60	1.29
Pentolite	1.67	1.31
COMP C-4	1.6	1.34
PBXN-103	1.87	1.23
HBX-1	1.72	1.23

In equation (3-9) we have distinguished the approximation for the maximum radius using a charge radius constant J from the "exact" formula (3-7), where $J = J_\alpha$ is not a constant. These formulas would agree if the ratio α was a constant independent of the depth. However, it follows from (3-2), (3-7), (3-8) and (3-11) that α depends on the depth and can be determined using

$$G(\alpha) \equiv \frac{1}{\alpha} \left[\frac{1 - \alpha^{3(1-\gamma)}}{1 - \alpha^{-3\gamma}} \right]^{1/3} = N_\infty (d + P_A)^{1/3}, \quad (3-14a)$$

where N_∞ can be defined using

$$N_\infty = \frac{q}{J_\infty}. \quad (3-14b)$$

In practice, if q is known, and the maximum radius is measured at some depth, then α can be determined at that depth using (3-8) and (3-2). Given a value for γ , a value for J_∞ can then be evaluated using (3-7), and N_∞ can then be determined using (3-14b). Figure 3-1 is a graph of $\alpha = G^{-1}(N_\infty(d+33)^{1/3})$ as a function of the depth d , under the assumption that $\gamma = 1.3$ for values of $N_\infty = 0.03, 0.025, 0.02$ and 0.015 . These represent typical values for N_∞ . For example, using the

data presented in Reference 19 for TNT, the average value of $N_\infty = 0.0236$ is obtained if $q = 0.324$, $N_\infty = 0.021$ if $q = 0.286$. Also based on data from several sources for Pentolite charges the value $N_\infty = 0.0194$ is obtained. From this figure it can be seen that for a typical value of $N_\infty = 0.02$, α ranges from 15.1 to 4.5 as the depth varies from 0 to 1000 ft. It can easily be shown that $\alpha \rightarrow 1$ as $d \rightarrow \infty$, and $\alpha \rightarrow \infty$ as $d \rightarrow -P_A$. Perhaps more important is the variation of $J_\alpha = J_\alpha(d)$ as a function of d . Figure 3-2 shows the ratio J_∞/J_α as a function of depth for the same values of N_∞ . At shallow depths $d \approx 0$, J_∞ is approximately 3.1 percent larger than J_α for charges with $N_\infty = 0.02$. At a depth of 300 ft this ratio increases to 6.8 percent and at 1000 ft the ratio is 11.0 percent. This means, for example, that a value for J determined using (3-9) for a charge at a depth of 300 ft, would underpredict the maximum radius of a shallow charge by approximately 4 percent. A measurement for J based on a charge at 1000 ft would underpredict a shallow charge maximum radius by approximately 8 percent.

Figure 3-3 displays computed values for both J using (3-9) and J_∞ using (3-7) for charges of TNT at various depths. The data used for this figure came from Reference 19, Table XV, which contains data for 0.66-lb charges at depths between 300 and 600 ft,* and from Table XVIII, which contains data for 56 and 295-lb charges at depths between 36 and 95 ft. Notice that the spread in the values of J due primarily to the shallow data. The average values were $J = 12.6$ for the deeper charges and $J = 13.1$ for the shallow shots. However, the values for J_∞ are more consistent, having an average of $J_\infty = 13.59$ for the deeper shots and $J_\infty = 13.68$ for the shallow depths assuming $q = 0.286$. The corresponding deep and shallow values when $q = 0.324$ are 13.73, and 13.75, respectively. The dependence of J on the depth has been known and reported by Snay,²⁹ but it has been ignored since for the cases of previous interest J varied by about 4 percent which is within the experimental accuracy.

It is also interesting to note the the value quoted in the references was $J = 12.6$ in reports prior to 1978,^{2,20-22,24-25,29-31} while $J = 13.1$ was listed afterwards.^{3,32} This time dependence on the value J was caused by simply using values from Reference 19 Table XVIII, instead of Table XV.³³ However, since values for J for other charges are often given relative to values of TNT, the radius constants for all types of charges increased by $1.04 = 13.1/12.6$ when the report by Swisdak³² appeared. These problems would have been avoided if (3-7) was used instead of (3-9).

Increases in the measured value of J were also reported for pressed Teteryl charges.¹⁹ At depths greater than 200 ft the average value of $J = 12.8$ was reported for both 0.0558-lb charges (Table XVI) and 1/2 lb charges (Table XV). However, at depths between 1.75 and 5 ft, the average value $J = 14.1$ was reported in Table XVII.

We also distinguish the period T_K , computed using (3-10) from the theoretical period T_∞ . The bubble period can be measured reliably from experiments through the use of pressure gauges. Measurements for the period have been plotted as a function of the hydrostatic pressure P_∞ for

* The data for shot G21F was excluded since Swift and Decius¹⁹ excluded it for computing the average value of the period constant K (see page 4 of that reference).

several charge types and have been shown to lie very near the empirical relation (3-10) for depths ranging from 100 to 800 ft.¹ However, from (3-4a) and assumption (3-5), the formulas (3-4a) and (3-10) are not equivalent since the integral I_1 depends on the depth. It is interesting to compare values of T_∞ to T_K . We can do this by comparing measured values of K to computed values of

$$K_\alpha(d) = T_\infty \frac{P_\infty^{5/6}}{W^{1/3}},$$

in Figure 3-4. Both sets of values, ($\gamma = 1.3$, $q = 0.324$, $J_\infty = 13.73$) and ($\gamma = 1.3$, $q = 0.286$, $J_\infty = 13.60$) for TNT were used to compute T_∞ using (3-4). Note that for a fixed charge weight W , and a specified depth d , values for γ , q , and J_∞ will completely determine the solution to (3-1). Therefore, comparing $K_\alpha(d)$ to measured values of K provides a consistency check for the theory. In both cases the theoretical values $K_\alpha(d)$ are slightly larger than the average measured value $K = 4.36$ and have only a small dependence on the depth, thereby justifying the approximation (3-10). The choice $q = 0.286$ gives a better agreement than $q = 0.324$. The theoretical values for $K_\alpha(d)$ when $q = 0.286$ are less than 2 percent larger than the measured values at depths under 800 ft. This is in reasonably good agreement, especially when uncertainties in determinations of γ , q , and J_∞ are considered.

Since $K_\alpha(d)$ is completely dependent on values of γ , q , and J_∞ , that is

$$K_\alpha(d) = \Pi(\gamma, q, J_\infty, d),$$

it may be possible to approximate one of these constants by solving $\Pi = K$ for the parameter in question. Of course, Π is a non-linear function and a unique solution cannot in general be guaranteed. For example, suppose that $\gamma = \gamma_0$ is known and the maximum radius A_{\max} has been measured for a charge of weight $W = W_0$ at a depth of $d = d_0$. Furthermore assume that the period, and hence K was measured, but that values for the minimum radius and the pressure differences are not available, so that q remains unknown. Since by (3-7) the value for J_∞ depends on γ and α , which, in turn, depends on q , values for both q and J_∞ can be approximated if the equation

$$\Pi(\gamma_0, q, J_\infty(\gamma_0, q), d_0) = K$$

has a unique solution $q = q_0$. Figure 3-5 shows the dependence of Π as a function of q for the values $\gamma_0 = 1.2, 1.25, 1.3$, and 1.35 . Values for A_{\max} and W_0 were taken to be the average values for TNT reported in Reference 19 at a depth of approximately $d_0 = 300$ ft. At this depth the measured values for K were between 4.32 and 4.41 (shown as dashed lines in Figure 3-5), with an average of approximately 4.36. The corresponding values of q lie between 0.233 and 0.305, with the average corresponding to 0.265. These values are substantially lower than the value $q = 0.324$ determined using (3-13) based on the data in Table 3-2. As mentioned earlier, this discrepancy may be due to the assumption of a spherical bubble collapse, which was used to derive (3-13). However, the choice $q = 0.286$ yields results within the experimentally measured data. The corresponding values for J_∞ are shown in Figure 3-6.

Values for J can be determined fairly accurately through the use of high speed photography.¹⁸ Unfortunately, for many of the newer charge types, values for J have not been determined directly from photographs due to the extra cost, but instead were inferred using a value of K from period measurements. It has been reported³⁰ that values of J/K are relatively constant, ranging from $J/K = 2.84$ for Pentolite, to $J/K = 2.96$ for pressed Tetryl.¹⁹ Therefore, given K , one can use $J = 2.90K$ as an approximation, if photographic measurements are not available. However, this can be another source of error since according to (3-7), neither J nor K are independent of depth. (Although Figure 3-4 indicates that K is less sensitive than J , particularly for shallow depths). However, in the absence of more reliable data the approximation $J_{\infty} = 3.1K$ can be used based on the values displayed in Figures 3-2, 3-5 and 3-6 for TNT discussed above. A more accurate procedure for determining J_{∞} would be to solve the equation

$$\Pi(\gamma, q, J_{\infty}, d) = K, \quad (3-15)$$

assuming that γ and q are known, and K has been measured at some depth d .

The values often given in the literature for the radius constant J were determined for sea water, while the tests discussed in this paper are for fresh water. In fresh water it can be expected that the maximum bubble radius will be larger due to the fact that fresh water is less dense than sea water. The correction for fresh water is³⁰

$$J_{F,\infty} = \left(\frac{33.9}{33}\right)^{1/3} J_{S,\infty} \quad (3-16)$$

where the ratio 33.9/33 is the ratio of air pressure in units of feet of fresh water to sea water. It is also the approximate density ratio of sea to fresh water. In the case of fresh water, the value $P_A = P_{F,A} = 33.9$ should be used with $J_{F,\infty}$ in (3-7). (Actually, the value 34 was used instead of 33.9 in Reference 30.)

Two-Dimensional Bubbles

Suppose several identical charges are placed in a line and are separated by a distance that is considerably less than their free field maximum radius. Then it could be expected that this "line of charges" could be approximated (at least at the central charge) as a two-dimensional problem in which the bubble is cylindrical and has infinite length. In such cases, the three-dimensional problem with multiple charges could be approximated by a much simpler (and computationally less intensive) two-dimensional problem.

Let each individual charge have mass W , and be separated by a distance S . From (3-8) each of these charges would produce a spherical bubble having a minimum (initial) radius given by

$$A_{\min}^{(3D)} = qW^{1/3}.$$

Let $A_{\min}^{(2D)}$ denote the minimum radius of the cylindrical bubble used in the two-dimensional approximation. Imposing the condition that the bubble volume per unit length is the same for both the multiple spheres and the single cylinder yields

$$\frac{4}{3}\pi(A_{\min}^{(3D)})^3 = \pi(A_{\min}^{(2D)})^2 S.$$

Combining this with (3-8) yields

$$A_{\min}^{(2D)} = \frac{2}{\sqrt{3S}}(A_{\min}^{(3D)})^{3/2} = \frac{2}{\sqrt{3}}q^{3/2}M^{1/2} = q^{(2D)}M^{1/2}, \quad (3-17a)$$

where

$$q^{(2D)} = \frac{2}{\sqrt{3}}q^{3/2}, \quad (3-17b)$$

and $M = W/S$ is the mass per unit length of the line charge. The initial pressure for the cylindrical bubble is the same as for each individual charge given in (3-3) with $\alpha = \alpha^{(3D)}$ being the ratio of the individual spherical bubble's maximum to minimum radii. In practice, the value for $\alpha^{(3D)}$ could be determined by solving (3-14a). An estimate for the maximum radius of the cylindrical bubble can be obtained by equating the equivalent expression for the initial pressure

$$P_B^0 = P_{\infty}(1-\gamma) \left[\frac{1-(\alpha^{(2D)})^2}{(1-(\alpha^{(2D)})^{2(1-\gamma)})} \right]$$

where $\alpha^{(2D)} = A_{\max}^{(2D)}/A_{\min}^{(2D)}$, to (3-3) which yields

$$\alpha^{(2D)} = (\alpha^{(3D)})^{3/2}.$$

Using this with (3-17) and (3-7) we obtain

$$A_{\max}^{(2D)} = J_{\infty}^{(2D)} \left[\frac{1-(\alpha^{(2D)})^{2(1-\gamma)}}{1-(\alpha^{(2D)})^{-2\gamma}} \right]^{1/2} \frac{M^{1/2}}{P_{\infty}^{1/2}} \quad (3-18a)$$

where

$$J_{\infty}^{(2D)} = \frac{2}{\sqrt{3}}J_{\infty}^{3/2}. \quad (3-18b)$$

Therefore, the empirical constants and initial conditions for a cylindrical bubble, can be determined directly from the spherically symmetric bubble theory.

FREE SURFACE EFFECTS

Here the effects of the free surface on the period and maximum bubble volume are examined. Both theoretical and computational results are presented. This analysis is crucial for a better understanding of the comparisons of our computational results to the experimental data presented in the next chapter.

Free Surface Effects on Bubble Period

The effects of both the surface and a rigid bottom boundary on the bubble period has been studied by Friedman.¹⁶ Under the assumption that the bubble remains spherical, as well as the usual

assumptions that the bubble gases behave adiabatically (2-2) and are surrounded by a constant density incompressible liquid, he used potential theory together with the "method of images" to derive a formula for surface and boundary corrections. This formula can be expressed as

$$T_{d,b} = T_{\infty} \left[1 - \frac{\kappa T_{\infty} \sqrt{P_{\infty}} F(x)}{d} \right], \quad (3-19)$$

where b is the initial distance from the bubble center to the bottom surface, $T_{d,b}$ is the corrected period, T_{∞} is the "free field" period, $F(x)$ is defined by the infinite series

$$F(x) = \frac{x}{1+x} + (1-x) \left[\sum_{n=1}^{\infty} \frac{(-1)^n x}{(2n+1)^2 - x^2} + \frac{\log 2}{2} \right] \quad (3-20a)$$

where

$$x = \frac{b-d}{b+d}, \quad (3-20b)$$

and κ is a constant depending on the adiabatic exponent γ and the minimum to maximum ratio α (3-2). In particular, if values of A_{\min} and A_{\max} are known *a priori* then κ can be computed using

$$\kappa = 1.158 \frac{I_2}{I_1^2} \quad (3-21)$$

where I_1 is defined in (3-4b) and

$$I_2 = \int_{a_0}^{a_1} \frac{a^{5/2} da}{\sqrt{1 - a^3 - ka^{-3(\gamma-1)}}}, \quad (3-22)$$

In (3-21) the coefficient $1.158 = 0.25\sqrt{2g/3}$, where $g = 32.174$ is the acceleration due to gravity in units of ft/sec^2 . Note that if the water is infinitely deep, $b = \infty$, it follows from (3-20) that $x = 1$ and $F(x) = 1/2$. For details on the derivations of these formulae see Friedman¹⁶ and Cole.^{1*}

Figure 3-7 displays the comparison between the theoretical correction T_d/T_{∞} (using (3-19)) and the computations using the medium grid ($h=0.2$). The computational results plotted are T_d^h/T_{∞}^h , where $T_{\infty}^h = 1.0479$ (from Table 3-1) was used instead of $T_{\infty} = 1.0684$ to reduce the effects of discretization errors. Using (3-22) together with the initial conditions (3-5) yields a value of $\kappa = 1.189$, which is typical of values which have been reported ($1.13 \leq \kappa \leq 1.22$) from experimental data.^{1,16,25} We remark that formula (3-19) has been used in practice in its approximate form, with T_K replacing T_{∞} on the right hand side.²⁵ Let C to be the *scaled depth*,

$$C = \frac{d}{A_{\max}}. \quad (3-23)$$

* The formula (3-20) is taken directly from Friedman,¹⁶ page 190. Cole¹ uses a different equivalent formula but erroneously omits the alternating sign $(-1)^n$ whenever dealing with formulas resulting from the image theory (page 323, 330, and formula (8.60) on page 333). However, his Figure 8.1 on page 335 for the image function is correct. That is, it represents values not from his formula (8.60) but values which are obtained using an alternating series in (8.60).

Figure 3-7 shows the agreement between the computations and theory to be very good, particularly for values of $C \geq 1.5$. However, the disagreement increases for smaller values of C . In this case, the validity of the theory becomes questionable due to the assumption that the bubble remains spherical throughout its entire motion. An additional assumption used for the derivation of (3-19) is that the boundary condition for the potential at the free surface is linear and homogeneous. It has been more recently demonstrated³⁴ that the more correct nonlinear terms in the free surface boundary condition become extremely important for $C < 1.5$. The actual computational results are also listed below in Table 3-4 together with the computed equivalent maximum bubble radii.

TABLE 3-4. FREE SURFACE EFFECTS ON PERIOD AND MAXIMUM RADIUS

$C = \frac{d}{A_{\max}}$	T_d^h	$A_{\max}^h(C)$
0.56	0.7655	9.384
0.60	0.7759	9.460
0.80	0.8200	9.666
1.00	0.8554	9.736
2.00	0.9474	9.789
4.00	1.0020	9.796
∞	1.0479	9.797

For these computations, a uniform grid with $h=0.2$ was used in the region $0 \leq r \leq 12$, and $-(d+12) \leq z \leq 12$, with grid stretching to $r = R_L = 200$, and downward to $z = -(d+R_L)$. The value $\epsilon_A = 0.4$ was used at the air-water interface and $\epsilon_p = 0.04$ at the bubble interface (see Chapter 2).

Free Surface Effects on Maximum Radius

Very little attention has been given to the effects on the maximum bubble radius due to the proximity of the surface. Here, by bubble "radius" we mean the equivalent radius of a sphere with the same volume, since in general, the bubble may diverge from its spherical shape at the time of its maximum volume. The formulas for maximum radius found in Friedman¹⁶ are not appropriate since their derivation depended on the additional assumption that the velocity of the surface is negligible (this is the assumption which linearizes the free surface boundary condition) and the bubble stays spherical. Indeed, those formulas for maximum radius predict a reduction due only to the vertical migration of the bubble and are not appropriate here.

Let $D(t)$ be a domain occupied by an incompressible liquid, that is,

$$D(t) = \left\{ \mathbf{x} : \rho(\mathbf{x}, t) = \rho_0, \quad \nabla \cdot \mathbf{u}(\mathbf{x}, t) = 0 \right\}.$$

Consider the following class of free surface problems.

DEFINITION: (Class A Problems)

A *Class A* free surface problem is one which satisfies the following assumptions:

- (i) If $D(t)$ extends to infinity in one or more directions then the velocity and pressure have the asymptotic behavior

$$\begin{aligned} u(x,t) &= O\left[\frac{1}{|x|}\right] \\ P(x,t) &= P_\infty + O\left[\frac{1}{|x|}\right] \end{aligned}$$

as $|x| \rightarrow \infty$, where P_∞ is a constant.

- (ii) The liquid region, $D(t)$ completely surrounds a *bubble region* $B(t)$, having a boundary denoted by $\partial B(t)$. This region contains a uniform pressure given by

$$P_B = CV_B^{-\gamma} \equiv f(V_B), \quad (3-24)$$

where $C > 0$, and $\gamma > 1$ are constants and V_B is the volume of $B(t)$ given by

$$V_B(t) = \int_{B(t)} d\mathbf{x}.$$

Furthermore, the pressure is assumed to be continuous so that $P_B = f(V_B)$ on $\partial B(t)$ also.

- (iii) All other finite boundaries of D are such that either $\mathbf{u} \cdot \mathbf{n} = 0$ (rigid wall or symmetry boundaries) or $P = P_\infty$ (free surface).
 (iv) No gravity is acting.
 (v) Initially, the liquid has zero velocity, that is,

$$\mathbf{u}(\mathbf{x}, 0) = 0. \quad (3-25)$$

The simplest example of a *Class A* problem is the spherically symmetric bubble in an infinite domain. This problem, governed by equation (3-1), yields periodic solutions for the bubble radius with $A_{\min} \leq a(t) \leq A_{\max}$.

Let

$$V_{\min}^S = \frac{4}{3}\pi A_{\min}^3, \quad V_{\max}^S = \frac{4}{3}\pi A_{\max}^3, \quad (3-26)$$

denote the minimum and maximum volumes of a spherically symmetric bubble.

Without loss of generality we can assume that initial conditions for our *Class A* problems satisfy

$$V(0) = V_{\min}^S, \quad (3-27)$$

and

$$P_B(0) = P_B^0 \geq P_\infty. \quad (3-28)$$

Let $e(t)$ be the *kinetic energy* of the liquid

$$e(t) = \int_{D(t)} \frac{1}{2} \rho |\mathbf{u}|^2 d\mathbf{x}. \quad (3-29)$$

The following result states that an upper bound on the bubble volume is the maximum free field bubble volume.

THEOREM 3-1: The volume of a bubble $B(t)$ governed by a *Class A* free surface problem, with initial conditions (3-27), (3-28) satisfies the inequality

$$V_{\min}^S \leq V_B(t) \leq V_{\max}^S, \quad \text{for } t \geq 0, \quad (3-30)$$

with equality holding only if $e(t) = 0$.

PROOF: The energy balance equation is

$$\frac{de}{dt} + \int_{\partial B(t)} (P - P_{\infty})(\mathbf{u} \cdot \mathbf{n}) dS = 0, \quad (3-31)$$

where \mathbf{n} is the unit outer normal to $D(t)$, and e is defined by (3-29). This is derived by taking the dot product of the velocity vector with the momentum equations (2-1b) (with $g=0$ by *Class A* condition (iv)), integrating in space, and applying the *Class A* assumptions (i) and (iii) together with the Divergence theorem. Since $\partial B(t)$ is the surface of the bubble, its speed of propagation in the direction of \mathbf{n} is given by $-\mathbf{u} \cdot \mathbf{n}$, it follows that

$$\int_{\partial B(t)} (\mathbf{u} \cdot \mathbf{n}) = -\frac{dV_B}{dt}. \quad (3-32)$$

Using (3-32) in (3-31) it follows that

$$\frac{de}{dt} - \left[f(V_B) - P_{\infty} \right] \frac{dV_B}{dt} = 0,$$

or equivalently

$$e + F(V_B) = C, \quad (3-33)$$

where C is a constant of integration, and

$$F(V) = - \int_V^V [f(\tau) - P_{\infty}] d\tau \quad (3-34)$$

Note that for $V > 0$

$$\frac{dF}{dV} = -[f(V) - P_{\infty}], \quad (3-35)$$

and using (3-24),

$$\frac{d^2F}{dV^2} = \frac{\gamma}{V} f(V) > 0,$$

so that F is a convex function of V , with a unique minimum

$$F(V_\infty) = \min_{V \geq 0} \{F(V)\},$$

where $f(V_\infty) = P_\infty$ by (3-35). The *Class A* assumption (v) implies that $e(0) = 0$. This, combined with (3-33) and the initial condition (3-27) yields

$$e(t) = F(V_{\min}^S) - F(V_B(t)).$$

Noting that $F(V_{\max}^S) = F(V_{\min}^S)$ (from (3-3)), and $e(t) \geq 0$, the theorem follows from the convexity of F .

Theorem 3-1 states that the presence of the free surface, or a rigid boundary, will in general reduce the maximum bubble volume. The same conclusion holds if the initial shape of the bubble is non spherical. A simple explanation, which summarizes the proof of the theorem, is that if there is any kinetic energy in the incompressible liquid at the time of the maximum bubble volume is attained, then the potential energy of the bubble F , and hence volume, must be less than if the kinetic energy were zero, as it is in the spherically symmetric case.

Figure 3-8 is a graph of the reduction of the equivalent maximum radius $A_{\max}(C)/A_{\max}(\infty)$, using both the computational results from Table 3-4, as well as an empirical fit to this data, given by the formula

$$\frac{A_{\max}(C)}{A_{\max}(\infty)} = \left[1 - \frac{0.0071}{C^3} \right] = \left[1 - \frac{0.0071 A_{\max}^3(\infty)}{d^3} \right]. \quad (3-36)$$

If a measured value for the maximum radius is used in $A_{\max}(C)$, then $A_{\max}(\infty)$ can be approximated by solving (3-36). Of course, this approximation may only be valid when $\alpha \approx 10$, but this is a fairly typical value according to Figure 3-1.

NEW BUBBLE PARAMETERS

As was demonstrated earlier in this chapter, the commonly used empirical formula (3-9) is inaccurate for shallow charge depths. Therefore, the value J_∞ defined in (3-7) needs to be determined, as opposed to $J = J_\alpha$, which is depth dependent. First, consider direct observations of the maximum bubble radius for shallow charges of C-4, and both shallow and deep charges of Pentolite. Table 3-5 lists the computed values for J_∞ based on measured maximum bubble radii for C-4 and Pentolite charges. In this table, the data sources prefixed with a CD describes measurements taken from the NSWCCD Test Pond in May, 1993.

TABLE 3-5. MAXIMUM RADIUS MEASUREMENTS AND J_∞ VALUES FOR PENTOLITE AND C-4 CHARGES

Data Source	Charge Type	d (ft)	W (lb)	A_{\max}^{meas} (ft)	$A_{\max}(\infty)$ (ft)	C	J_α	J_∞
CD-9	C-4	2.5	1.25	4.57	4.78	0.52	14.7	15.0
CD-11	C-4	5.0	1.25	4.75	4.78	1.05	15.0	15.3
CD-17	C-4	9.0	1.06	4.08	4.08	2.21	14.0	14.3
CD-10	Pentolite	2.5	1.72	5.50	5.95	0.42	16.5	16.8
CD-13	Pentolite	5.0	1.73	5.75	5.81	0.86	16.4	16.8
CD-16	Pentolite	9.0	1.73	4.84	4.85	1.86	14.1	14.5
Ref. 19	Pentolite	335	0.551	1.46	1.46	229	12.7	13.7
Ref. 19	Pentolite	396	0.548	1.33	1.33	297	12.2	13.2
Ref. 23	Pentolite	5982*	1.06	0.698	0.698	8570	12.4	15.0
Ref. 23	Pentolite	11852†	1.03	0.545	0.545	21746	12.3	15.6

Obviously, there is a fairly large amount of scatter in the data listed above. In addition to modeling assumptions, the scatter can also be attributed to inaccuracies in measuring the bubble size, and variations of the explosive product itself (e.g., age, storage conditions, and manufacturing process may all have some effects on the detonation.) However, it appears that the values for J_∞ at shallower depths are somewhat larger than the values determined at greater depths with the exception of the very deep shots reported in Reference 23. This discrepancy cannot be explained by our theory. Indeed, equation (3-36) and Theorem 3-1 predict the opposite effect. Therefore, if this effect is real then it must be due to other physical effects (shock effects, dissolved gases near the free surface, etc.) not modeled in our theory. The result for the $d = 2.5$ Pentolite case (CD-10) may also not be valid here since it is likely that the bubble may have partially vented into the atmosphere before it attained its maximum size.

As mentioned previously, an alternative method for determining J_∞ is to use period measurements and solve equation (3-15). Since the free surface and bottom locations had an effect on many of the tests reported, the values J_∞ were determined using (3-15) with

$$\Pi(\gamma, q, J_\infty, d) = T_{d,b} \frac{P_\infty^{5/6}}{W^{1/3}}$$

with $T_{b,d}$ defined using (3-19). The tabulated results of this procedure are listed in Table 3-6 below. In this table, the values listed for $A_{\max}(\infty)$ were determined from the derived values of J_∞ from solving (3-15) and using (3-7a), with α determined from (3-14). Here, data sources prefixed with ARV describe tests performed in Arvonja in August, 1993, and the BP prefix corresponds to tests at the Briar Point facility in June, 1994.

* Average values for 3 shots at depth between 5934 and 6030 ft.

† Average values for 9 shots at depths between 11812 and 11885 ft.

TABLE 3-6. COMPUTED J_{∞} VALUES BASED ON PERIOD MEASUREMENTS

Data Source	Charge Type	W (lbs.)	d (ft.)	$b+d$ (ft.)	T^{meas} (sec.)	$A_{max(\infty)}$ (ft.)	C	J_{∞}
CD-11	C-4	1.25	5.0	24	0.1952	4.48	1.12	14.4
CD-3	C-4	1.25	9.0	24	0.1952	4.21	2.14	14.0
CD-17	C-4	1.06	9.0	24	0.1861	3.99	2.25	14.0
ARV-1	C-4	10.0	6.0	110	0.34	9.63	0.62	15.6
CD-13	Pentolite	1.75	5.0	24	0.2120	4.95	1.01	14.3
CD-4	Pentolite	1.75	9.0	24	0.2150	4.67	1.93	14.0
CD-16	Pentolite	1.72	9.0	24	0.2157	4.68	1.92	14.1
Ref. 35	Pentolite	0.671	39	87	0.108	2.78	14.0	13.8
Ref. 35	Pentolite	0.655	39	106	0.108	2.79	14.0	14.0
Ref. 19	Pentolite	0.552	335	3600	0.02607	1.46	229	13.6
Ref. 19	Pentolite	0.566	404	4800	0.02290	1.37	295	13.6
Ref. 19	Pentolite	0.550	396	4700	0.02240	1.32	300	13.2
Ref. 19	Pentolite	0.551	380	6700	0.02347	1.36	279	13.4
BP-7	HBX-1	206	25	54	0.883	23.18	1.08	16.4
BP-4	HBX-1	206	26	54	0.894	23.34	1.11	16.6
BP-6	HBX-1	206	27	54	0.891	23.21	1.16	16.6
BP-2	HBX-1	206	28	54	0.891	23.01	1.22	16.6
BP-5	HBX-1	206	29	54	0.889	22.80	1.27	16.5
BP-3	HBX-1	206	30	54	0.888	22.67	1.32	16.5
BP-8	PBXN-103	26.2	10.1	54	0.542	15.08	0.67	19.1
BP-9	PBXN-103	26.2	13.8	54	0.544	13.69	1.01	17.9
Ref. 35	PBXN-103	29.3	30	65	0.550	13.88	2.16	19.3

As in Table 3-5, the estimations for J_{∞} appear to be larger for smaller values of C (with the exception of the PBXN-103 charge at $d = 30$). In this case, however, this can be attributed to the underestimation of the period using (3-19) (see Figure 3-7). Also, the values obtained for J_{∞} using the period are substantially below the corresponding values listed in Table 3-5 for both C-4 and Pentolite charges with $d = 5$ and $d = 9$. The values obtained for Pentolite charges at depths of $d = 335$ and $d = 396$ using both procedures yield essentially the same result. Unfortunately, other comparisons can not be made at this time since the periods for the Pentolite charges listed in Reference 23 were not listed, and the bubbles were not photographed for the HBX-1 or PBXN-103 shots listed in Table 3-6.

The explosive bubble parameters used in the next chapter are listed below. The $2D$ values listed were derived using (3-17) and (3-18).

TABLE 3-7. EMPIRICAL BUBBLE PARAMETERS

Charge	γ	q	J_{∞}	$q^{(2D)}$	$J_{\infty}^{(2D)}$
C-4	1.34	0.286	15.3	0.177	69.1
Pentolite	1.30	0.272	15.3	0.164	69.1
HBX-1	1.23	0.360	16.5	0.249	77.4
PBXN-103	1.23	0.400	18.8	0.292	94.1

These values for C-4 and Pentolite are only roughly based on the data listed in Tables 3-5 and 3-6. For C-4 the value $J_{\infty} = 15.3$ is simply the value in the case when $C \approx 1.0$ (shot CD-11) based on photographic measurement. It also corresponds to the shallowest case for which the bubble remained nearly spherical at the time of its maximum size. Due to the wide scatter in the values listed in Table 3-5 for Pentolite we simply chose the same value as C-4. The equivalence of C-4 and Pentolite is supported by tests performed by Heathcote and Niffenegger.³⁶ These values should be considered valid for shallow depths only, and $J_{\infty} \approx 13.8$ is probably a better approximation for $C > 2$. Note that this value is much closer to the value $J_{\infty} = 13.6$ for TNT charges derived earlier. For HBX-1 and PBXN-103 the averages of the values for J_{∞} listed in Table 3-6 was used.

SPARK BUBBLE COMPARISONS

We continue our code validations by attempting to match the excellent photographs of a shallow depth spark generated bubbles.⁴ These experiments were done in free-fall, thereby removing the effects of gravity. Furthermore, it can be expected that the shock wave from the spark will be weaker than that resulting from an explosive so the early time compressible effects (e.g., cavitation and spalling at the surface) are not evidenced in these experiments.

In particular, consider the case $C = 0.56$. In the experiments the value $A_{\max} = D_{\max}/2$ was used as a value for the maximum radius for the determination of the scaled depth (3-23), where D_{\max} was the maximum observed horizontal diameter of the bubble. According to the computations we conducted, the maximum width matched the maximum equivalent radius to less than 0.5 percent for examples with $0.5 \leq C \leq 0.6$ despite the fact that the bubble does not remain spherical. (By maximum equivalent radius we mean the radius of a sphere with the same volume as the maximum bubble volume.)

In order to slightly improve our simulation of the experiment we used the free surface correction based on (3-36). In particular, for the initial conditions we modified (3-5), using $A^0 = 1.042$ instead of $A^0 = 1.0$, so that $A_{\max}(C) \approx D_{\max}/2 \approx 10$, when the initial depth is $d = 5.6$. The grids used for the computations consisted of a region of uniform cells of size h in the region $0 \leq r \leq 12$ and $-16 \leq z \leq 24$. Outside of this uniform grid region the grids were stretched downward to $z = Z_b = -119$, upward to $z = Z_t = 100$, and radially to $r = R_L = 72.6$, which corresponds to a scaled version of the experimental apparatus.

Figure 3-9 compares a copy of the photographs of the experiments of Blake and Gibson to the computations using the "fine" grid ($h = 0.1$, 160×488 cells, $N_T \approx 2000$ steps). The times printed

above the figures are scaled using

$$T = \frac{t}{A_{\max}} \sqrt{\frac{P_{\infty}}{\rho_0}}, \quad (3-37)$$

where t is the actual time. The frames corresponding to the computational results contain density contours of $\rho = 0.5\rho_0$ at the same scaled times as the photographs. Note the agreement in predicting the large central jet rising above the surface, as well as the smaller downward moving jet, which can be seen in the frames corresponding to $T = 0.59$. This downward moving jet passes through the center of the bubble and by $T = 1.16$ has impacted its bottom surface. This jet impacts the bottom slightly earlier in the computations, but this may be due to the fact that the gases in the spark bubble are very likely at or near the vapor pressure P_v , as opposed to having an adiabatic behavior. In this event the times should be scaled using $P_{\infty} - P_v$ in place of P_{∞} in (3-37).

Figure 3-10 shows the results of computations using both the "medium" ($h = 0.2$, 80×264 cells, $N_T \approx 1000$ steps) and "coarse" ($h = 0.4$, 41×141 cells, $N_T \approx 500$ steps) grids. This shows that qualitative agreement can be attained without large computational expense. Quantitatively, the scaled heights of the plume from both the experiments and the computations are shown in Figure 3-11. The computed plume heights are all above the measured values, which again may be due to the vapor pressure. Nevertheless, the agreement is still very good. The run times for these computations were approximately 15 min for the coarse grid run, 3 hr for the medium grid run, and 24 hr for the fine grid run on an HP 9000-735 workstation.

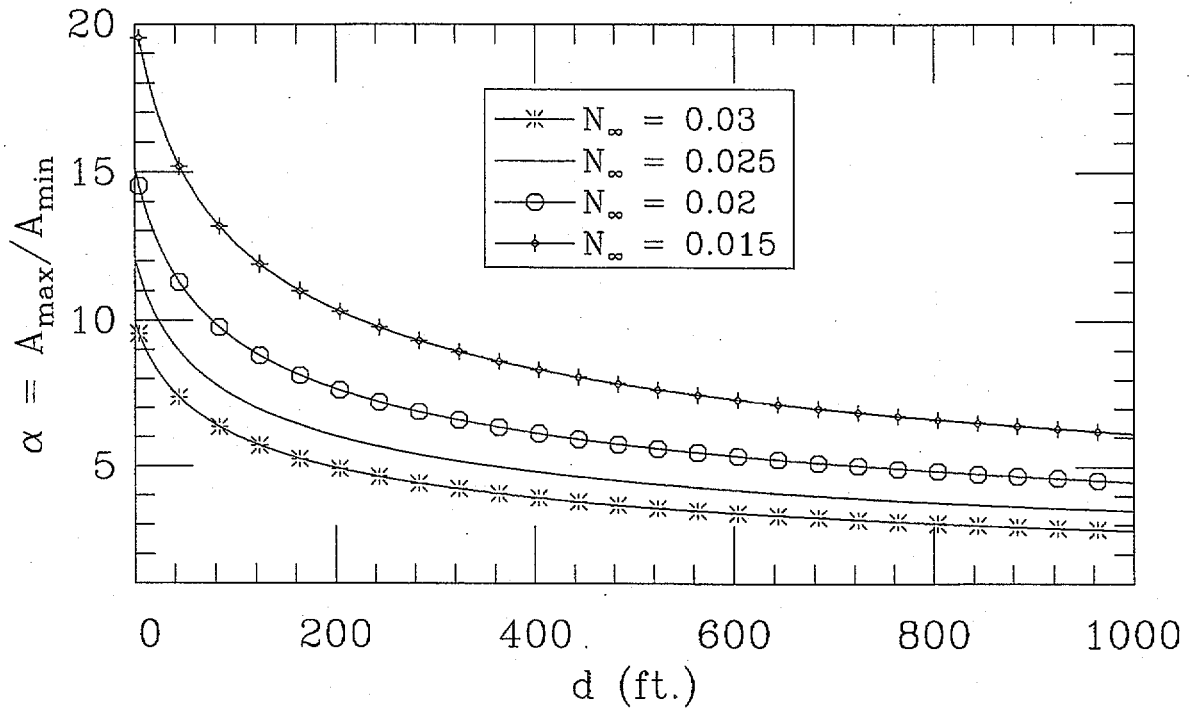


FIGURE 3-1. DEPENDENCE OF THE RADIUS RATIO ON THE DEPTH
WITH $\gamma = 1.3$ AND VARIOUS VALUES OF N_{∞}

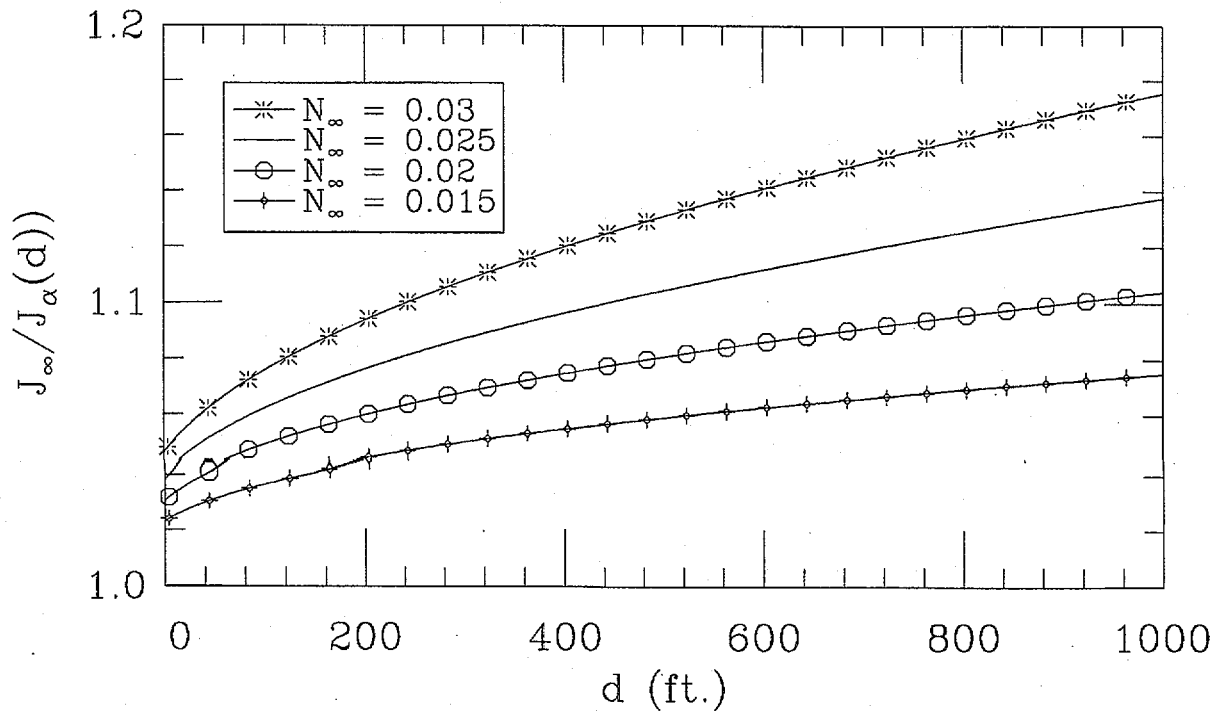


FIGURE 3-2. RATIO BETWEEN THE RADIUS CONSTANT J_{∞} AND $J_{\alpha}(d)$
WITH $\gamma = 1.3$ FOR VARIOUS VALUES OF N_{∞}

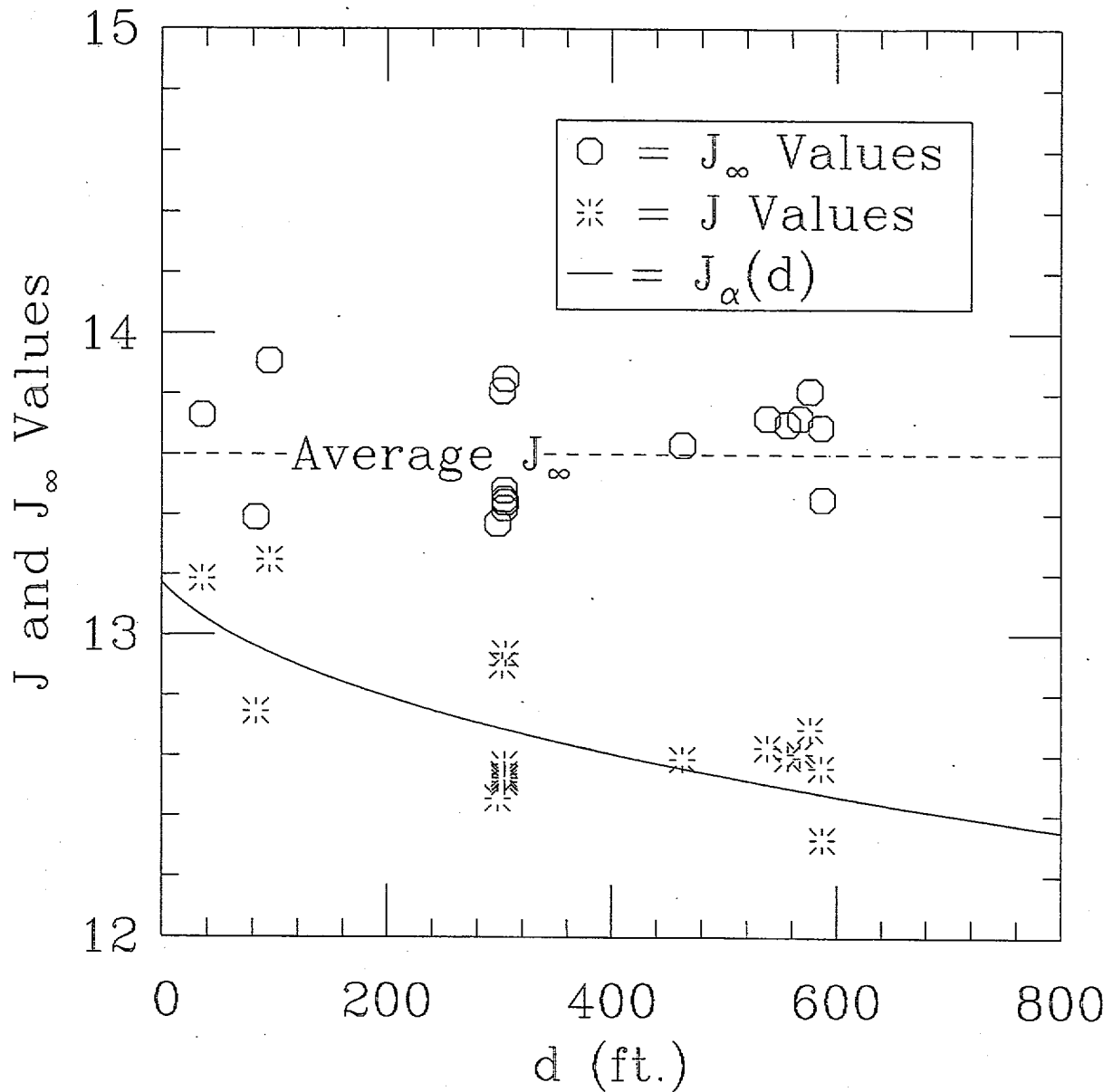


FIGURE 3-3. MEASURED VALUES OF J AND J_{∞} FOR TNT CHARGES AT DIFFERENT DEPTHS

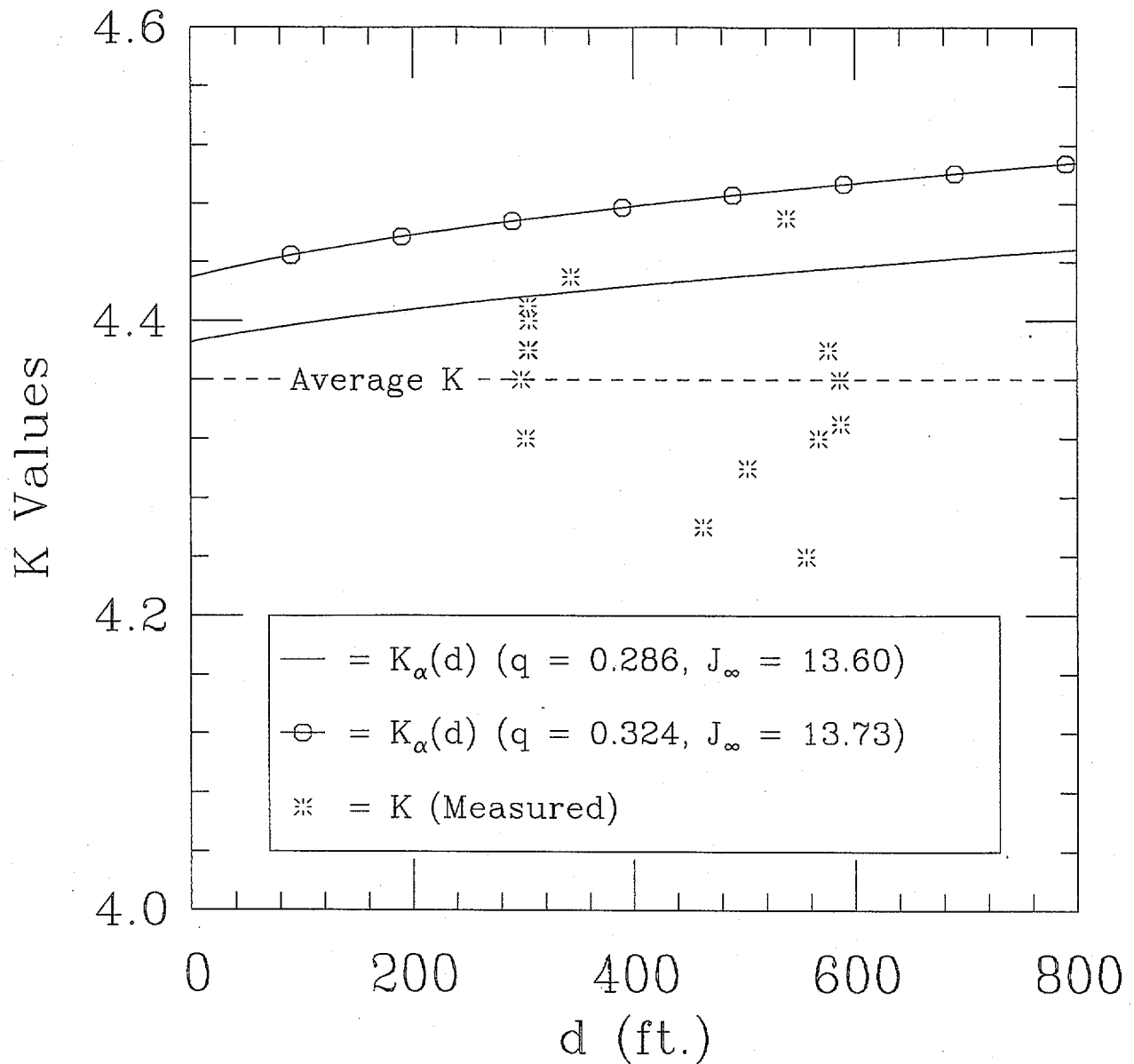


FIGURE 3-4. MEASURED AND THEORETICAL VALUES OF K FOR TNT CHARGES AT DIFFERENT DEPTHS.

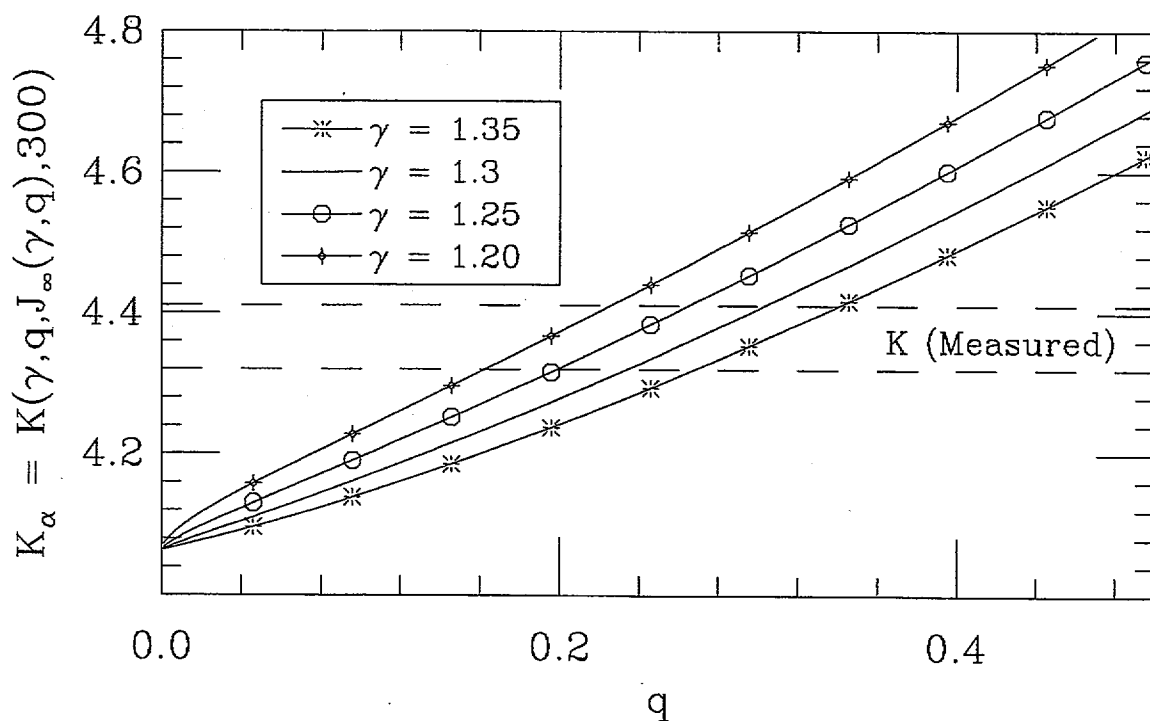


FIGURE 3-5. THEORETICALLY DETERMINED VALUES OF K_α AS A FUNCTION OF q FOR VARIOUS VALUES OF γ

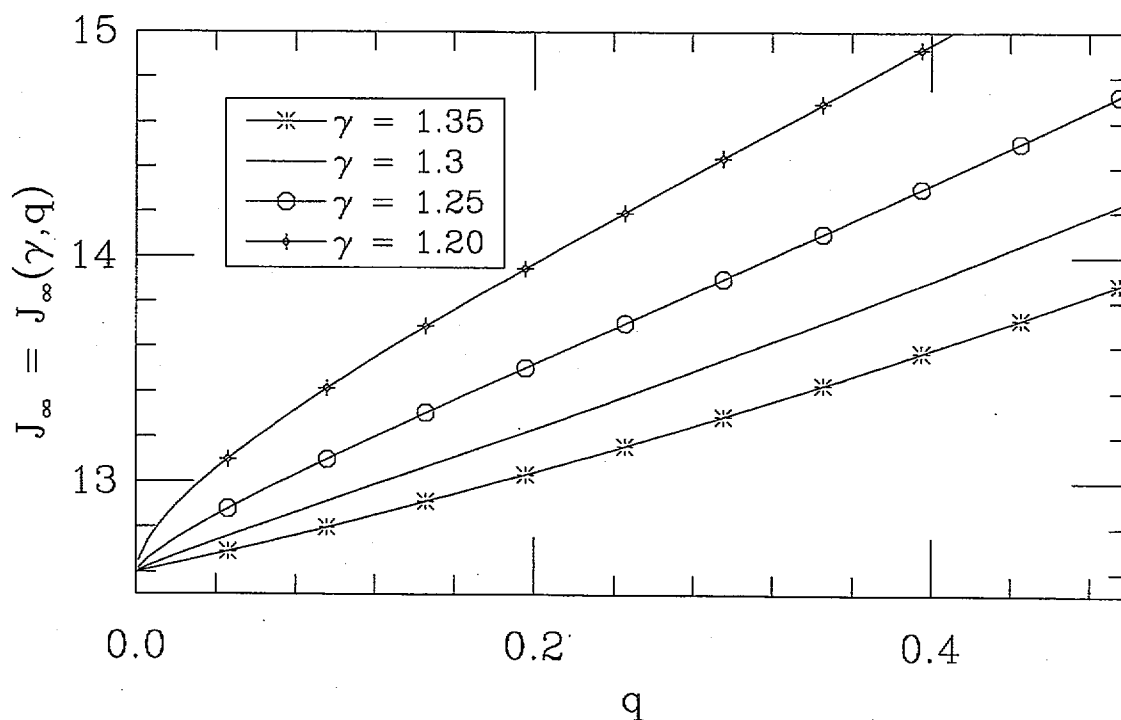


FIGURE 3-6. DEPENDENCE OF J_∞ ON q FOR VARIOUS VALUES OF γ (BASED ON A VALUE A_{\max} MEASURED AT $d = 300$ FT)

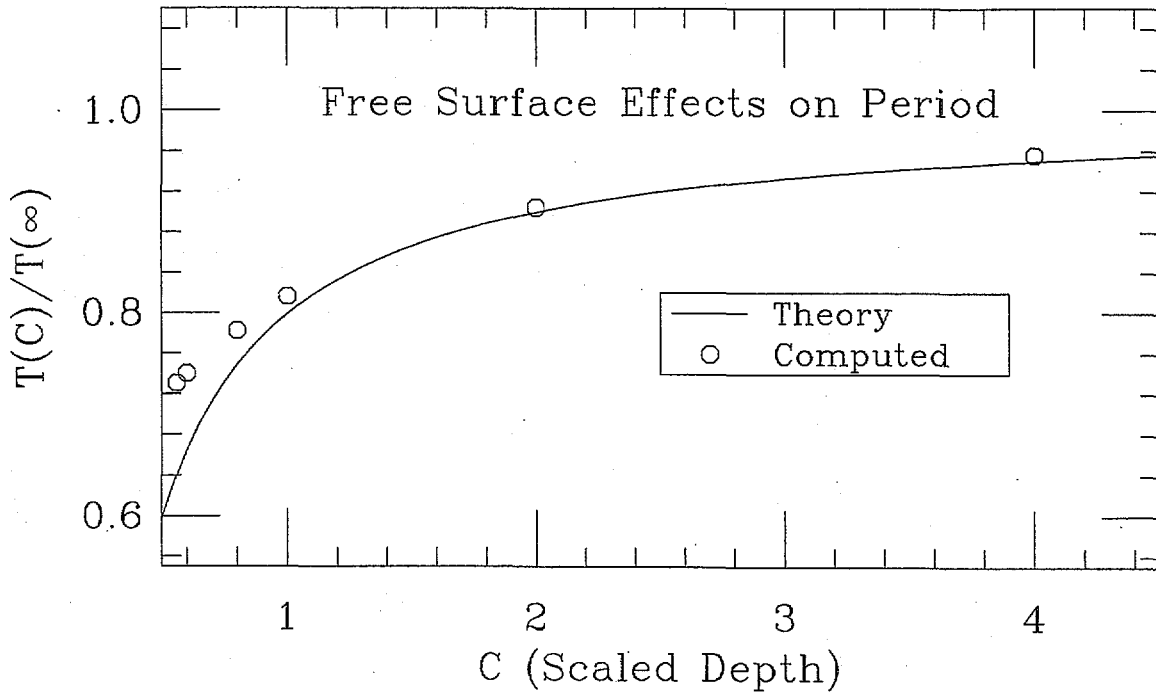


FIGURE 3-7. COMPARISON OF THEORY TO COMPUTATIONS OF FREE SURFACE EFFECTS ON THE PERIOD IN THE ABSENCE OF GRAVITY

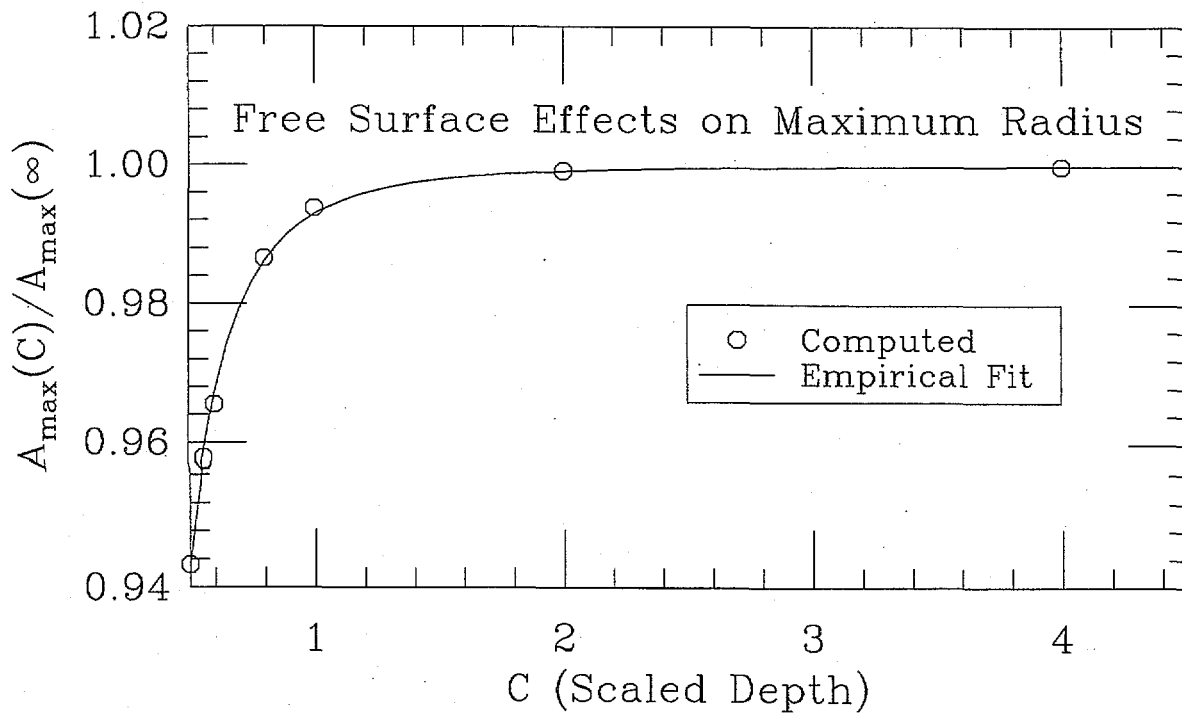
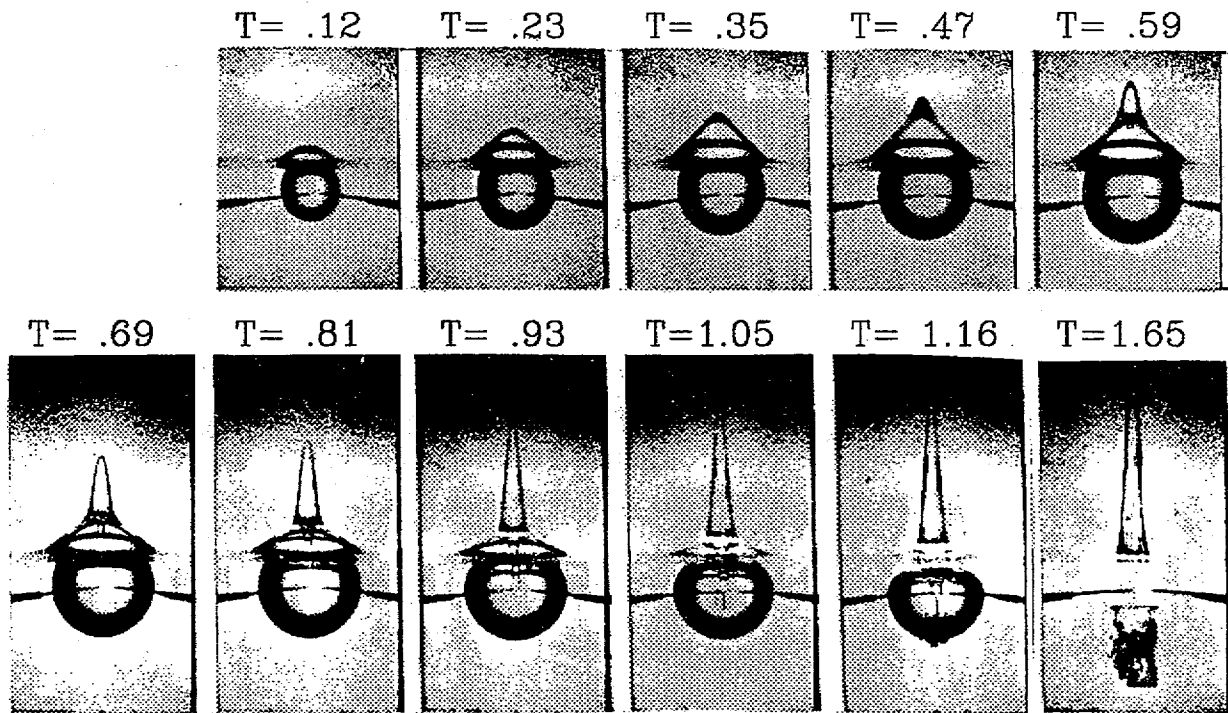
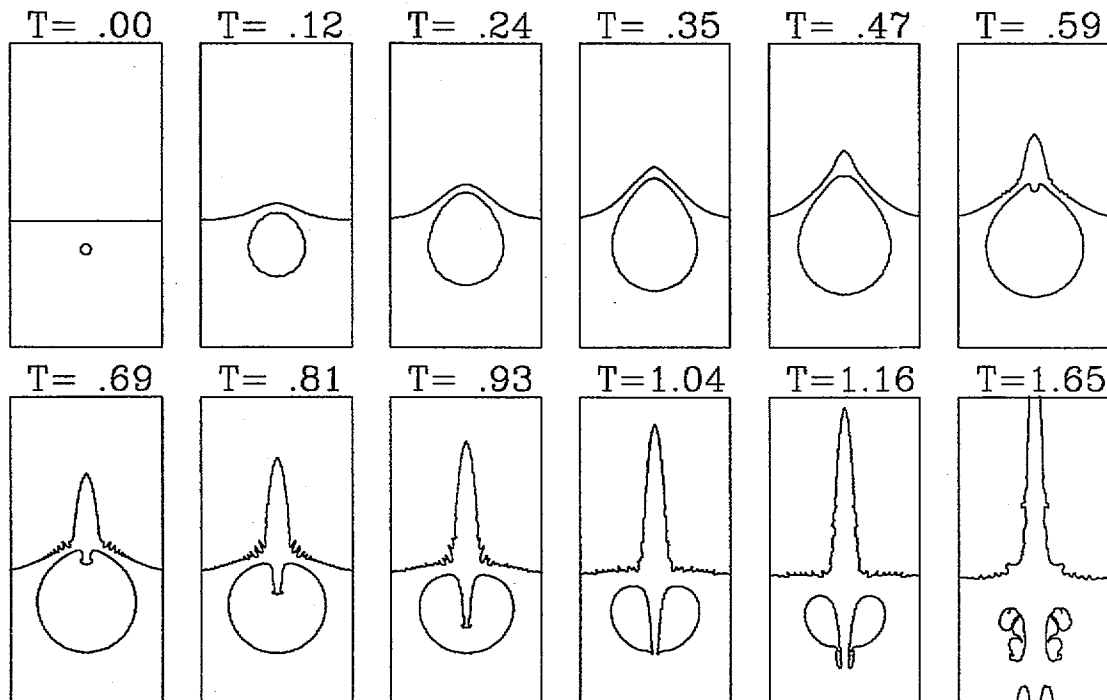
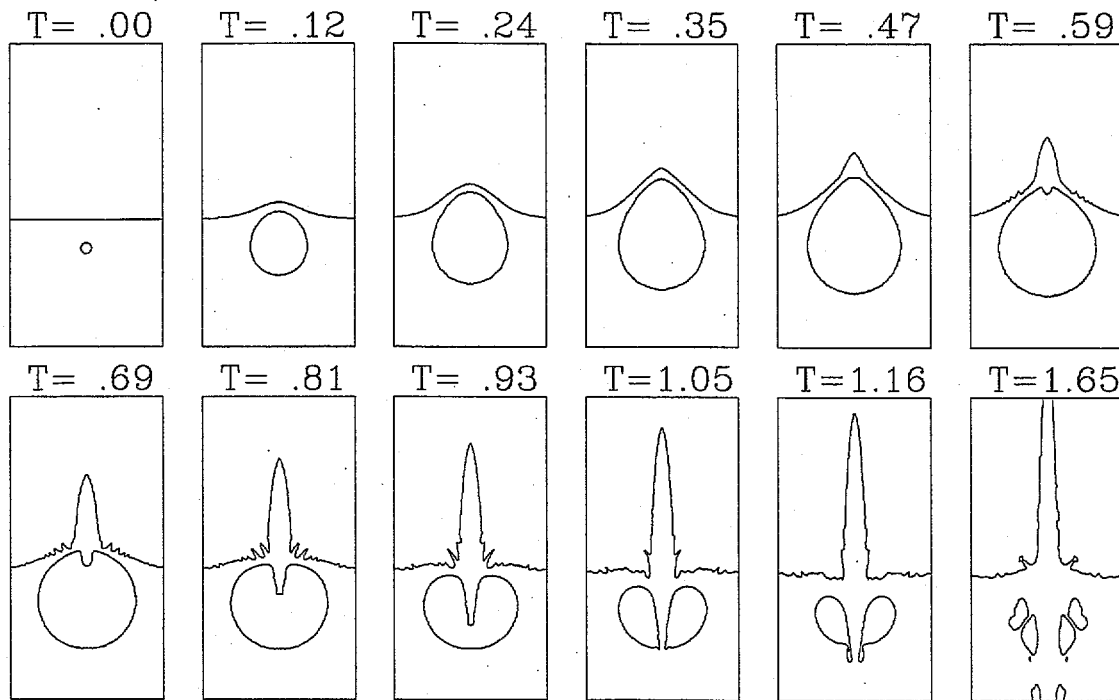


FIGURE 3-8. COMPUTATED EFFECTS OF THE FREE SURFACE ON THE MAXIMUM EQUIVALENT BUBBLE RADIUS IN THE ABSENCE OF GRAVITY

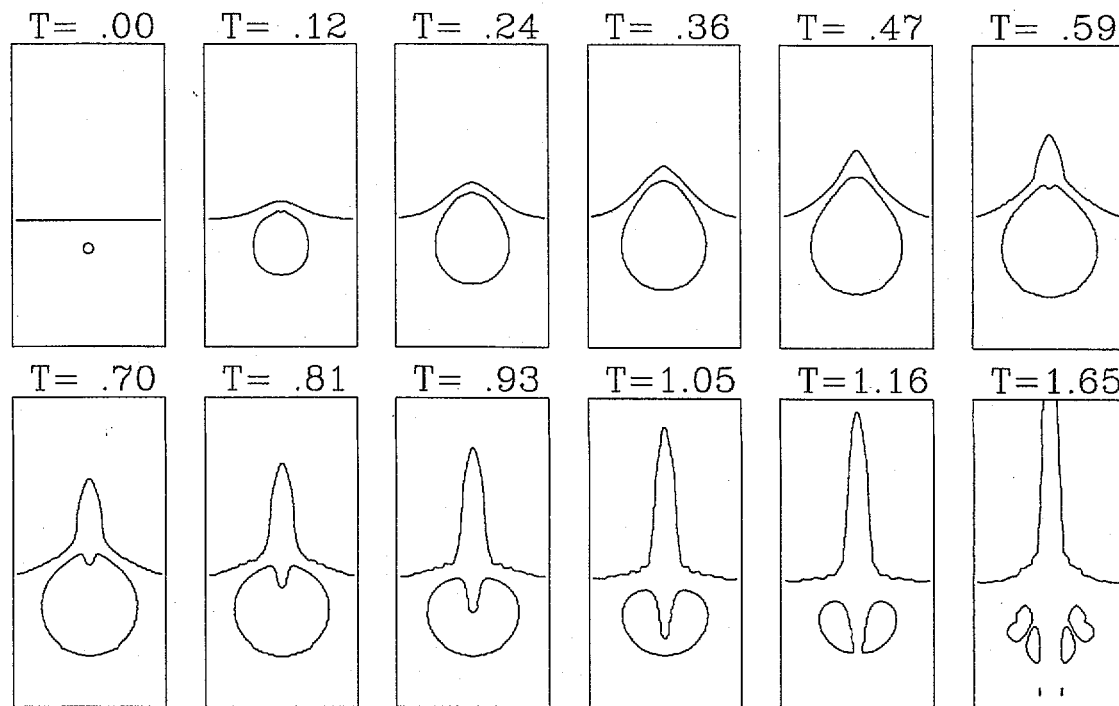
(A) EXPERIMENTS OF BLAKE AND GIBSON⁴

(B) FINE GRID COMPUTATIONS

FIGURE 3-9. SPARK BUBBLE AT SCALED DEPTH $C = 0.56$



(A) MEDIUM GRID



(B) COARSE GRID

FIGURE 3-10. GRID SIZE EFFECTS ON DENSITY CONTOURS

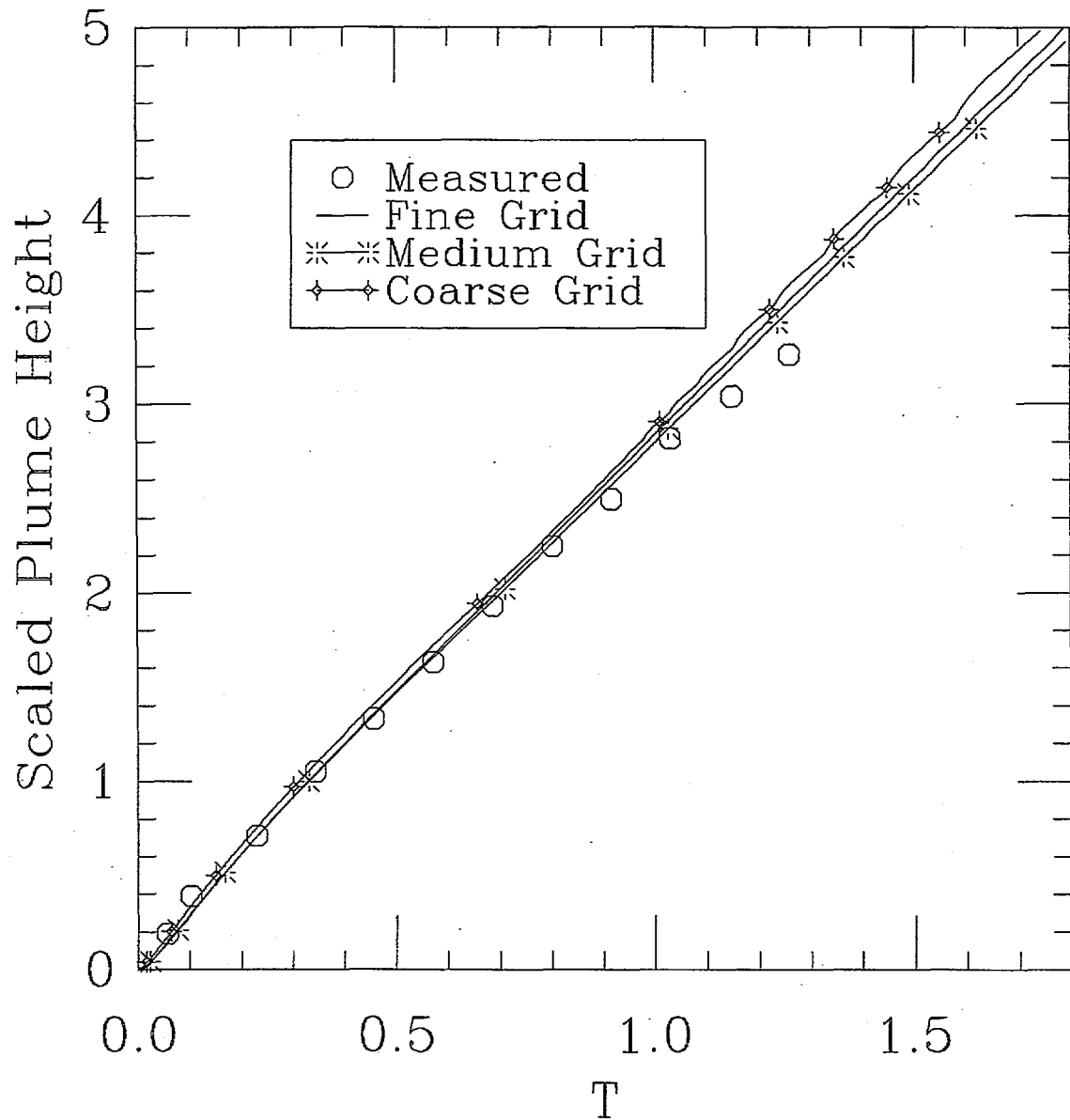


FIGURE 3-11. COMPUTED AND MEASURED PLUME HEIGHTS FOR THE $C = 0.56$ SPARK BUBBLE

CHAPTER 4

COMPARISONS TO EXPERIMENTS

In this chapter, data from shallow depth explosion experiments are presented and compared. These tests were conducted to both provide additional benchmark validations for our computational code as well as to demonstrate feasibility for creating an effective water barrier.³⁷ Three sets of experiments were conducted at different scales. The first set of experiments consisted of small (between 1- and 2-lb) individual charges detonated at the NSWCCD Test Pond in May 1993. Both above surface and below surface photographs were taken of these tests. These tests will be denoted with the prefix CD. The second set of tests were performed in the Arvon test facility (ARV) and consisted of both single and multiple 10-lb charges of Composition C-4. The experimental results were recorded using above surface cameras, in addition to the use of conductivity probes³⁸ and Microwave measurements.³⁹ Larger (25 lb) charges of PBXN-103 were tested at the Aberdeen Proving Grounds Briar Point facility (BP) in June, 1994.^{40,41} The particular shots focused on are listed in Tables 4-1 and 4-2 below.

TABLE 4-1. SINGLE CHARGE TEST SHOTS

Shot Label	Charge Type	d (ft)	W (lb)	$A_{\max}(\infty)$ (ft)	C
CD-9	C-4	2.5	1.25	4.87	0.51
CD-10	Pentolite	2.5	1.72	5.38	0.46
CD-13	Pentolite	5.0	1.73	5.27	0.95
ARV-1	C-4	10.0	6.0	9.44	0.64
ARV-2	C-4	10.0	10.0	9.14	1.09
BP-8	PBXN-103	10.08	26.3	14.85	0.67
BP-9	PBXN-103	13.83	26.3	14.43	0.96

TABLE 4-2. MULTIPLE CHARGE TEST SHOTS

Shot Label	Charge Type	d (ft)	W (lb)	N_c	S (ft)	M (lb/ft)	$A_{\max}^{(2D)}$ (ft)	C
ARV-3	C-4	8.0	10.0	5	8.0	1.25	11.55	0.69
BP-12	PBXN-103	10.1	26.3	5	10.1	2.61	20.83	0.48
BP-14	PBXN-103	13.8	26.3	5	13.8	1.90	17.02	0.81

The values listed for the scaled depth C in Table 4-1 were computed using the bubble parameters

listed in Table 3-7, together with equations (3-7) and (3-14). In Table 4-2, $C = d/A_{\max}^{(2D)}$, where $A_{\max}^{(2D)}$ was computed using (3-18a) using a cylindrical bubble assumption. Also listed in Table 4-2 are N_c , the number of charges used for the shot, S , the standoff (distance) between charges, and $M = W/S$, the mass per unit length.

COMPUTATIONAL GRIDS

The grids used in this study have essentially the same structure as those used in the spark bubble comparisons described in Chapter 3. That is, they are comprised of a uniform grid region of square cells that extend slightly past the bubble at its largest size. Outside this region, the grids are extended by stretching so that the computational boundaries correspond to the experimental conditions, whenever possible. For example, in all cases, the bottom computational boundary corresponds to the location of the bottom below the charge. Although the other boundaries of the test sites were not axisymmetric or two-dimensional they were generally sufficiently far away from the charge as to have a negligible effect on the bubble dynamics.

It follows from (3-18) that the maximum to minimum bubble radii is much larger in the two dimensional cylindrical case than for spherical bubbles. For example, for the cases listed in Table 4-2, the values of $\alpha^{(2D)}$ corresponding to two-dimensional approximations to shots ARV-3, BP-12, and BP-14, are 58.5, 44.1, and 42.3, respectively. Using a single uniform grid capable of resolving both the bubble at its minimum size, while extending past the bubble at its maximum size would require an excessive number of grid points. However, this problem can be alleviated using two separate grids.

Initially a grid that is fine in a region surrounding the charge was used until the bubble approached the boundary of the fine region. Then the solution was remapped, conserving mass and momentum, onto a grid that was coarser than the fine region of the first grid, but still able to resolve the bubble after the initial grid had been used. This second grid was uniform in a large enough region to contain the important long time dynamics of the problem. For example, the initial grid for shot BP-12 consisted of 40×98 square cells with size $h = 0.1$ in the region $0 \leq r \leq 4.0$ intersected with $-15.0 \leq z \leq -5.2$. Outside this uniform region the cells were stretched radially to $r = R_L = 160$ using 40 additional grid lines, and downward to $z = Z_b = -54$ using 30 grid lines. Above the uniform region the spacing in the z direction was uniformly set to $\Delta z = 0.2$ in the region $-5.2 \leq z \leq 4.0$. The initial grid was used for $0 \leq t \leq 0.015$ sec, while the cylindrical bubble grew from its initial radius of 0.47 ft, to 3.3 ft. The computed solution at $t = 0.015$ was then remapped onto a second grid having square cells of size $h = 0.3$ in the region $0 \leq r \leq 24$, intersected with $-30 \leq z \leq 30$. As with the initial grid domain, the second grid was stretched radially to $r = R_L = 160$ using 40 grid lines, and downwards to $z = Z_b = -54$ using 30 grid lines. Above $z = 30$ the grid was also stretched upwards using the stretching $\Delta z_j = 1.1\Delta z_{j-1}$, with the additional restriction that $\Delta z_j \leq 15$. Using 50 grid lines above the uniform region allowed the computational domain to extend to $z = Z_T = 326$.

While the initial grid is used for only a small fraction of the first bubble period, the computations were carried out for several periods on the second grid. Typically, the use of the initial grid

represents approximately 2 percent of the total computational effort. For this reason, the second grid is referred to as the "principle" grid. Since it was also observed to slightly improve the single shot computations (it typically reduced the error by 0.5 percent) we adopted this methodology for all the runs. A summary of the cell sizes in the uniform regions and total numbers of cells ($N \times M$) used for all the computations are listed below in Table 4-3.

TABLE 4-3. SUMMARY OF COMPUTATIONAL GRIDS AND RESULTS

Shot Label	Initial Grid		Principle Grid		Bubble Period (sec)		Maximum Radius (ft)		Radius Ratio α
	h	$N \times M$	h	$N \times M$	T_{meas}	T_h	A_{Max}^{meas}	A_{max}^h	
CD-9	0.05	70 X 150	0.1	80 X 275	-	0.180	4.57	4.53	15.8
CD-10	0.05	70 X 150	0.1	80 X 280	-	-	5.50	5.44*	16.5
CD-13	0.05	70 X 180	0.1	82 X 281	0.212	0.216	5.75	5.12	16.1
ARV-1	0.1	70 X 160	0.2	80 X 270	0.34	0.344	-	9.03	15.3
ARV-2	0.1	90 X 270	0.2	80 X 290	-	0.363	-	8.93	14.8
BP-8	0.125	74 X 175	0.25	96 X 299	0.542	0.540	-	14.47	12.5
BP-9	0.125	70 X 220	0.25	96 X 284	0.544	0.558	-	14.31	12.1
ARV-3	0.05	100 X 280	0.2	100 X 290	-	0.558	-	10.94	58.5
BP-12	0.1	80 X 174	0.3	120 X 280	-	0.872	-	19.30	44.1
BP-14	0.1	80 X 183	0.3	120 X 280	-	0.897	-	16.58	42.3

The cell sizes in the principle grid uniform region were selected so that $A_{max}/h \approx 50$, corresponding to the "medium" grid used for the spark bubble comparison, and the $h = 0.2$ grid listed in Table 3-1. Therefore, when the ratio $\alpha = A_{max}/A_{min} \approx 10$, it can be expected that the error in computing the period or maximum radius will be approximately 2 percent. For the single shot cases listed in Table 4-3, the values of α are slightly larger than 10, and the error can be expected to be approximately 2.5 percent. The initial grid uniform cell sizes were generally selected so that $A_{min}/h > 4$ to adequately resolve the bubble at its smallest size.

Also listed in Table 4-3 are the computed and available measurements of bubble periods and maximum radii. The agreement in all cases, except for the maximum radius for shot CD-13, provides an additional justification for using the empirical values listed in Table 3-7. With the exception of shot CD-10, which is expected to vent, all computations were performed using $\epsilon_A = 0.5$ for $0 \leq t \leq 0.8T_{d,b}$, where $T_{d,b}$ was computed using (3-19) as an approximation to the period. For $t > 0.8T_{d,b}$, the value was decreased to $\epsilon_A = 0.1$ (see Chapter 2). For shot CD-10, the value of ϵ_A was varied, and the results presented in the next section.

* Maximum width of vented cavity.

BUBBLE PROFILE COMPARISONS

We begin our validations by comparing computational bubble shapes and sizes to the underwater photography performed at Carderock. For all figures in this chapter the units of distance are measured in feet, and time is measured in seconds. Figure 4-1 shows the computed and measured outlines of the bubble and plume at $t = 0.1$ sec for shot CD-9, which roughly corresponds to the time of maximum bubble size. For the computations, two contours of density are shown, namely $\rho = 0.9\rho_0$ and $\rho = 0.01\rho_0$. Note that the lower valued contour provides a better match for the plume outline. The fact that these contours are widely separated in the plume indicate an instability at the air-plume interface. This is because of the plume's downward acceleration (the bubble has a lower pressure than the air) and its upward velocity. Inside the bubble; however, the contours agree closely with each other and with the measurements. The quality of the photographs were not good enough to observe the downward moving jet which is predicted by the computations. For this example $A_{\max}^{\infty} = 4.87$, and the scaled depth $C = 0.51$ is close to the critical scaled depth when venting can be expected. The computed equivalent maximum radius (based on maximum volume) was $A_{\max}^h(C) = 4.53$. According to (3-36) the expected maximum radius, taking the free surface into account, is $A_{\max}(C) = 4.61$. Using the same grid resolution the computed maximum radius of a spherically symmetric bubble with the same initial conditions (and pressure at infinity set to the hydrostatic pressure at the charge depth) was $A_{\max}^h = 4.75$, representing an error of approximately 2.5 percent. This explains why the computed bubble is slightly smaller than the measurements and is slightly below the expected value of $A_{\max}(C)$.

An even shallower case was shot CD-10 ($W = 1.72$ lbs of Pentolite at a depth of $d = 2.5$ ft) which has a scaled depth $C = 0.46$. In this case the bubble is expected to vent. Figure 4-2 compares the computed and measured bubble outlines at $t = 0.10$ sec using 5 computations with different values of the air-water interface cutoff ϵ_A (cf. (2-3b)). When $\epsilon_A = 0.5$ (Figure 4-2(A)) venting did not occur and the computed bubble is substantially smaller than the observations. Using $\epsilon_A = 0.4$ causes the bubble to eventually vent at time $T_v = 0.076$, but the bubble profile is not greatly effected at $t = 0.10$ (Figure 4-2(B)). However, the central water plume is slightly narrower and the density contour $\rho = 0.01\rho_0$ is higher than in the previous case. As ϵ_A is decreased (Figure 4-2(C-E)) the bubble vents earlier, causing the cavity to get larger. In Figures 4-2 (D) and (E) the outline of the cavity is in good agreement to the photographic observations. Also, the amount of water in the central region is greatly decreased as the bubble vents earlier. However, as mentioned in Chapter 2 the venting of the bubble is crudely approximated in our model, with the pressure in the cavity instantaneously changing from the value it had before the bubble vents to the constant and uniform atmospheric pressure. Therefore, long time predictions of bubbles which have vented cannot be expected to be reliable.

PLUME COMPARISONS

At early times after detonation the plume outlines were observed clearly in the photographic records. Comparisons of the observed plume heights and widths provide a critical validation of the computational model.

Single Charge Plume Heights

Figure 4-3 shows the measured and computed values of the plume heights for the Carderock shots CD-9, CD-10, and CD-13. The computations for CD-9 were the same as shown in Figure 4-1. The plume heights for CD-10 were taken from the same computation depicted in Figure 4-2(C) (with $\epsilon_A = 0.3$). For the computations, the plume height was defined to be the highest z value for which $\rho \geq 0.01\rho_0$. The "ripples" in the computed plume heights are due to the coarse stretched grids which were used above $z = 13$ ft. While the agreement for the shallow cases (CD-9 and CD-10) is very good, the computation for shot CD-13, where the scaled depth is $C = 0.95$, underestimates the measured plume heights by over 30 percent.

The underestimation of plume heights (using an incompressible liquid assumption) has been discussed by Kedrinski,⁵ who also noted that early time plumes will be enhanced if the surface is indented above the charge. Such a recess would be caused by the spallation region caused by the interaction of the shock with the free surface. Since our model uses an incompressible assumption for water, this phenomenon cannot be predicted directly using our methodology. However, we can simulate this shock effect by modifying the initial conditions. For example, instead of initializing the free surface to be flat ($z = 0$), we can recess the surface by "cutting out" a spherical region with radius R_i centered at $z = d$, where $z = -d$ is the initial charge location. The computed plume heights for shot CD-13, repeated with an initial recess radius $R_i = 1.03d$, are also displayed in Figure 4-3. The discrepancy between the measured and computed data in this case is greatly reduced.

Computational grids used for the Arvonja shots were twice the size as those used for the Carderock computations so that the relative resolution A_{\min}/h was the same as for shot CD-9. Figure 4-4 shows comparisons of measured and computed plume heights for shots ARV-1 and ARV-2. In each case the computations with an initially flat free surface underpredicted the plume heights by 30 percent to as much as 50 percent. As with shot CD-13, this discrepancy was greatly reduced with the choice $R_i = 1.03d$, for both cases.

Figure 4-5 compares the initial plume formation for shot ARV-1 based on computations using a recessed and flat initial free surfaces. Here, the density contour $\rho = \rho_0$ is displayed. In the recessed case, a thin jet of water forms at an early time and precedes the thicker "main" column which would appear without the recess. This recess has little or no influence on the bubble dynamics under the surface.

The empirical value $R_i = 1.03d$ was also used for charges of PBXN-103. Figure 4-6 includes measured and computed plume heights for shots BP-8 and BP-9 performed at the Briar Point Facility of the Aberdeen Proving Grounds. These shots were conducted with 25 lb charges of PBXN-103 with a 2.5 lb C-4 booster. This is roughly equivalent to a 26.3 lb charge of PBXN-103. For shot BP-9, where $C = 0.96$, the plume heights are substantially underestimated with $R_i = 0$. For the early times, $0 \leq t \leq 1.0$, the computed heights with $R_i = 1.03d$ are 20 to 25 percent below the measured values. However, this discrepancy disappears at later times. For shot BP-8 ($C = 0.67$) the initially flat surface yielded predictions that were over 50 percent under the measured values. As with shot BP-9, the computations using $R_i = 1.03d$ underestimated the measured values at the early times ($0 \leq t \leq 0.7$). We conjecture that this underestimation is caused by the initial shock dome of

spalled water which is not modeled in our simulations. At later times the computed heights become slightly greater than the measured values. Other effects, such as the plume breakup and drag forces, may become significant at these times.

Based on these results as well as those displayed in Figures 3-11 and 4-3, the value $R_i \approx 1.03d$ appears to provide a reasonably good match to plume height data for scaled depths C in the approximate range $0.6 \leq C \leq 1.1$ for both C-4, Pentolite, and PBXN-103 charges. The use of the initially indented surfaces had a negligible effect on the computed periods and maximum bubble radii (< 0.1 percent) for the cases considered. The computed values listed in Table 4-3 were unaffected by the use of the indented initial surfaces.

Multiple Charge Plume Heights

We now turn our attention to the multiple charge shots listed in Table 4-2. In the cases considered the distance between the individual charges was less than the free field maximum radius of the single charges. For example, a single 10-lb charge of C-4 at a depth of 8 ft has a free field maximum bubble radius of 9.29 ft, which is larger than the standoff distance between charges of 8 ft for shot ARV-3. The corresponding single charge values for shot BP-12 and BP-14 are listed in Table 4-1 ($A_{\max}(\infty)$ values for shots BP-8, and BP-9, respectively). In such cases, it can be expected that the individual bubbles will merge into a nearly cylindrical bubble (given a sufficient number of charges). Therefore, a two-dimensional approximation may be reasonable near the center of the line of charges.

Figure 4-7 compares the measured and computed plume heights for shots BP-12, and BP-14. For a simultaneous detonation of multiple charges, spallation can be expected not only above each charge, as in the single shot case, but also in between the charges due to the interaction of the shock intersections with the free surface. Shock interactions from underwater spherical charges have been studied by Stebnovskii⁴² and by Coleburn and Roslund,⁴³ but not in conjunction with the air-water surface. This interaction effect is clearly seen in the images taken from video tapes of shots BP-12 and BP-14. A sequence of these frames appear in the top half of Figure 4-8 (shot BP-12) and Figure 4-9 (shot BP-14). In each case four distinct "peaks" are clearly observed at early times, which jet upwards from the midpoints of the five underwater charges. The fact that this effect can be seen in the first video frame after the detonation (at $t = 0.03$) supports the conjecture that this is a shock effect. In Figure 4-7, both the measured heights of the peaks, and the "valleys" are plotted for shot BP-14. The computations are closer to, but still below the measured heights of the valleys. This discrepancy is probably caused by the spallation directly above each charge as occurred with the single shot cases previously discussed.

As with the single shot cases, multiple shot shock effects can be modeled empirically by initializing the air water surface with recesses corresponding to where spallation occurs. In addition to a recess directly above each charge, the surface should also include recesses in between the charges, where shock focusing is expected. This latter recess could be modeled as the region of intersection between spheres centered at reflected points located a distance $2d$ above each charge. This model

is shown in Figure 4-10. Testing this model computationally requires the use of our three-dimensional code *BUB3D* which will be done in a forthcoming paper.

Secondary Plumes - Long Time Behavior

To better understand the quantitative comparisons of plume densities, we must also qualitatively examine the long time plume dynamics. The long time plume behavior can be seen in Figures 4-8 and 4-9 for multiple shots BP-12, and BP-14, and in Figures 4-11, and 4-12 for single shots BP-8 and BP-9. The computational results for all four cases are shown using gray scale density contours. A middle value of gray was used to shade the region $0.5\rho_0 \leq \rho \leq \rho_0$. For values of $\rho < 0.5\rho_0$ the gray scale was lightened using linear interpolation, so that $\rho = 0$ corresponds to white. The size scale used for the contour frames is roughly the same as in the photographic frames in each case. As indicated in the computational frames, the top of the video frames corresponds to a height of approximately 90 ft. We remark that in regard to the multiple shot cases in Figures 4-8 and 4-9, the photographic view is at nearly a right angle to the computational contour of the plume and bubble cross section.

The single shot examples shown in Figures 4-11 and 4-12 begin similarly as the previous examples shown in Figures 3-9, 4-1, and 4-5. Here, two central jets, a large one rising into the atmosphere and a smaller one falling into the bubble, form between the bubble and air surface as the bubble begins its first contraction. The downward moving jet can be observed in the computed frame labeled $T = 0.41$ in Figure 4-11. The downward jet is just beginning to form at time $T = 0.41$ for shot BP-9 (Figure 4-12) and by $T = 0.61$ has collided with another thicker jet moving upward from the bottom of the bubble. For a further discussion on the formation of jets in bubbles near a free surface see Blake et. al.,³⁴ who also provides an analysis of such phenomenon through the use of the Kelvin impulse concept.

The photographs of single shot BP-8 in Figure 4-11 show a persistent central column, which appears to be initially surrounded by spray, but at later times appears to be a thin column of water. Although this column appears to be thinner in the computations, its height and persistence are matched very well, even through the last frame at time $t = 5.8$ sec. The long time plume heights are also reproduced accurately by the computations for shot BP-9, as shown in Figure 4-12.

An interesting effect that appears both in the computation and photographs is the emergence of secondary plumes ejected upward and radially away from the central column. These plumes can be seen emerging during the bubble's second expansion. In Figure 4-11, at time $t \approx 0.8$ the ejection of these plumes can be seen in both the computation and the photograph. The computed and photographed heights of these secondary plumes are in good agreement, although the widths, (or angles from the vertical) are somewhat narrower in the computation. The secondary plumes appear a little later in the photographs of shot BP-9 (Figure 4-12). In this case, the fallback of the radial plumes were matched well by the computation, but the width and height are slightly overestimated. The ability to capture the secondary plume phenomena, even qualitatively, is a difficult task due to the complex structure of the bubble surface and the relatively long time it takes to develop.

Note that these secondary plumes also appear in the multiple charge shots displayed in Figures 4-8 and 4-9. The emergence of these plumes is evident by time $t = 1.2$ for both shots. The two dimensional computations predict the emergence of the secondary plumes at times roughly coinciding with the photographs. For both of these multiple charge shots, the central plume falls faster in the computation than in the experiment, particularly for shot BP-14. This can be expected since the central plume heights are underpredicted. As mentioned earlier, we expect this discrepancy to be reduced by including the three-dimensional shock effects, using the empirical model described in Figure 4-10. Another phenomenon that will effect the duration of the plume is the drag on the small water droplets as they fall with gravity. As the plume breaks up into small droplets or spray, this effect can become significant. Droplet breakup and drag effects are currently not included in our model.

MICROWAVE COMPARISONS

Quantitative measurements of the plume density were made using microwave measurements. These measurements were based on the amount of microwave absorption through the plume. Microwaves were sent and received using a pair of three foot radius parabolic dishes placed on either side of the plume at equal heights above the water surface.³⁸ To compare the microwave measurement with the computed densities, the computed values were integrated within a cylindrical region of radius 3 ft between the microwave dishes. In Cartesian (x, y, z) coordinates this integral is

$$I^n = \int_{H_D-R_D}^{H_D+R_D} \int_{-R(z)}^{R(z)} \int_{-\infty}^{\infty} \rho^n(x, y, z) dx dy dz \quad (4-1)$$

where H_D is the height of the center of the dish, R_D is the radius of the dish, ρ^n is the density at time t^n , and

$$R(z) = \begin{cases} \sqrt{R_D^2 - (z-H_D)^2} & \text{if } |z - H_D| \leq R_D, \\ 0 & \text{otherwise.} \end{cases} \quad (4-2)$$

The integral I^n corresponds to the total mass of water in the cylindrical region between the two dishes straddling the plume at time t^n .

For the two-dimensional approximations, ρ^n does not change in the y direction (parallel to the line of charges, and perpendicular to the line between the microwave dishes). By symmetry across $x = 0$ it follows that

$$I^n = 4 \int_{H_D-R_D}^{H_D+R_D} R(z) \int_0^{\infty} \rho^n(x, z) dx dz. \quad (4-3)$$

This integral is approximated using the midpoint rule quadrature

$$I^n \approx I_h^n = 4 \sum_{j=J_1}^{J_2} R(\tilde{z}_j) \sum_{i=1}^{N_i} \rho_{i,j}^n (\Delta x)_i (\Delta \tilde{z})_j, \quad (4-4)$$

where $\rho_{i,j}^n$ is the computed cell centered density of cell (i, j) ,

$$\bar{z}_j = \frac{z_j^T + z_j^B}{2}, \quad (\Delta \bar{z})_j = z_j^T - z_j^B, \quad (\Delta x)_i = x_{i+1} - x_i,$$

$$z_j^T = \min(H_D + R_D, z_{j+1}), \quad z_j^B = \max(H_D - R_D, z_j),$$

and J_1 and J_2 are indices such that $z_{J_1} \leq H_D - R_D$, and $z_{J_2} \geq H_D + R_D$. In the above, cell (i, j) corresponds to the rectangular region $x_i \leq x \leq x_{i+1}$, $z_j \leq z \leq z_{j+1}$ for $i = 1, \dots, N$ and $j = 1, \dots, M$.

In cylindrical (r, θ, z) coordinates the integral (4-1) can be written as

$$I^n = 4 \int_{H_D - R_D}^{H_D + R_D} \int_{\theta=0}^{\frac{\pi}{2}} \int_{r=0}^{R(z)/\cos(\theta)} r \rho^n(r, z) dr d\theta dz. \quad (4-5)$$

This integral is approximated on the computational grid using the quadrature

$$I_h^n = 4 \sum_{j=J_1}^{J_2} \sum_{l=1}^{M_\theta} \left[\sum_i \tilde{r}_i \rho_{i,j}^n (\Delta \tilde{r})_i \right] (\Delta \theta)_l (\Delta \bar{z})_j, \quad (4-6a)$$

where

$$\tilde{r}_i = \frac{r_i^R + r_i^L}{2}, \quad (\Delta \tilde{r})_i = r_i^R - r_i^L, \quad \tilde{\theta}_l = (l - 1/2) \frac{\pi}{2M_\theta}, \quad (\Delta \theta)_l = \frac{\pi}{2M_\theta}, \quad (4-6b)$$

$$r_i^R = \min(R_{j,l}, r_{i+1}), \quad r_i^L = \min(R_{j,l}, r_i), \quad R_{j,l} = \frac{R(\bar{z}_j)}{\cos(\tilde{\theta}_l)} \quad (4-6c)$$

Note, that the values \tilde{r}_i depend implicitly on the indices l and k as indicated by (4-6b) and (4-6c) due to the variable limits of integration in the r coordinate.

For the actual comparisons, the total mass values I^n were scaled by both the cross sectional area of the cylinder and the water density to obtain an "effective water length" (EWL). This value

$$EWL^n = \frac{I^n}{\rho_0 \pi R_D^2} \quad (4-7)$$

corresponds to the *length* of water filling the cylinder having an equivalent mass as the plume at time t^n .

Before proceeding with the comparisons, note that because of the novelty of using microwave absorption to measure plume densities, no independent validation of this procedure is currently available. Therefore, these comparisons should be considered in conjunction with the plume height data, photographs, measured bubble periods, and the probe measurements in the following section, whenever these were available. In this way, the microwave comparisons provide validations not only for the computations, but for the measurements as well.

Figures 4-13 and 4-14 display measured and computed microwave data for the single charge shots ARV-1 and ARV-2. For all the Arvonja shots, the microwave measurements were taken at a height $H_D = 25$ ft. The measured data for shot ARV-1 show an initial rise in the *EWL* from 0 to 0.2 occurring between 0.2 and 0.25 sec after detonation. There is an inflection point in the measured data at approximately $t = 0.25$, after which the *EWL* spikes to a value of approximately 1.6 at time $t = 0.55$. Using an initially flat surface, the computed data ($R_i = 0$) misses the inflection point entirely, and the *EWL* increases from 0 to approximately 0.8 in the time interval $0.3 \leq t \leq 0.6$. However, the computed *EWL* using an initially recessed surface ($R_i = 1.03d$) indicates an initial rise from 0 to 0.1 during the time interval $0.2 \leq t \leq 0.3$ with an inflection point at approximately $t = 0.35$. Based on this data, it is reasonable to expect that the first inflection point (or kink) in the measured data is due to shock effects (cf. Figures 4-4 and 4-5). Furthermore, the empirical model used to simulate these effects appears to underestimate the *EWL* before the initial kink. This can be expected since the spray dome that is spalled upward due to the shock reflection is not included in the computations. At later times both computations show a peak in the *EWL* at $t \approx 1$, with the $R_i = 0$ computation predicting *EWL* values approximately 30 percent larger than the $R_i = 1.03d$ computation in the time interval $1.0 \leq t \leq 2.2$. The computed peaks in the *EWL* occur when the secondary plumes pass through the microwave cylinder. Even though this event was not reproduced in the measured data, the overall agreement is reasonable, at least from the point of view of giving the correct order of magnitude for the *EWL* most of the time. At late times the measured data lies above the computed data.

Figure 4-14 displays a more dramatic difference in the computations using a flat and indented initial free surface. Here, the flat surface computation yields completely erroneous results, indicating no plume density until after $t = 1.6$ sec while the measurements and observed plume heights (cf. Figure 4-4) indicate that the plume enters the microwave cylinder at approximately $t = 0.6$. Furthermore, the $R_i = 0$ computation also predicts a rise in *EWL* values between $t = 1.6$ and $t = 3.0$. This effect was caused by a rebounding jet that formed after the computed bubble vented shortly after the time of the second bubble maximum. However, the computed *EWL* values with the initially recessed surface ($R_i = 1.03d$) are in excellent agreement with the measurements. The slight delay (approximately 0.2 sec) in the initial rise and decline of computed *EWL* values corresponds to the underestimation of initial plume heights as indicated in Figure 4-4. The difference between the measured and computed peak values in this case is only approximately 12 percent. Also, unlike the $R_i = 0$ computation, the bubble did not vent after the second bubble maximum, and no rebound jet formed. This example demonstrates, that in certain cases, particularly for values of $C \approx 1$, even the long time dynamics can be sensitive to relatively minor changes in the initial conditions (e.g., recessed surfaces caused by shock effects).

Figure 4-15 compares the measured and computed microwave data for multiple shot ARV-3 (cf. Table 4-2). The microwave equipment was calibrated only for values $EWL < 1.58$ for these experiments as indicated by the plateau in the measured data for $0.7 \leq t \leq 2.7$. Despite the underprediction by the computations between $2.0 \leq t \leq 3.0$, once again the agreement is good. The initial rise times agree to within 0.05 sec. The two peaks in the computations at approximately

$t = 0.7$, and $t = 1.35$ correspond to the rising of the central plume followed by the rise of the secondary plumes, through the microwave cylinder. The "bumps" at the later times correspond to parts of the plume structure falling back through the cylinder toward the surface. As in Figure 4-13, the measured *EWL* values take longer to decay to 0, possibly because of the unmodeled drag forces.

Figure 4-16 compares the computed and measured *EWL* for shot BP-8 at the two heights $H_D = 25$ and $H_D = 12.5$. The results using $R_i = 1.03d$ are slightly better, primarily at early times at $H_D = 25$. At this height at later times, the computations indicate that there is approximately twice as much water as measured using the microwave absorption data. This is somewhat surprising, when the photographs of Figure 4-11 are taken into consideration. As noted earlier, the computed plumes appear to be substantially thinner than in the photographs. If the microwave measurements are accurate, the actual plume must not be very dense, even through the middle. However, the persistence of the central plume suggests a relatively dense core in the plume, as the computations predict. It is also possible that the microwave measurements miss part of the plume at later times due to wind forces. A slight drift in the plume is noticeable in the photographs, particularly during its descent. At the height $H_D = 12.5$ ft, the microwave measurements saturated at $EWL = 0.9$. This comparison only indicates reasonably good agreement between rise and fall times for the *EWL* values.

Figure 4-17 compares the computed and measured *EWL* values for shot BP-9. For this case there is a large difference between the $R_i = 0$ and $R_i = 1.03d$ cases. When $R_i = 0$ the central jet does not quite reach a height of 25 ft, and the only measured water is produced by the secondary plumes. The computation with $R_i = 1.03d$ indicates an initial rise in *EWL* values after $t = 0.4$, about 0.2 sec later than the microwave data. This is consistent with the times that the plume heights approach 25 ft as indicated in Figure 4-6. The second *EWL* peak at $t = 1.0$ when $H_D = 25$ is due to the radial plume passing through the microwave cylinder. The radial plumes shown in the photographs of Figure 4-12 do not appear to contribute to the microwave data, and perhaps do not reach the height of 25 ft. In the computations the radial plumes rise above 30 ft and contribute significantly to the *EWL* values. This partly explains the overestimation of the computed *EWL* values for $t > 1.2$ sec. However, the photographs in Figure 4-12 shows a substantial amount of water in the plume at time $t = 2.53$ sec, which the microwave data fails to indicate.

At $H_D = 12.5$ both of the computations and the measurements are in good agreement for the initial rise of *EWL* values between $0.2 < t < 0.4$. The computations of the *EWL* values diverge after $t = 1.4$. This difference is similar to what occurred with the analogous computations for ARV-2 where the bubble vents shortly after its second bubble maximum in the $R_i = 0$ case. The high *EWL* values in this case are caused by the rebound jet passing through the microwave cylinder at $H_D = 12.5$. When $R_i = 1.03d$ the venting does not occur and the agreement with the measurements is much better. We remark that there is no evidence from the photographs of this rebound jet (cf. Figure 4-12). However, as with shot BP-8, the measured *EWL* values appear to fall too quickly, since the observed plume is above $H_D = 12.5$ until some time after $t = 3$, while the measured *EWL* values are negligible for $t > 2.2$.

Figure 4-18 compares the computed and measured *EWL* values for multiple charge shot BP-12. At both heights the initial rise times are predicted very well, while the computed values decay earlier (as occurred with shot ARV-3). Since the early time *EWL* values agree, while the computed plume heights were below the measurements (cf. Figure 4-7), it can be expected that the peaks of the plumes at early times do not contain a significant amount of water. Also note that the microwave dishes were centered above the central charge, which corresponds to the central valley of the initial plume structure (cf. Figure 4-8). The overall agreement between the computations and measurements in this case is good.

Finally, Figure 4-19 compares the computed and measured *EWL* values for multiple shot BP-14. Here the measured *EWL* rise times again show good agreement with the computed values. The computed *EWL* rise appears a little early at $H_D = 12.5$ and a little late at $H_D = 25$. The local peaks at $t \approx 1.2$ are caused by the secondary plumes passing through the microwave cylinders (cf. Figure 4-9). The peak value for the *EWL* at $H_D = 12.5$ of 22 ft at $t \approx 0.5$ is clipped off in the figure.

DENSITY PROBE COMPARISONS

A second set of plume density measurements were obtained through the use of conductivity probes. These probes were first developed by Phillips and Scott,⁴³ and consist of two parallel stainless steel rods. Phillips and Scott found that the conductivity through each probes was linearly proportional to the unwetted length of rod. These probes were originally used for measuring bubble radii from underwater explosions.

Lipton³⁸ suspended conductivity probes above the surface to obtain plume density measurements for both the Arvonja and Briar Point tests. Comparing the computed density at a specific location to the measured density from a single probe has little meaning for at least two reasons:

- (1) The free surface, and hence plumes, undergo periods of Rayleigh-Taylor instability. Therefore, point measurements cannot be expected to be reproducible. This is supported by the fact that probes located the same distance but on opposite sides of the charge center, yielded vastly different density histories.
- (2) The probes were suspended by a rope in the Arvonja tests which was deflected several feet upon impacts from the plumes. Therefore, the actual probe locations were not known.

Despite the instability, some degree of reproducibility can be expected from an integral norm. As with the microwave comparisons, the *EWL* value can be used, where the integration over the cylinder (4-1) is replaced by integration on a line. That is,

$$EWL^n = \frac{1}{\rho_0} \int_{-\infty}^{\infty} \rho(x, y_p, z_p) dx, \quad (4-8)$$

representing integration over the horizontal line located at $y = y_p$, and $z = z_p$. Note, that (4-8) is simply the limit of (4-7) and (4-1) as $R_D \rightarrow 0$. Since the probes were located at discrete points, a

trapezoid rule integration was used to determine the measured *EWL*. That is

$$EWL_p^n = \frac{S_p}{\rho_0} \left[\rho_1/2 + \sum_{i=2}^{n-1} \rho_i + \rho_n/2 \right] \quad (4-9)$$

where S_p is the uniform spacing between the n probes and ρ_i is the density at the i th probe location.

Comparisons with the simulations were made using the same formula (4-9), except the density values were interpolated from the computed cell density values. Using (4-9) on the computed data at the same locations as the probes is referred to as "Probe Integration" (P.I.). In addition, the computed values were integrated over the same grid that was used for the simulation. This "Full Integration" (F.I.) was used to determine if there was plume structure missed by the probes.

For the Arvonía tests eight probes were placed on a rope at a height 12.5 ft above the surface. The probes were placed 5 ft apart. Comparisons between the measured *EWL* values and the Computed values using both probe and full integration, are displayed in Figures 4-20, 4-21, and 4-22, for shots ARV-1, ARV-2, and ARV-3, respectively.*

In each case, the computed and measured initial rise times for the *EWL* values are in good agreement. For shots ARV-1, and ARV-2, this can be expected because of the agreement for the plume heights displayed in Figure 4-4. The data displayed for ARV-1 and ARV-2 in Figures 4-20 and 4-21, correspond to the computations with the initially recessed surface ($R_i = 1.03d$). Notice the F.I. values rise earlier than the P.I. values for these two cases. This is due to the fact that the central plume with the recessed surface is thin (see Figure 4-5). Therefore, it is not initially detected by the density values at the probe locations which are 2.5 ft on either side of the charge center. The computed and measured rise time of *EWL* values for multiple shot ARV-3 is excellent. This suggests that the height of the initial plume containing substantial water mass is accurately predicted by the computations.

It is obvious from these figures that there is little agreement for the *EWL* values. The large discrepancy between the computed P.I. and F.I. values suggests that the probe spacing is much too large to accurately portray the plume structure. Furthermore, it is also unlikely that the measured results are very reproducible, since the integration used for the *EWL* usually involved contributions from only 3 or 4 of the probes. Finally, the high-frequency oscillations in the measured data, also make comparisons difficult, unless these are substantially smoothed.

For the Aberdeen tests the number of probes was increased to 16, and the spacing between the probes was reduced to 2 ft.³⁸ Also, the probes were placed on a steel cable kept under high tension,

* The results shown here differ from those presented in Reference [38]. First of all, the measured values for ARV-2 in Reference [38] (Figures B-4, B-5, and B-6) are incorrect. Indeed, they appear to be the same values as for Arvonía Shot 1, with the peaks clipped at 2.5. The computed results presented here were also performed with initial conditions using the empirical constants presented in Table 3-7, while $\gamma = 1.3$ was used for all computational results presented in Reference [38]. Furthermore, the computational results presented there for Arvonía Shots 1 and 2 used an initially flat free surface.

probe line was offset 11.3 ft from the charge center for the single charge shots. Therefore, we expect that the central plume for the single charge shots will be missed by the probes, and only the radial plumes will be detected. The results for the single charge shots BP-8, and BP-9, are shown in Figures 4-23, and 4-24, respectively. In both cases, the computations indicate larger *EWL* values at earlier times than the measurements. With the exception of the time interval $1.3 \leq t \leq 2.0$ for shot BP-8 in Figure 4-23, there is little agreement between the measured and computed data.

Results for the multiple charge shot BP-12 are shown in Figure 4-25. Since the computed values using both the P.I. and F.I. quadratures produced similar results, only the P.I. values are shown. The computed *EWL* values show two distinct high peaks at approximately $t = 0.2$, and $t = 0.55$ sec. Peaks at corresponding times also appear in the measured data, but these are much smaller in magnitude. At $t = 0.32$ sec the top of the bubble is actually above the height of 12.5 ft as indicated in the computations shown in Figure 4-8. However, it appears that the cable as shown in the corresponding photograph has been significantly deflected upward. This deflection and relatively violent motion of the cable provides another possible explanation for the discrepancy at these times. For later times ($t \geq 0.6$), the agreement between the measured and computed *EWL* values is very good, until the probe data begins to vanish at about $t = 2.6$ sec. Indeed, with the high-frequency oscillations in the measured data providing an approximate bound for the experimental error, the computed data lies within or slightly above this bound for much of the interval, $0.6 \leq t \leq 2.6$.

The computed *EWL* values shown in Figure 4-25, are in good agreement with the computed microwave data in Figure 4-18. However, there are important differences between the *EWL* values determined using the microwave data and the probe data. At $H_D = 25$ ft, Figure 4-18 shows $EWL \geq 2.5$ for $0.2 \leq t \leq 3.2$. Since there will generally be more water at lower elevations, it can be expected that the *EWL* values using the data from the microwaves at a height of 12.5 ft would be substantially above 2.5 ft of water, had they not saturated. On the other hand, the probe data indicates that $EWL \leq 1$ for a substantial time in the interval $0.3 \leq t \leq 0.5$. It therefore appears that the magnitude of the *EWL* based on the probe data is substantially less than that indicated by the microwave data. Another notable difference between the microwave and probe measurements is the duration of the plume. While the probes indicate no substantial readings after 3 sec, the microwave data indicates significant measures of water after 6 sec. This may be due to the breakup of the plumes into small droplets. Since the probe must be totally wetted across the rods, any droplets smaller than the rod spacing will not be indicated. Furthermore, since the rods were pointed downwards, some shadowing could be expected from the falling plume. These limitations are also discussed by Lipton,³⁸ who concluded that the probes should tend to underestimate the water density.

Considering the fact that the computed probe data can be expected to underestimate the water density, the results for shot BP-14, depicted in Figure 4-26, show significant agreement. The general profiles, in particular the time and duration of the peak at time $t \approx 0.4$, and the overall decay of the *EWL* values, are in good agreement. The measured values are consistently about 50 percent below the computed values. The large computed *EWL* value at $t \approx 0.4$ is caused by the top of the water surface being pushed above the initial cable height of 12.5 ft. This can be seen in the

computed contour at $t = 0.32$ sec in Figure 4-9. The photograph at the corresponding time indicates very little deflection of the cable at this time, unlike the previous example where the agreement was much worse.

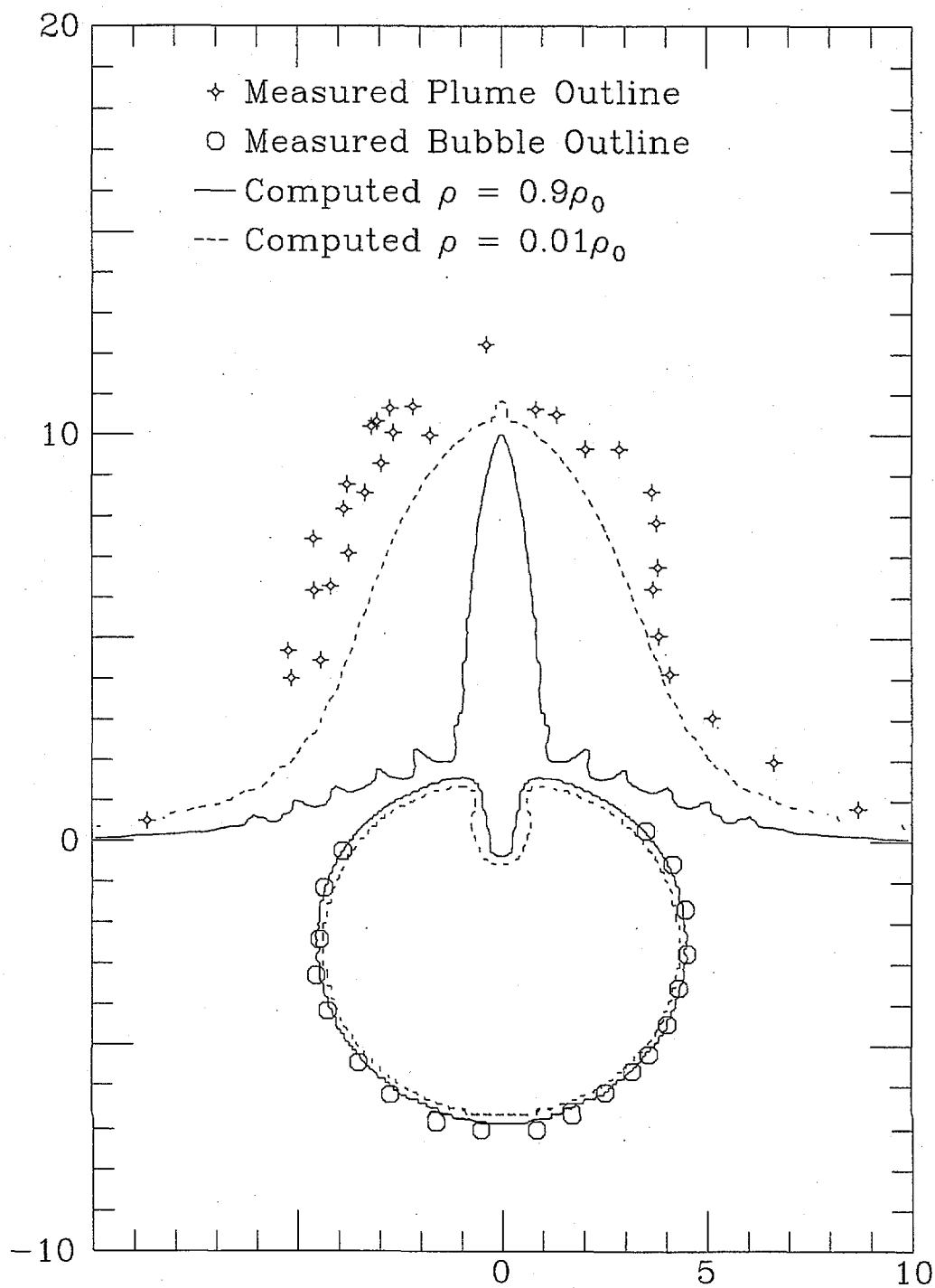


FIGURE 4-1. COMPARISON OF COMPUTED AND MEASURED BUBBLE AND PLUME OUTLINES FOR SHOT CD-9 AT TIME $t = 0.10$ SEC

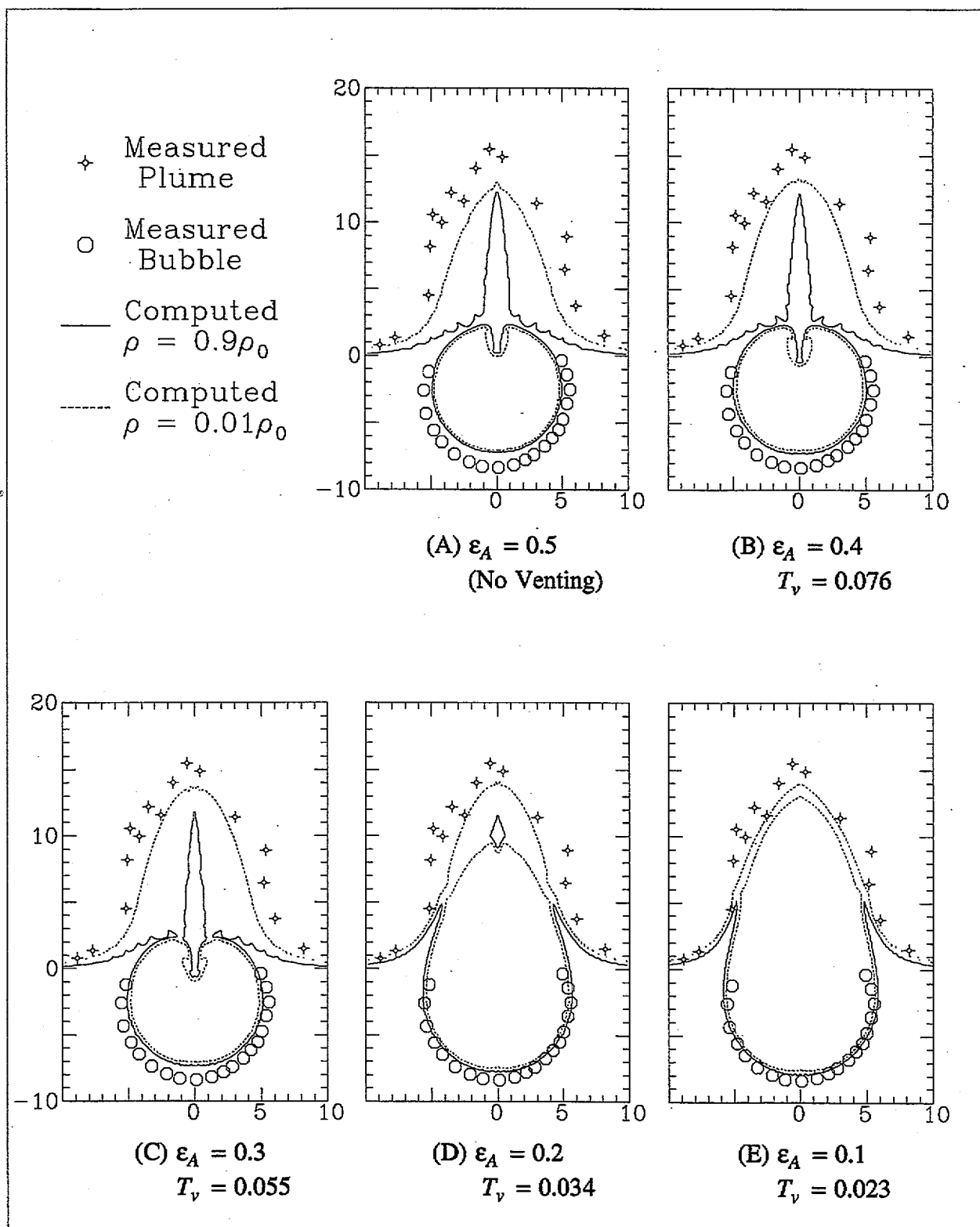


FIGURE 4-2. COMPARISON OF COMPUTED AND MEASURED BUBBLE AND PLUME OUTLINES FOR SHOT CD-10, (PENTOLITE, $W = 1.72$, $d = 2.5$) AT TIME $t = 0.10$ SEC FOR DIFFERENT VALUES OF ϵ_A

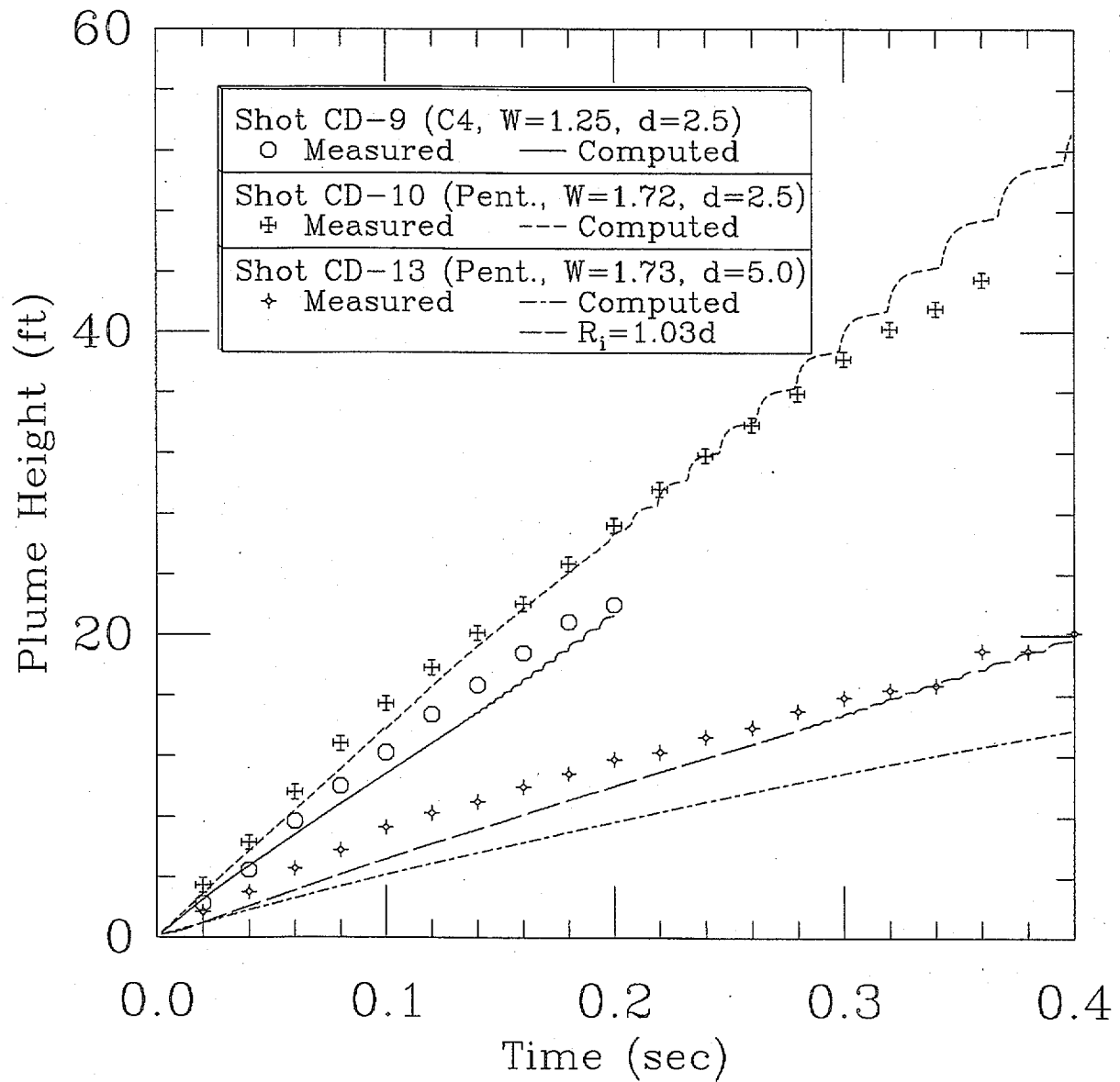


FIGURE 4-3. COMPUTED AND MEASURED PLUME HEIGHTS FOR CARDEROCK TEST POND SHOTS CD-9, CD-10, AND CD-13

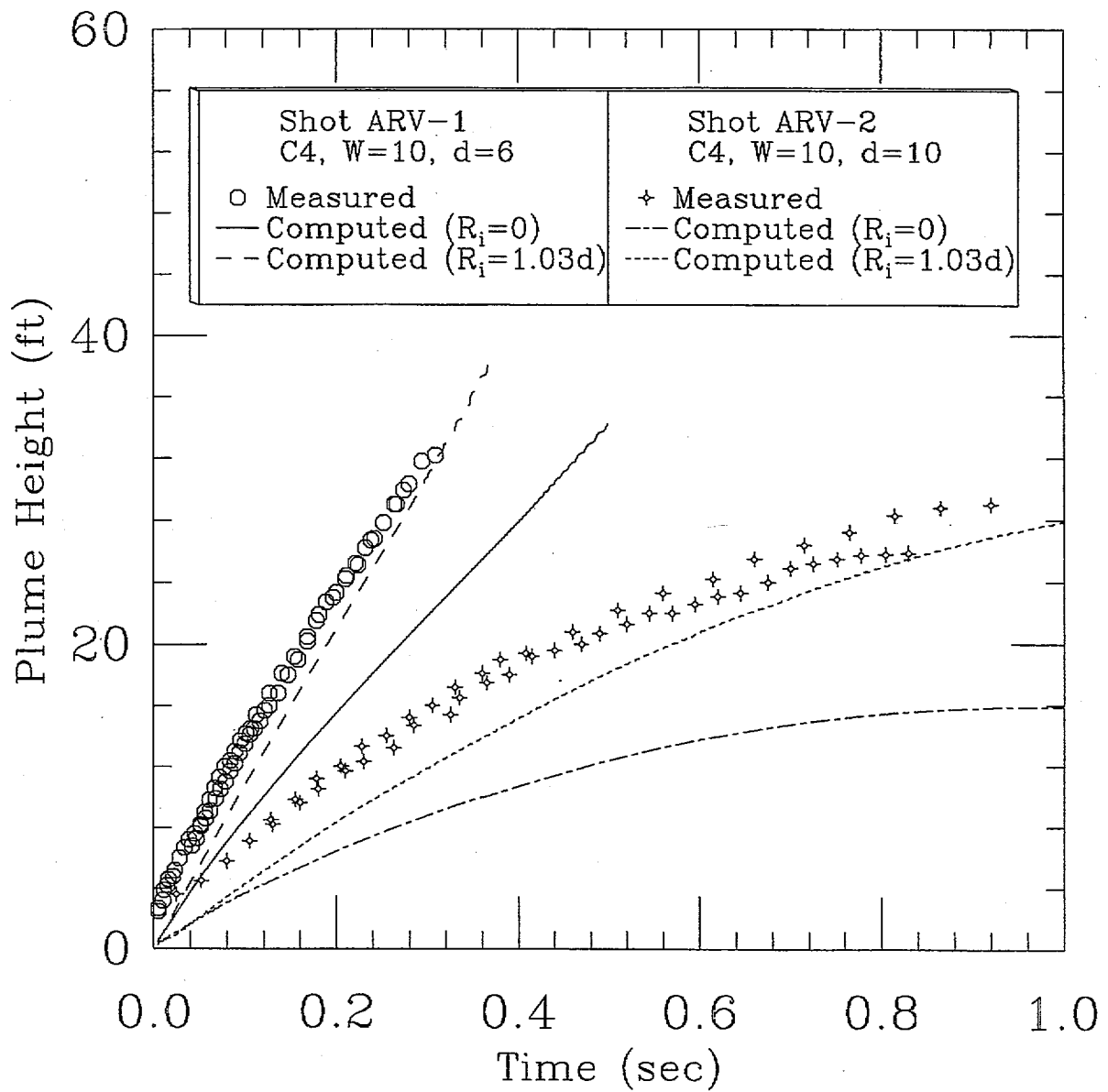
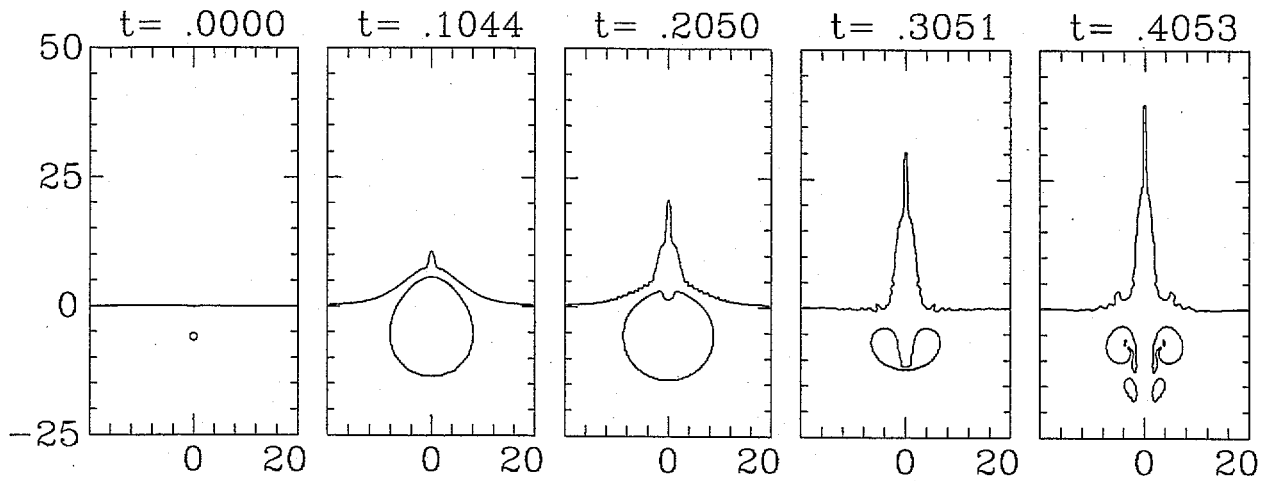
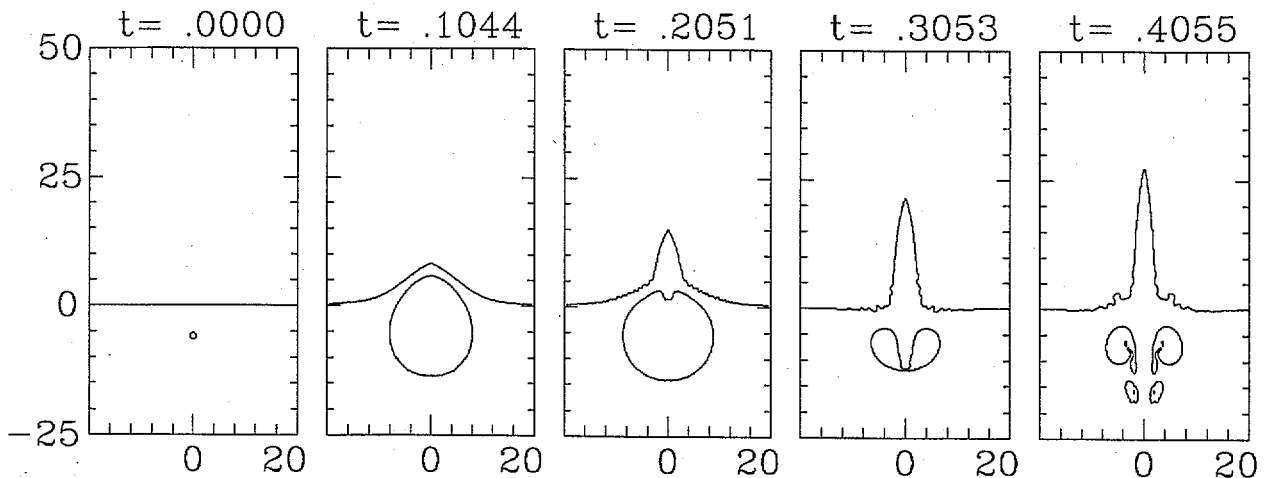


FIGURE 4-4. COMPUTED AND MEASURED PLUME HEIGHTS FOR ARVONIA SHOTS ARV-1 AND ARV-2

(A) INITIALLY RECESSED SURFACE $R_i = 1.03d$ 

(B) INITIALLY FLAT SURFACE

FIGURE 4-5. COMPUTED PLUME FORMATIONS FOR ARVONIA SHOT ARV-1
(C4, $W = 10$ lbs, $d = 6$ ft) USING AN INITIALLY RECESSED
AND FLAT FREE SURFACE

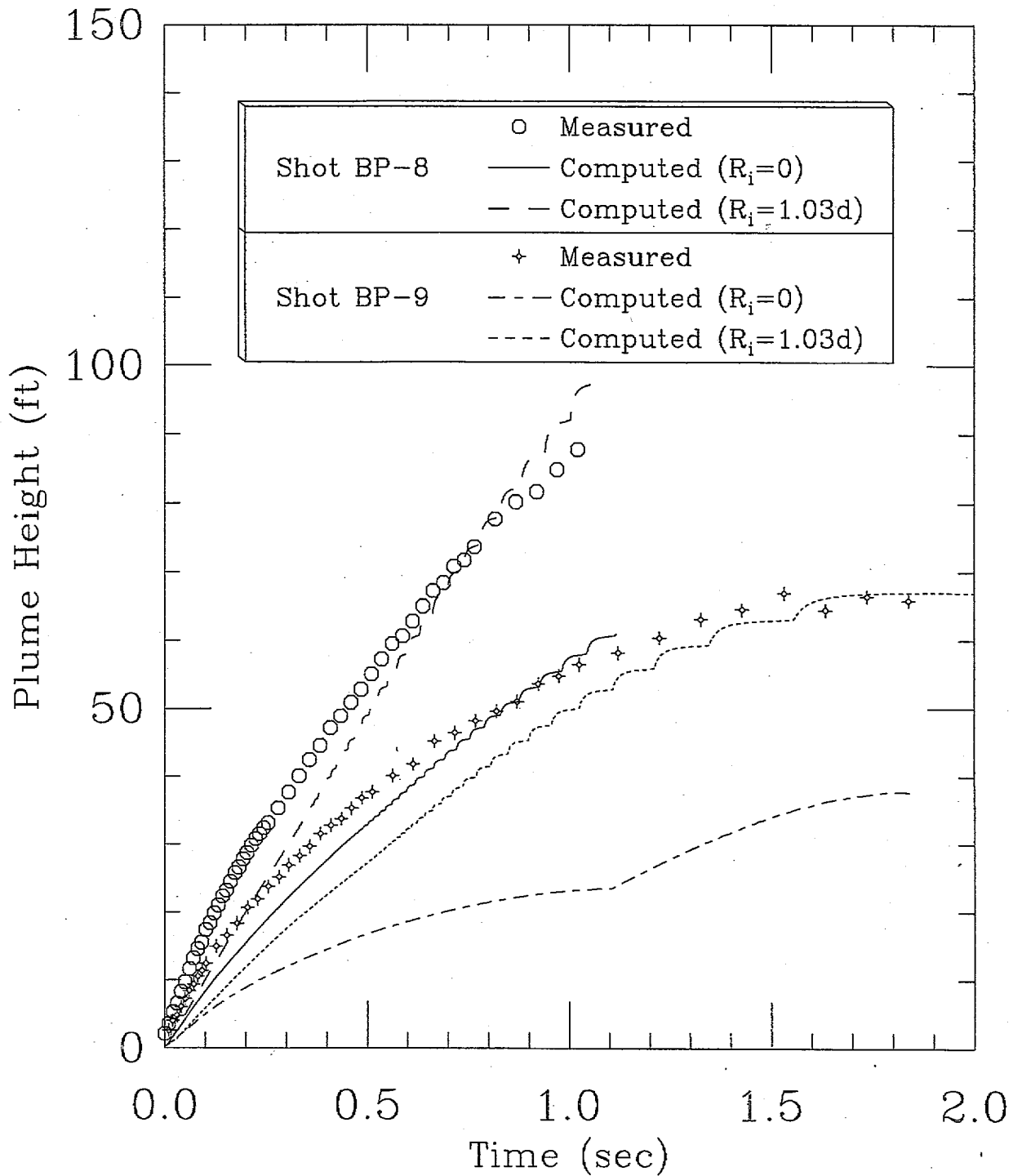


FIGURE 4-6. COMPUTED AND MEASURED PLUME HEIGHTS FOR BRIAR POINT SHOTS BP-8 AND BP-9

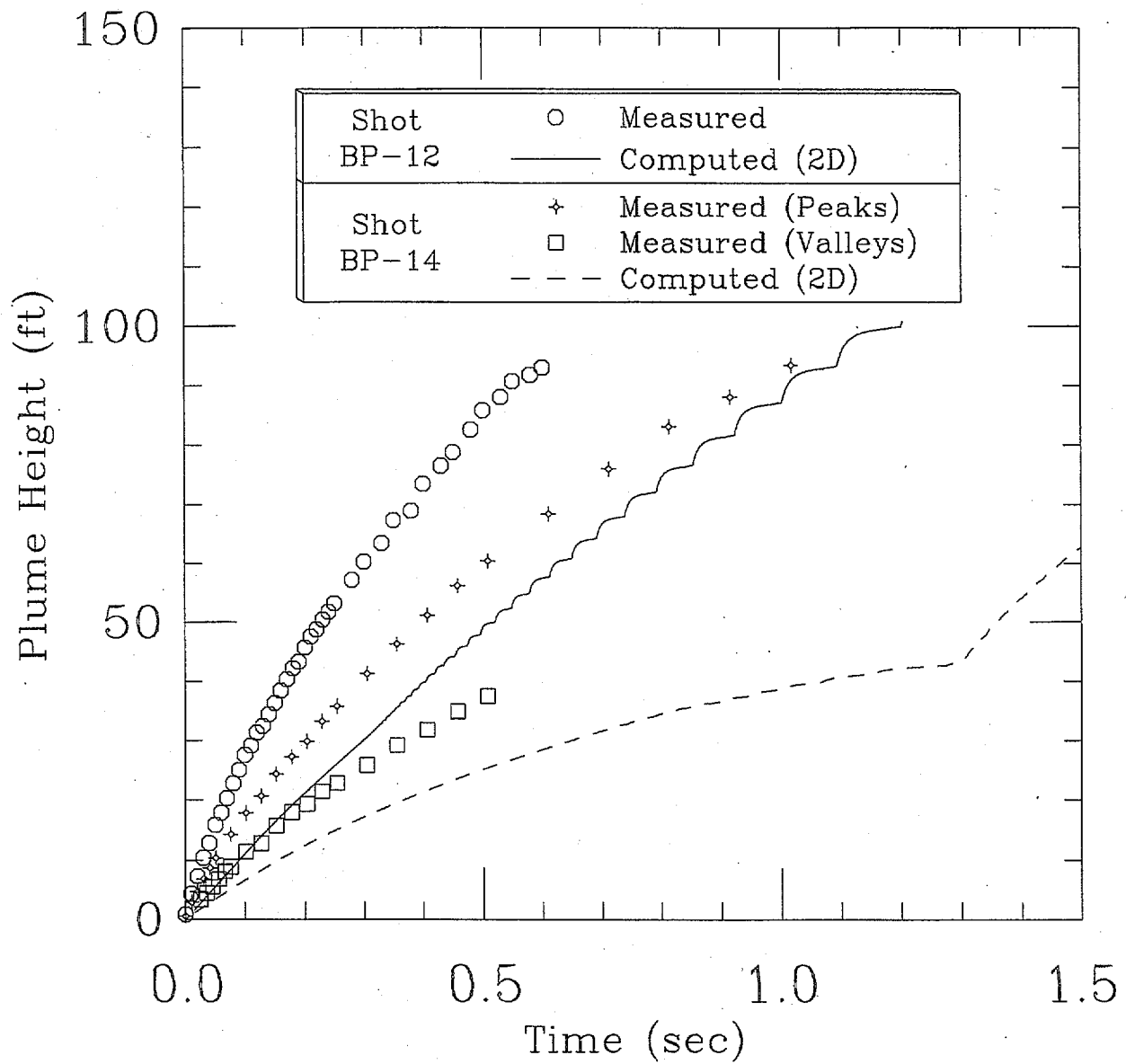


FIGURE 4-7. COMPUTED AND MEASURED PLUME HEIGHTS FOR BRIAR POINT SHOTS BP-12 AND BP-14

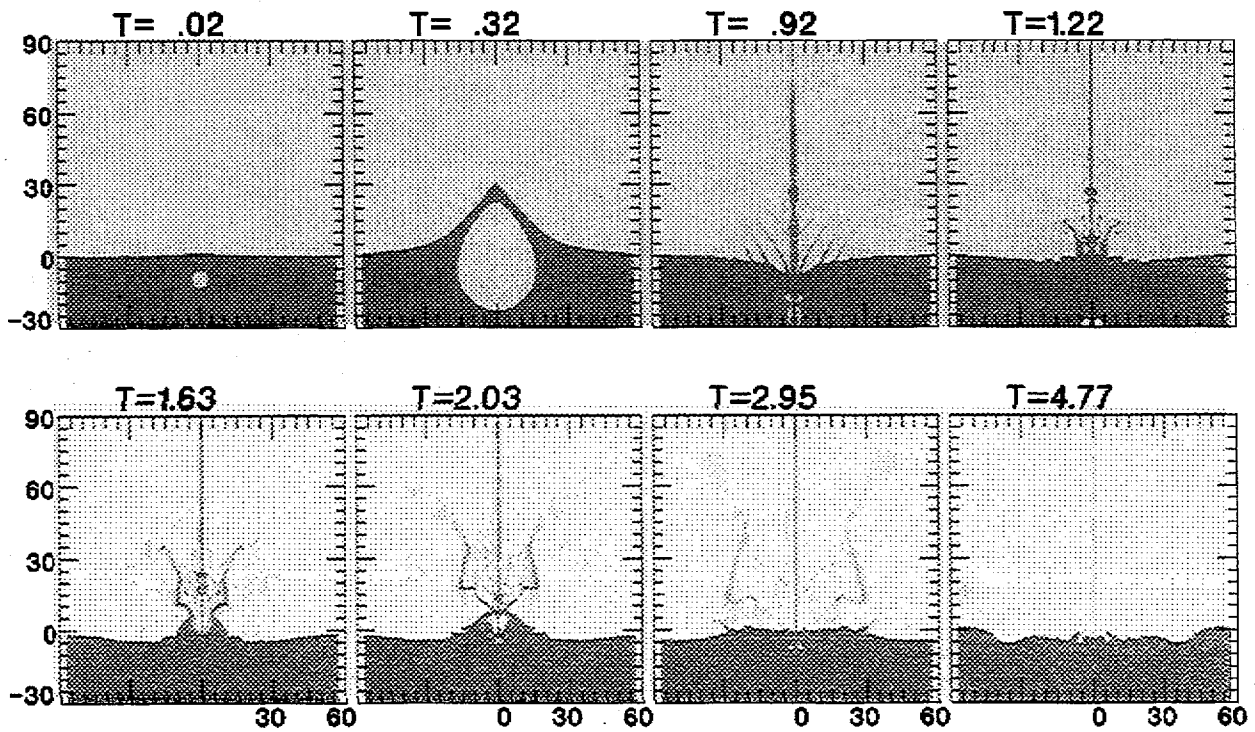
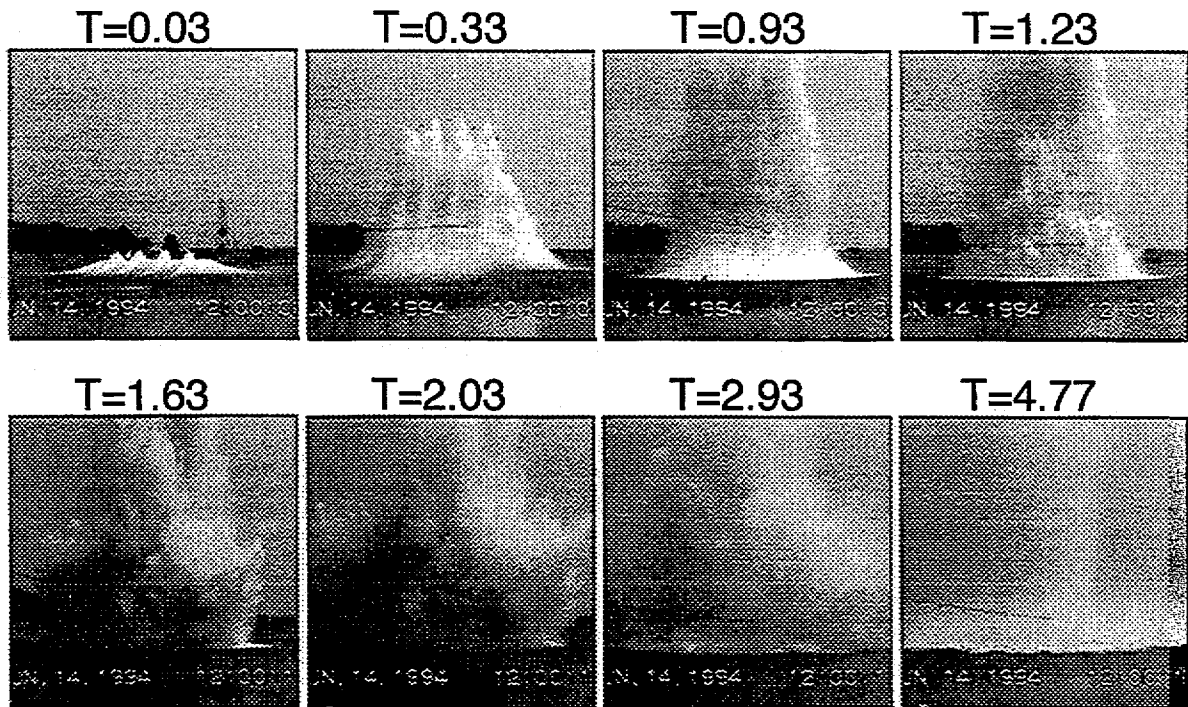


FIGURE 4-8. PHOTOGRAPHS AND COMPUTATIONS OF SHOT BP-12

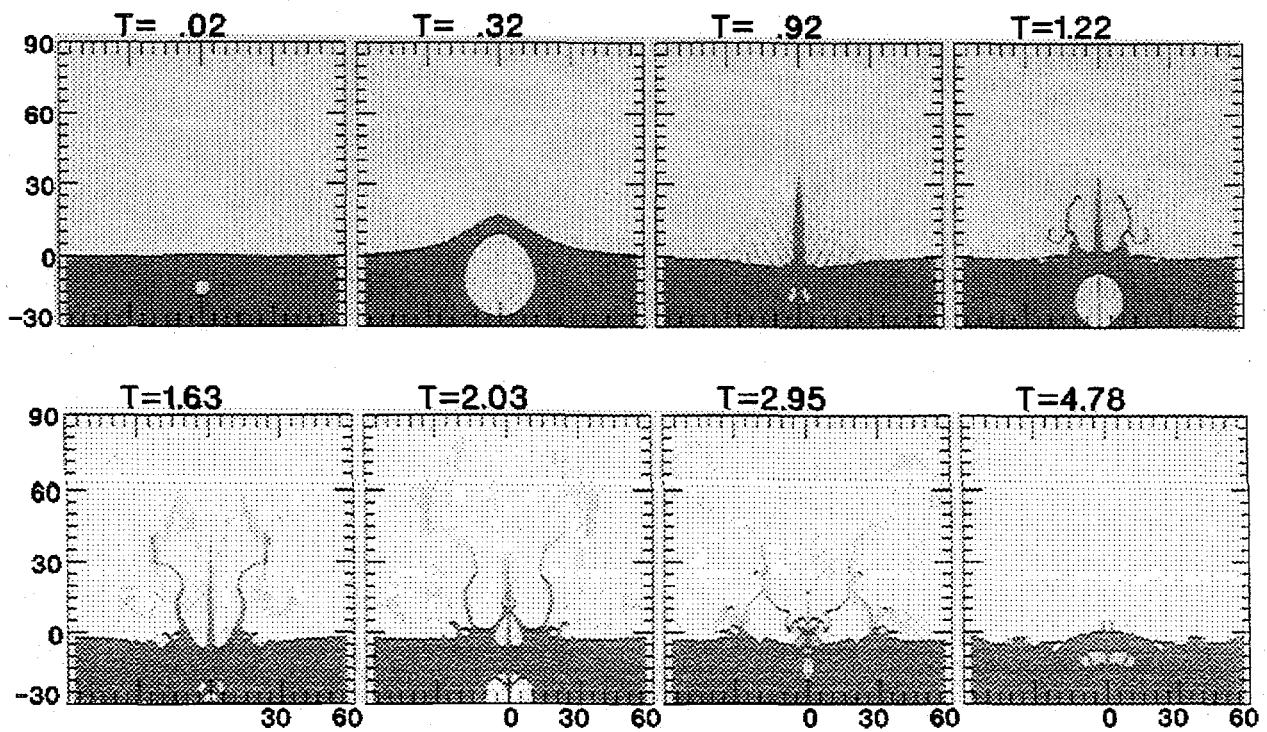
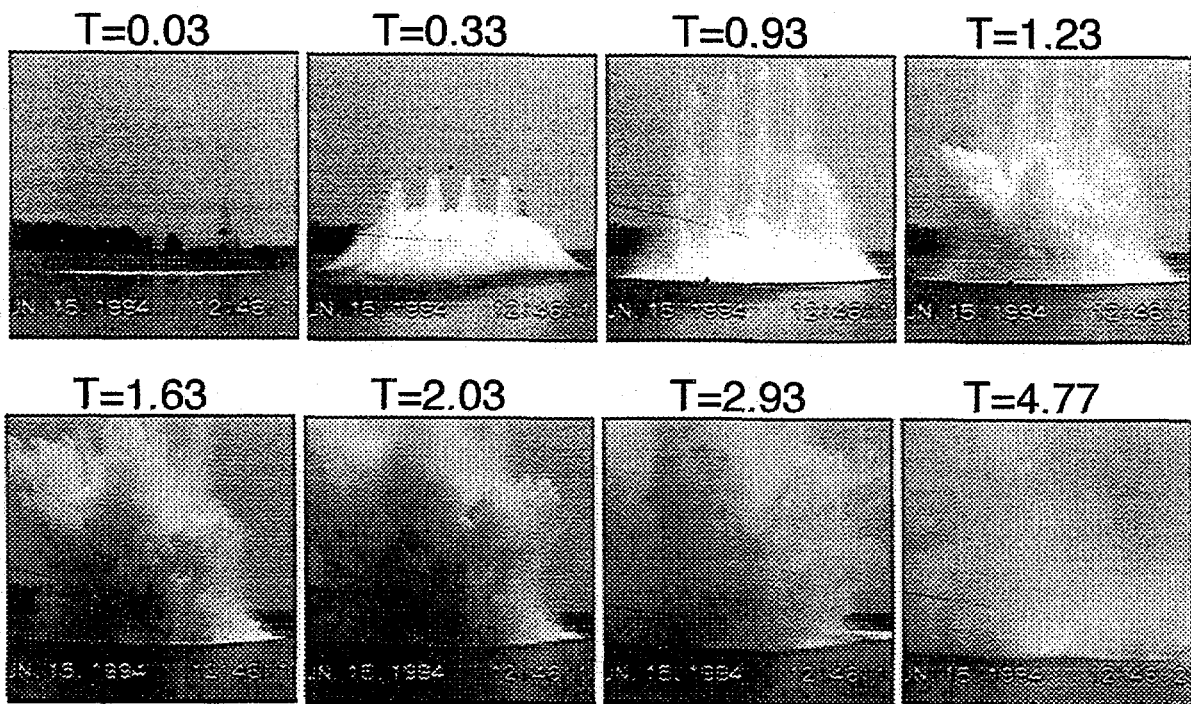


FIGURE 4-9. PHOTOGRAPHS AND COMPUTATIONS OF SHOT BP-14

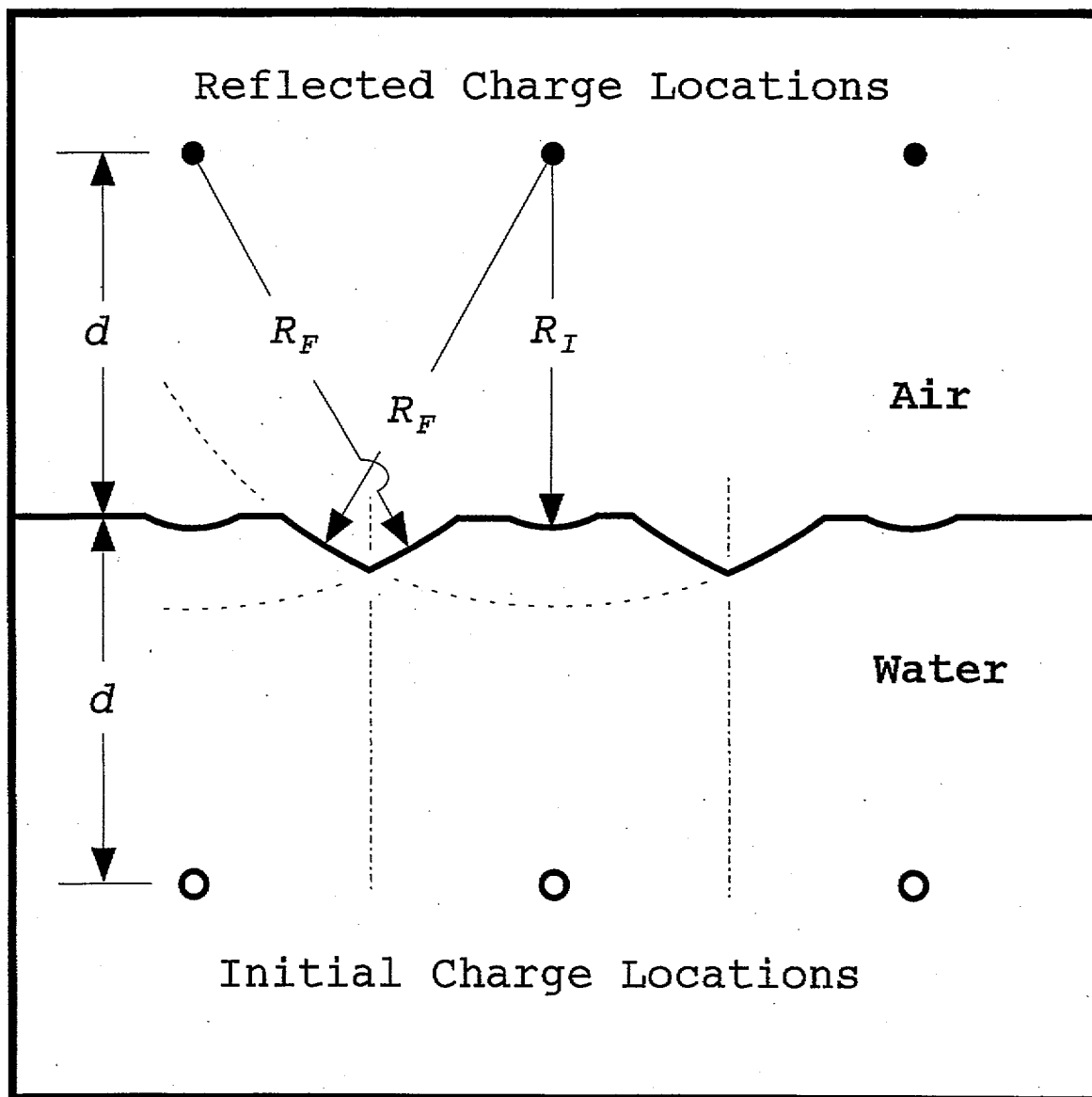


FIGURE 4-10. EMPIRICAL MODEL OF SURFACE SHOCK EFFECTS
FOR MULTIPLE CHARGE CONFIGURATIONS

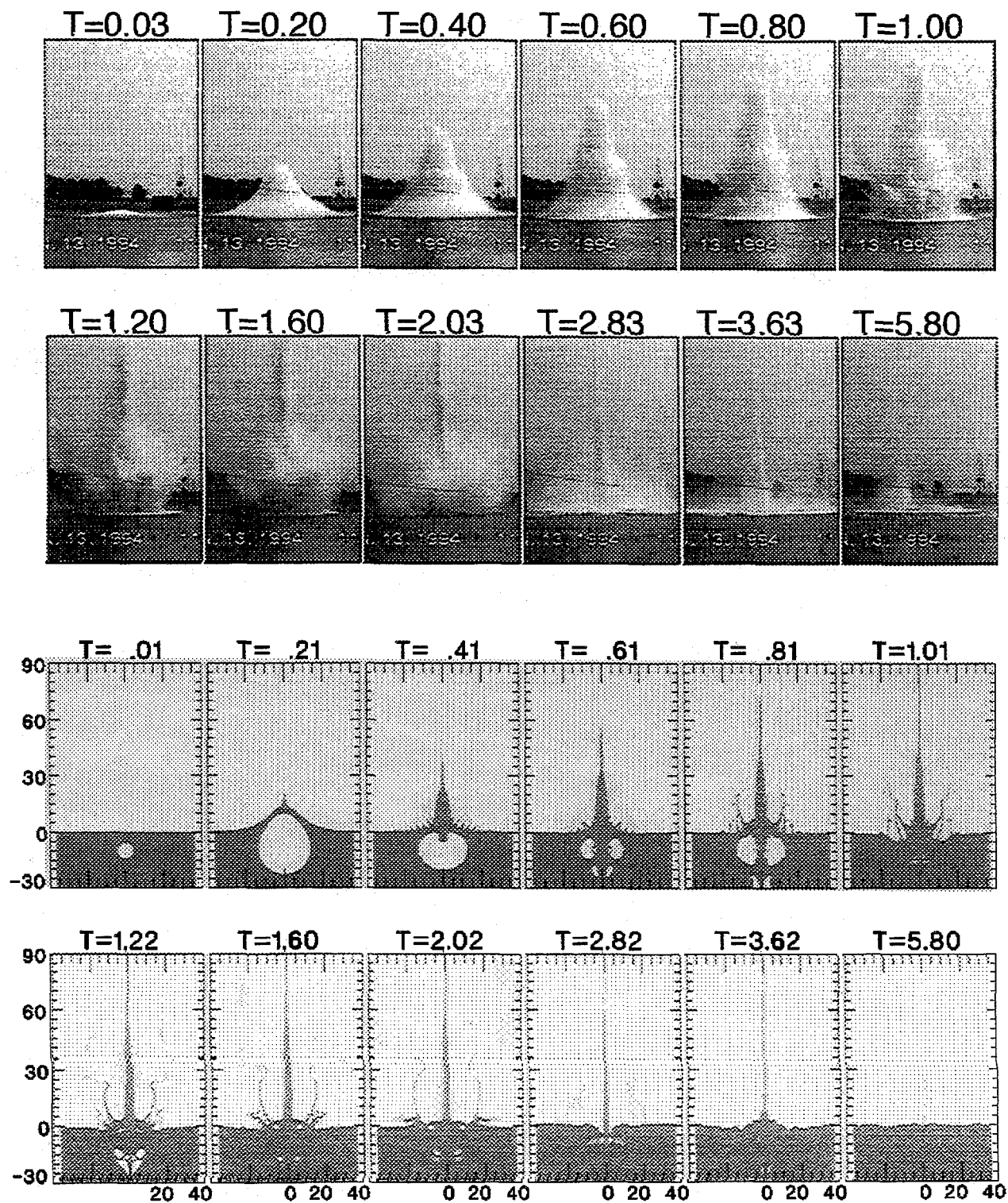


FIGURE 4-11. PHOTOGRAPHS AND COMPUTATIONS OF SHOT BP-8

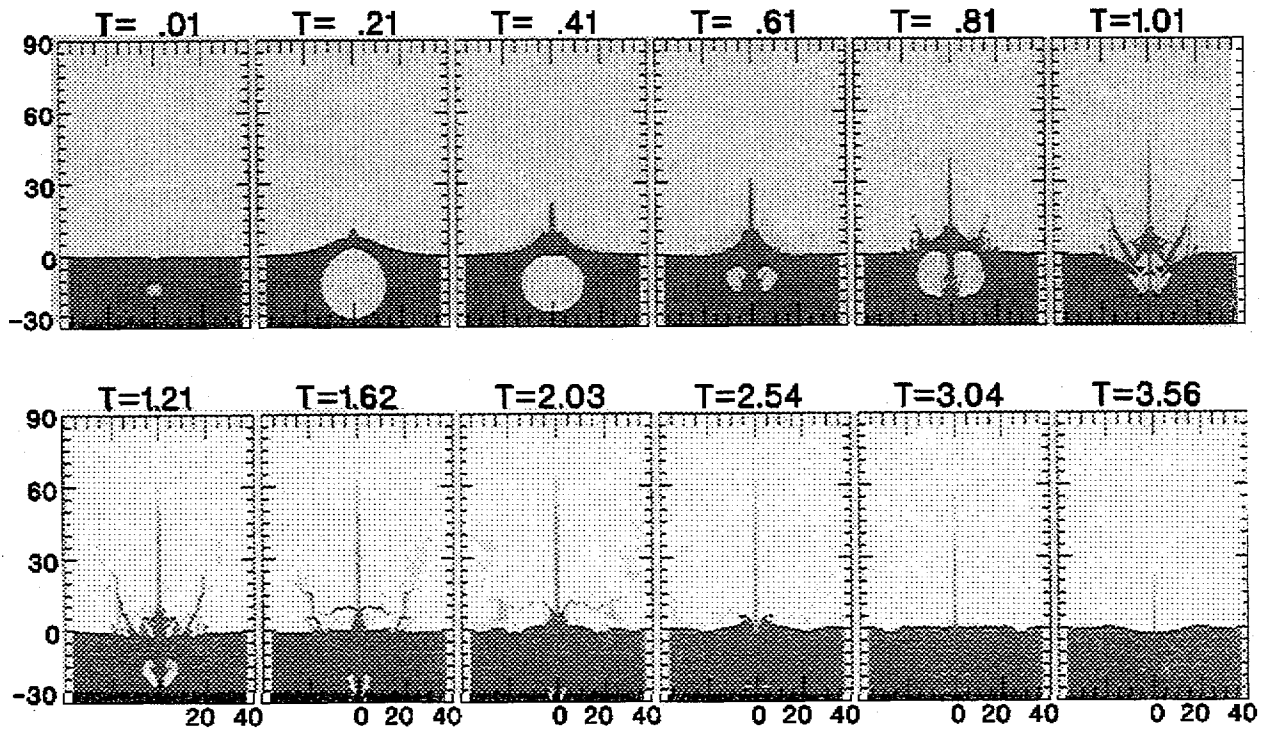
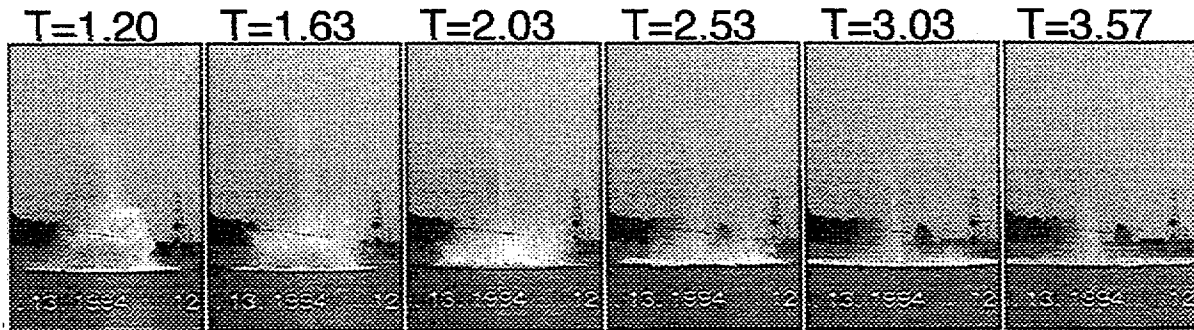
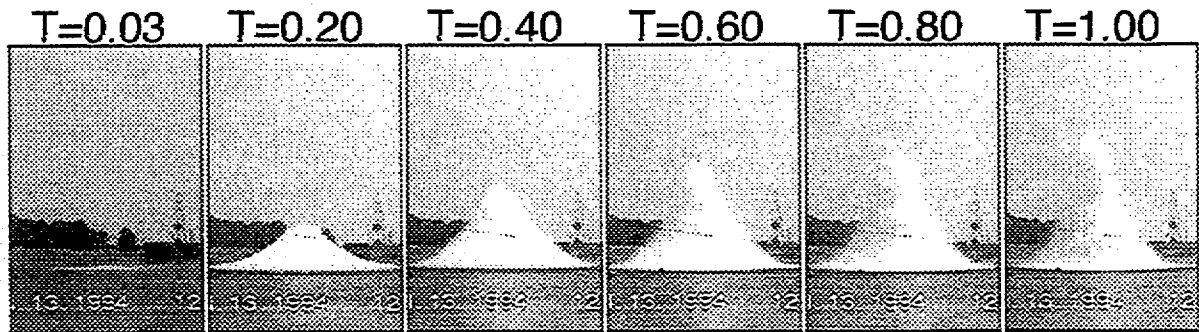


FIGURE 4-12. PHOTOGRAPHS AND COMPUTATIONS OF SHOT BP-9

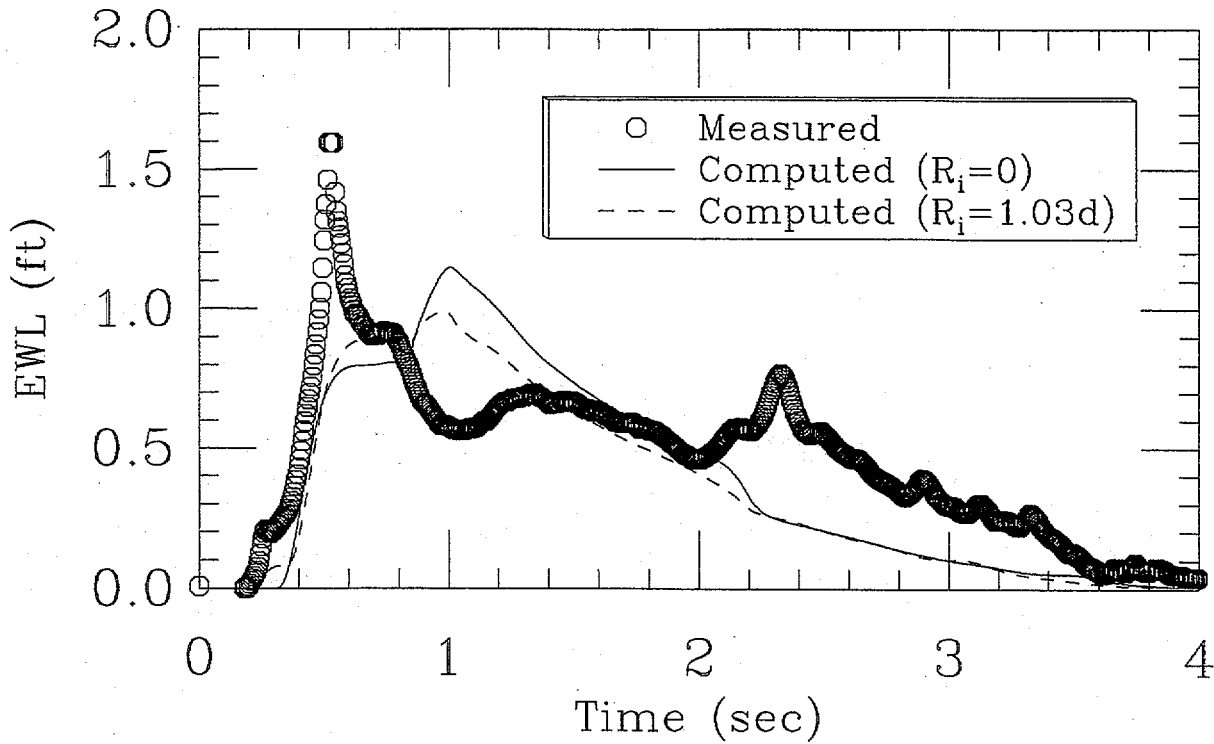


FIGURE 4-13. MEASURED AND COMPUTED MICROWAVE DATA FOR SHOT ARV-1

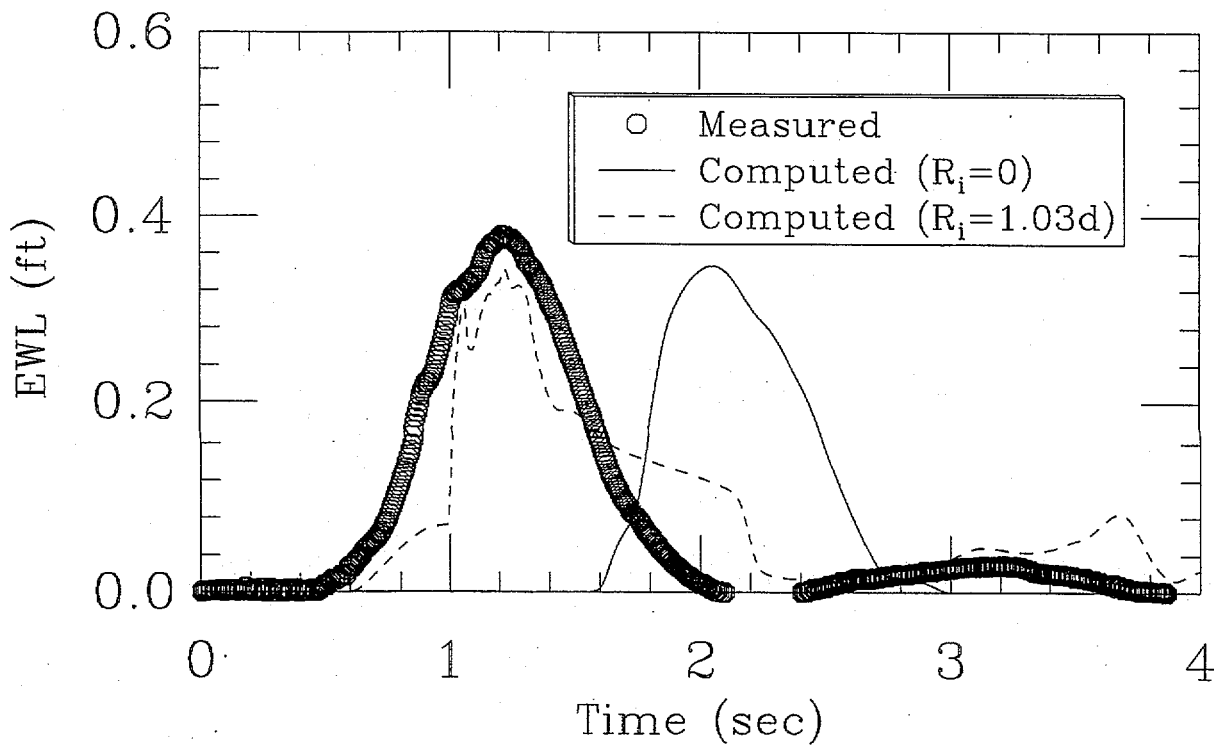


FIGURE 4-14. MEASURED AND COMPUTED MICROWAVE DATA FOR SHOT ARV-2

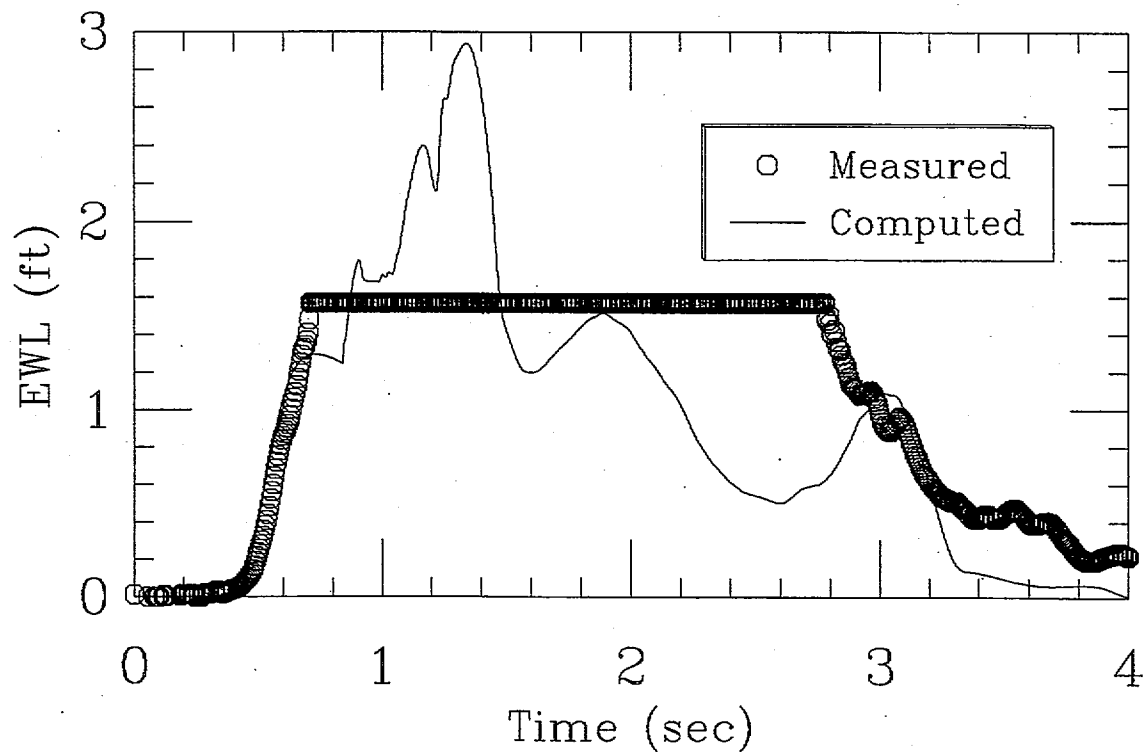


FIGURE 4-15. MEASURED AND COMPUTED MICROWAVE DATA FOR MULTIPLE CHARGE SHOT ARV-3

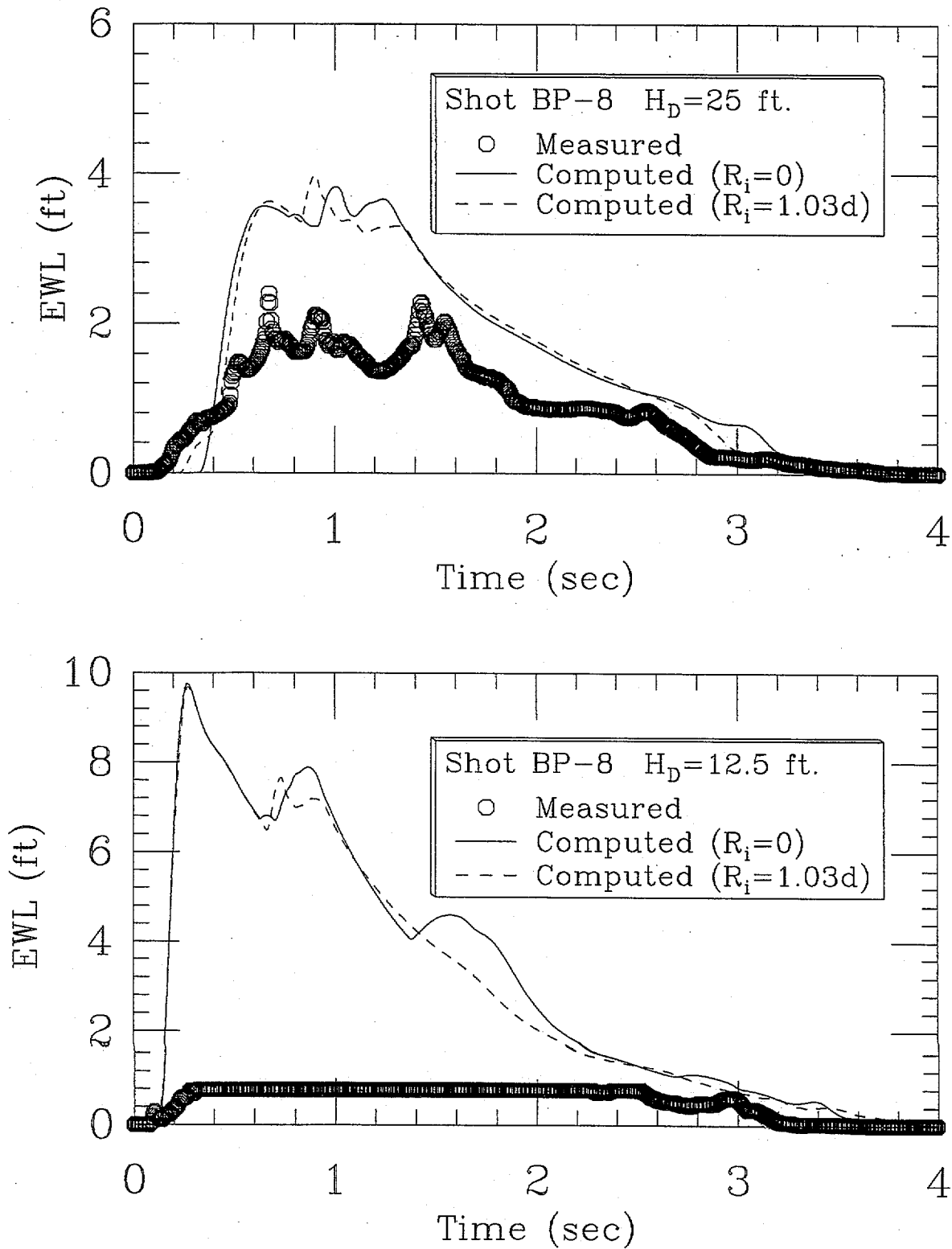


FIGURE 4-16. COMPUTED AND MEASURED MICROWAVE DATA FOR SHOT BP-8 AT HEIGHTS OF 25 AND 12.5 FT

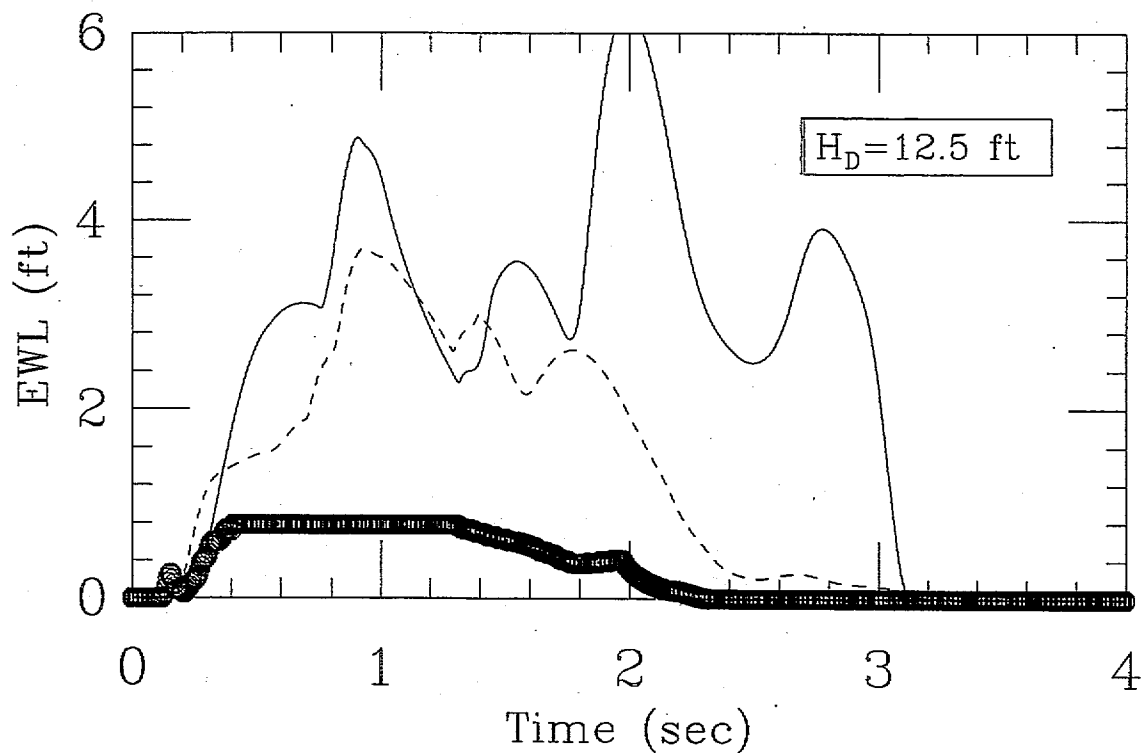
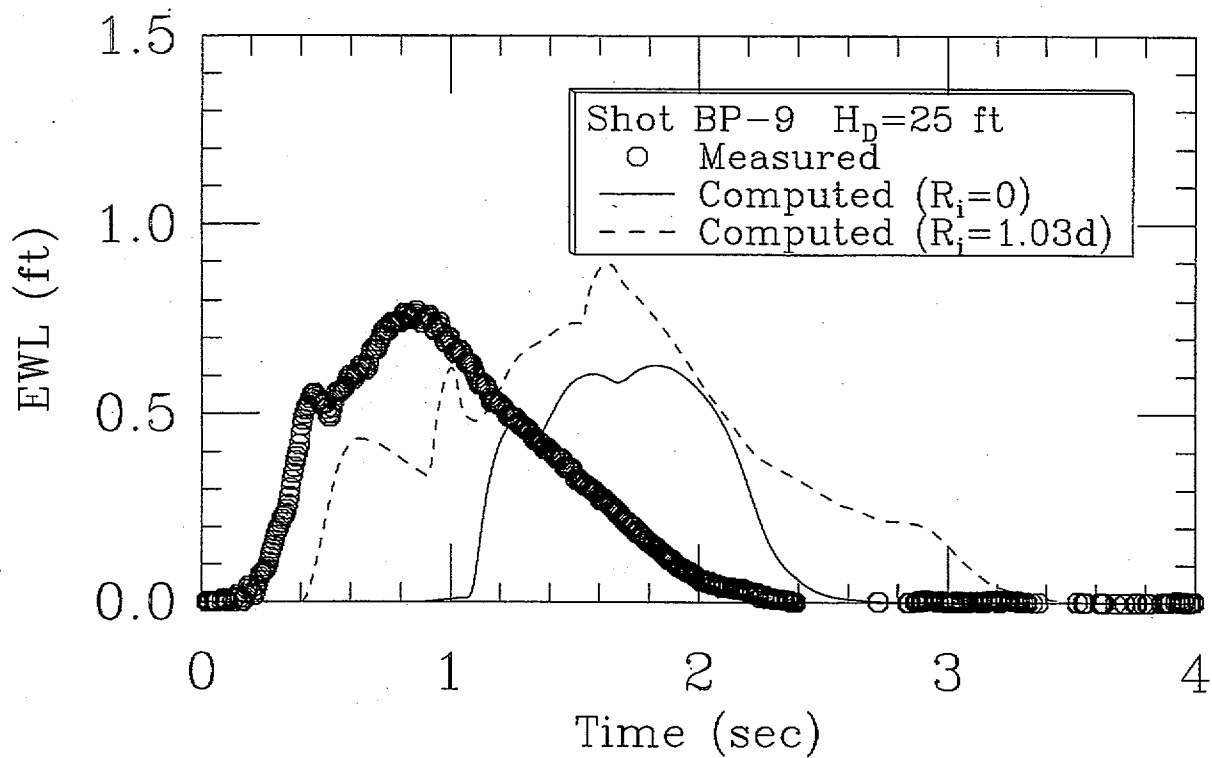


FIGURE 4-17. COMPUTED AND MEASURED MICROWAVE DATA FOR SHOT BP-9 AT HEIGHTS OF 25 AND 12.5 FT

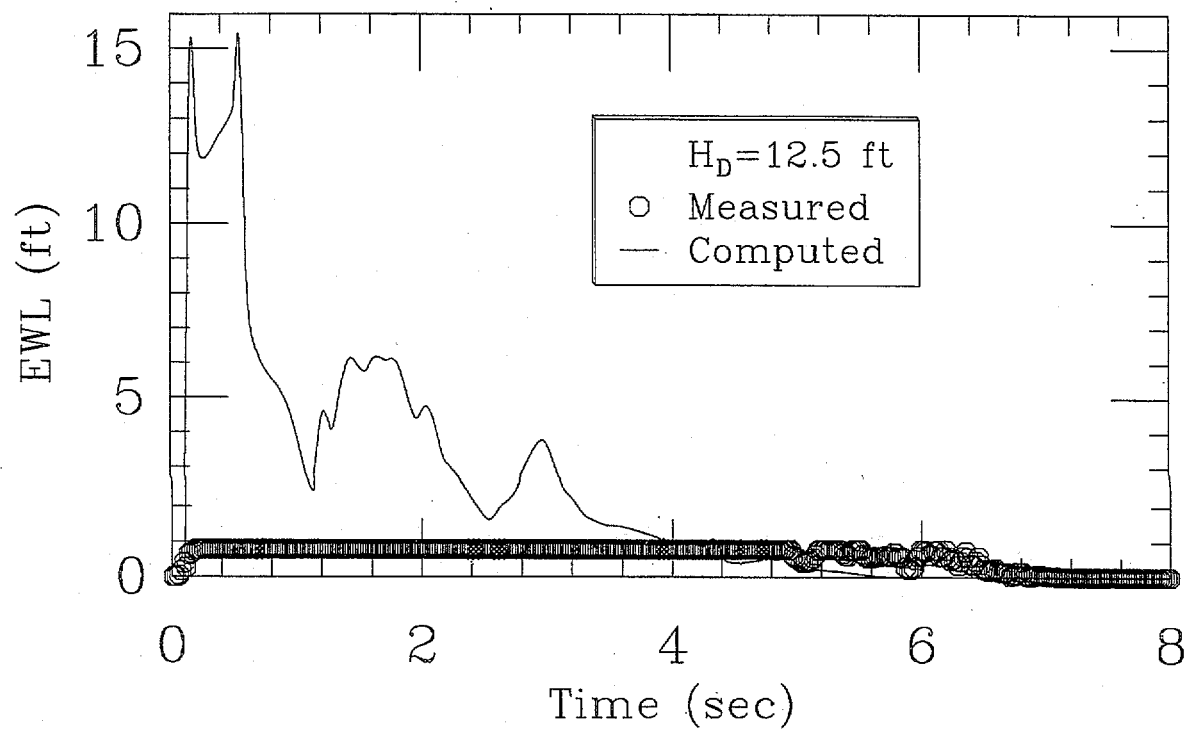
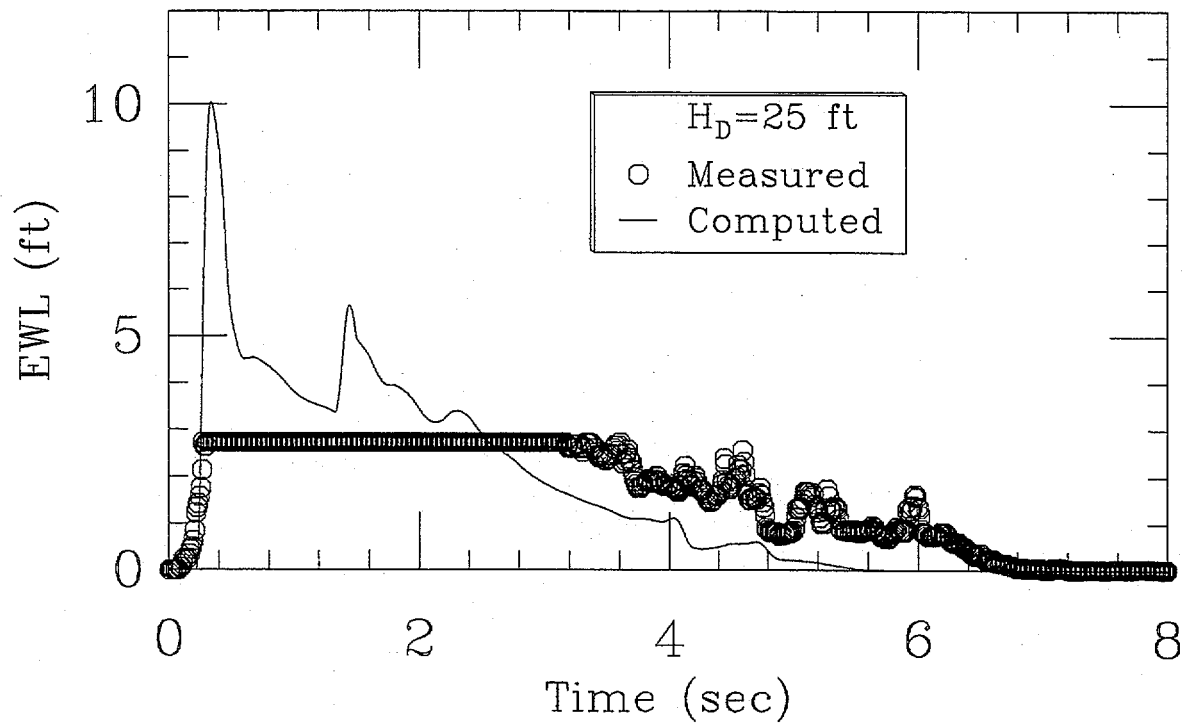


FIGURE 4-18. COMPUTED AND MEASURED MICROWAVE DATA FOR MULTIPLE CHARGE SHOT BP-12 AT HEIGHTS OF 25 AND 12.5 FT

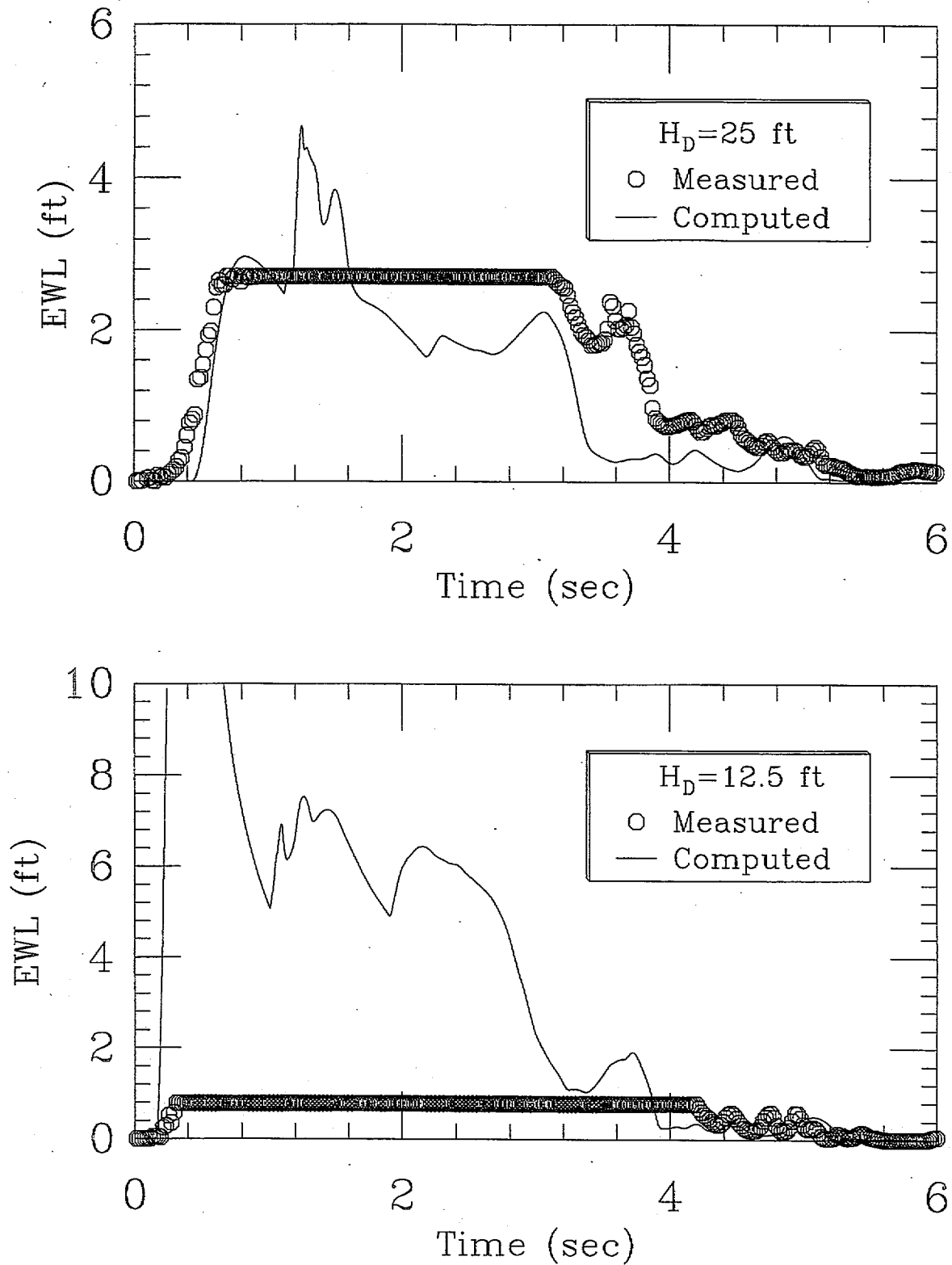


FIGURE 4-19. COMPUTED AND MEASURED MICROWAVE DATA FOR MULTIPLE CHARGE SHOT BP-14 AT HEIGHTS OF 25 AND 12.5 FT

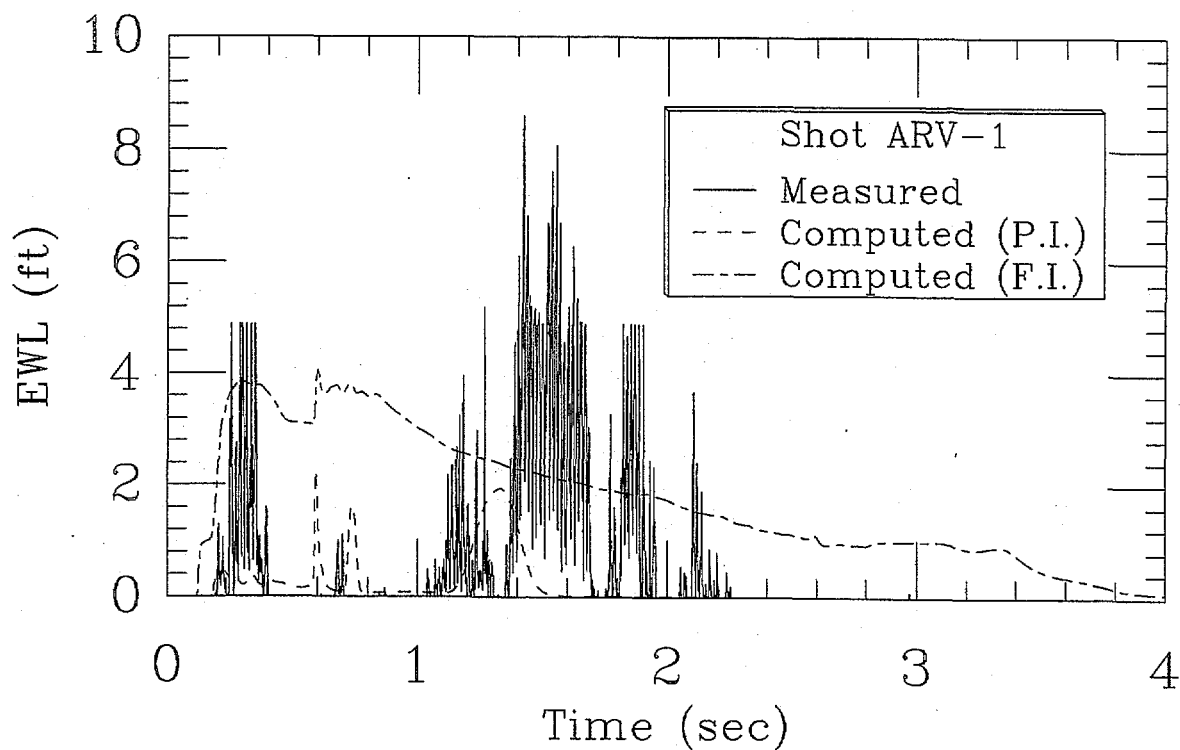


FIGURE 4-20. INTEGRATED PROBE DATA FOR SHOT ARV-1

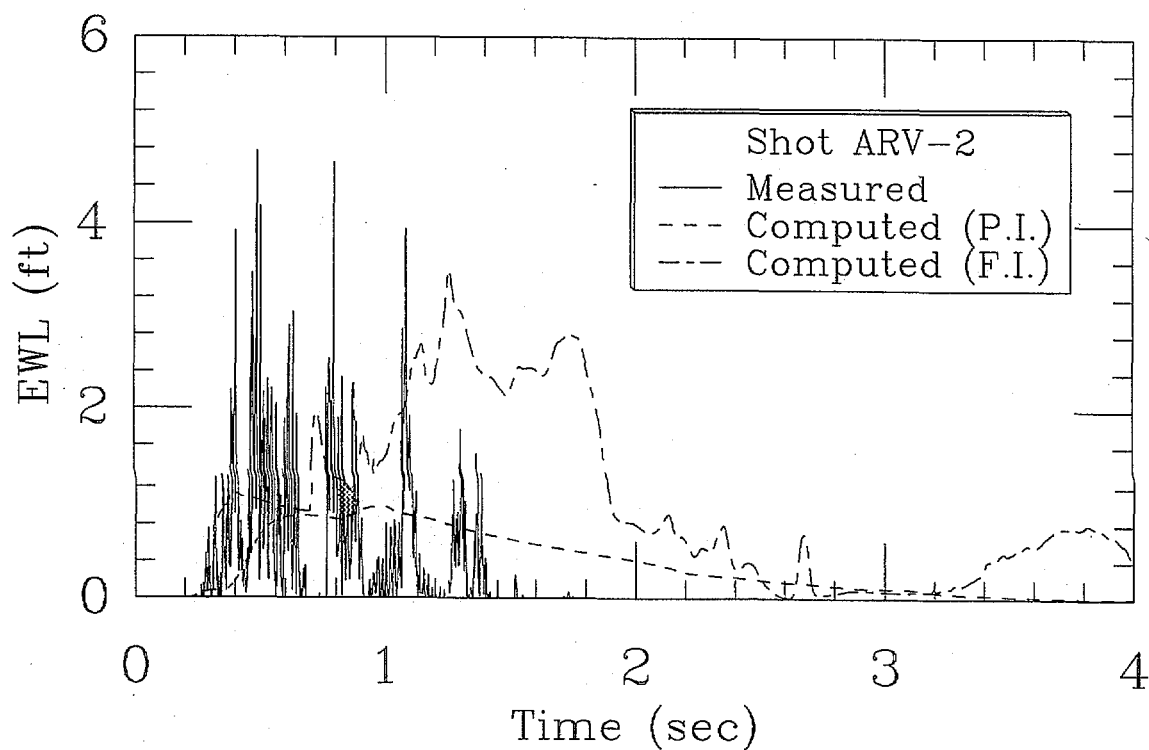


FIGURE 4-21. INTEGRATED PROBE DATA FOR SHOT ARV-2

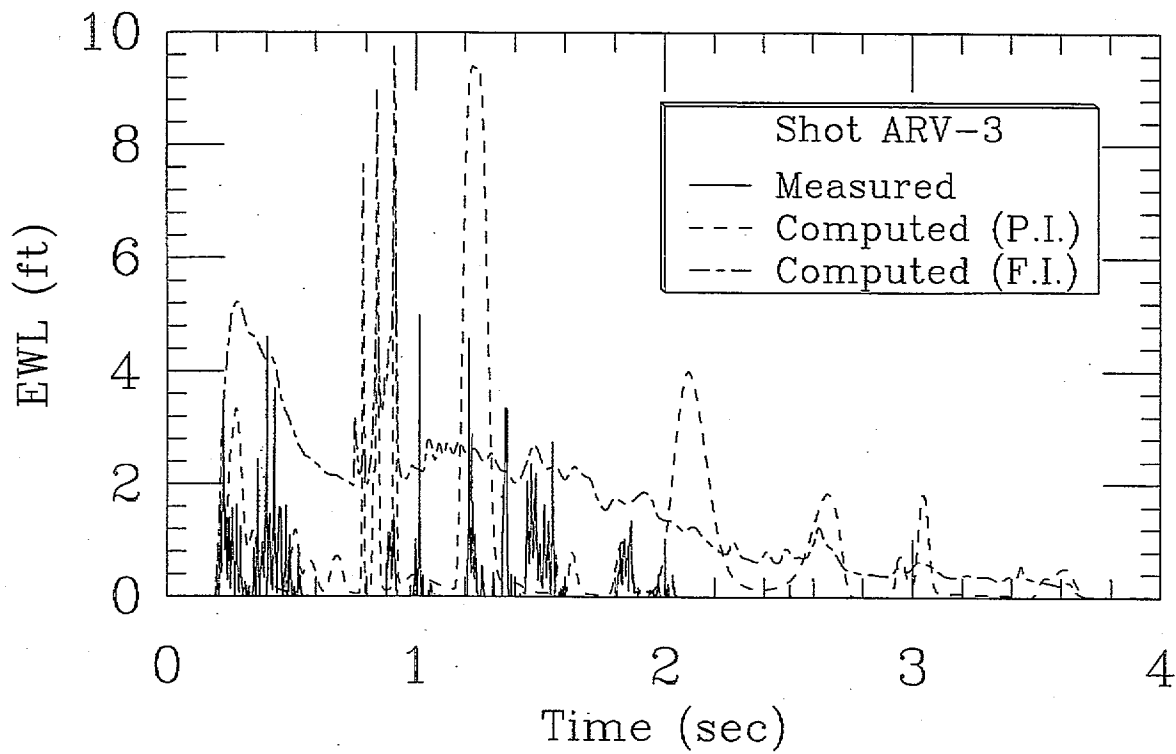


FIGURE 4-22. INTEGRATED PROBE DATA FOR SHOT ARV-3

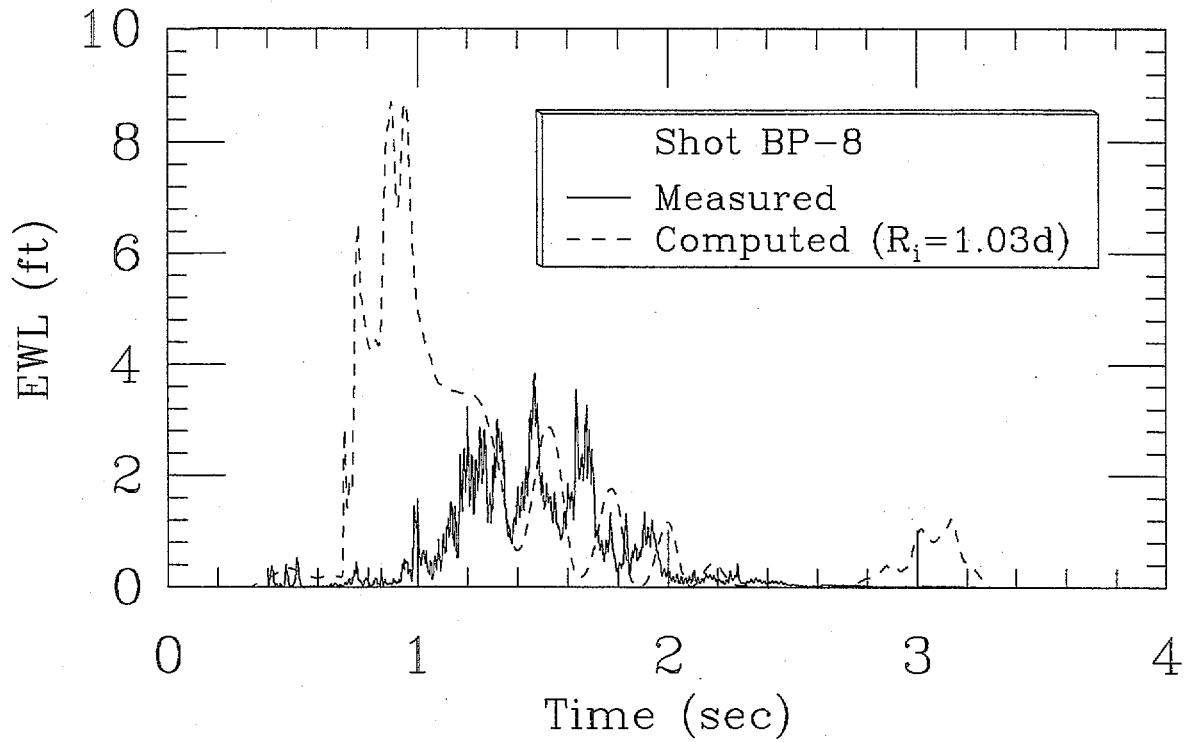


FIGURE 4-23. INTEGRATED PROBE DATA FOR SHOT BP-8

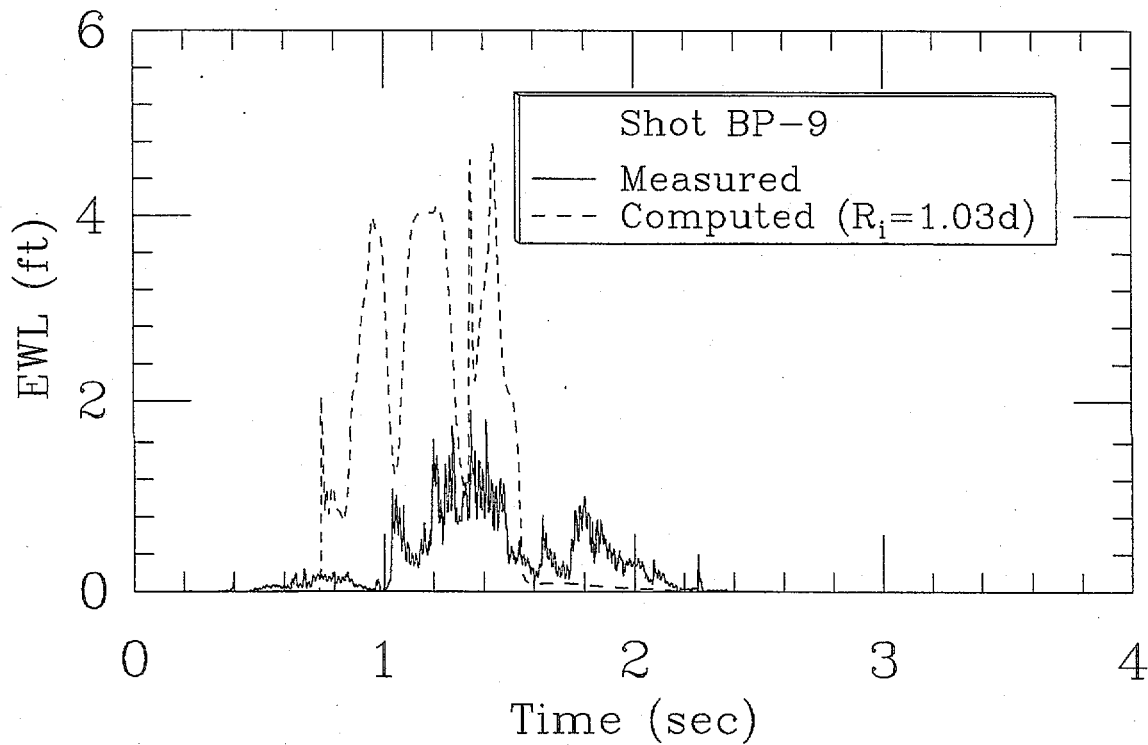


FIGURE 4-24. INTEGRATED PROBE DATA FOR SHOT BP-9

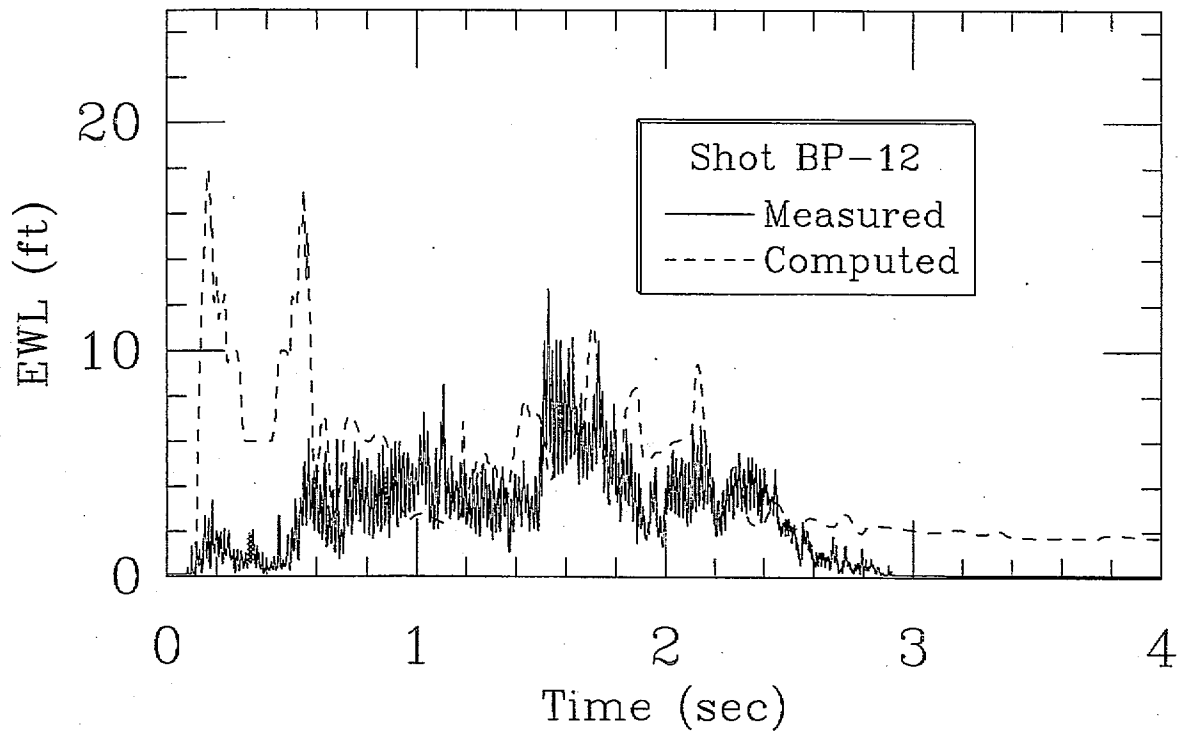


FIGURE 4-25. INTEGRATED PROBE DATA FOR SHOT BP-12

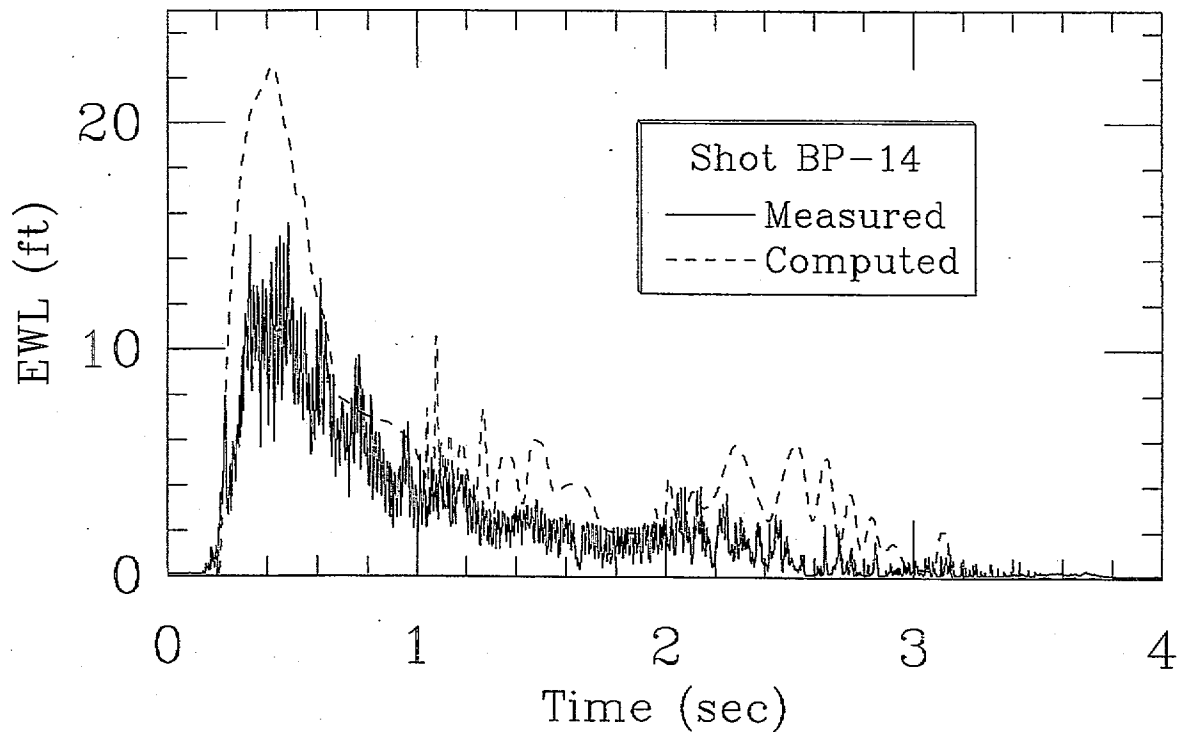


FIGURE 4-26. INTEGRATED PROBE DATA FOR SHOT BP-14

CHAPTER 5

CONCLUSIONS AND SUMMARY

The primary purpose of this report was to validate the computational code *BUB2D* for predictions of shallow depth explosion plumes. At the beginning of this study it was not possible to reliably predict long term explosion plume behavior. This was primarily because of insufficiencies in the physical modeling. Experimental observations were used to derive empirical relations, which greatly improved the computational predictions. These modifications to *BUB2D* are detailed below.

Initial Bubble Conditions

Since the chemistry of the explosion is not modeled, empirical laws are used together with the theory for a spherical bubble in an infinite incompressible liquid, to determine initial conditions for the *BUB2D* model. Unfortunately all of the empirical values for various charge types listed in the literature were based on approximations to the spherical bubble incompressible theory. These approximations are valid only at moderate depths. New empirical values are derived for the charge types studied here, without the use of any approximations to the spherical bubble theory. Furthermore, these values were based on experimental observations at a variety of charge depths. Since these values are substantially different than the values which have been accepted over the past 40 yr, a fairly detailed justification is provided in Chapter 3.

Bubble Venting

Venting is modeled only crudely by *BUB2D*, by instantaneously changing the pressure in the vented bubble region to the ambient atmospheric pressure. It was found through numerical experiments that bubbles would vent prematurely using the same cutoff value in the code which has been successful for deeper cases. Using a larger cutoff for liquid cells near the water-air interface only, premature venting was suppressed, while preserving the accuracy of predicting the underwater bubble dynamics.

Shock Effects

Since the *BUB2D* employs an incompressible liquid model, shock effects cannot be predicted. The dominant shock effect for shallow charges is the spallation of water due to the shock reflection off the free surface. This effect has been modeled empirically by initializing the free surface with an indentation. This indentation has been shown to greatly improve predictions of the plume height, particularly at early times. This indentation is characterized by a single constant which provided good plume height agreement for all single charge cases considered.

The phenomenon of shallow depth explosion plumes is extremely complicated. The bubble can undergo several cycles or periods before it vents. During each cycle hydrodynamic instabilities can be expected at both the bubble-water and air-water interfaces. Rayleigh Taylor instabilities occur whenever a denser material (water) is accelerated into a less dense material (bubble gas, or air). Such instabilities occur near the bubble interface when the bubble is near its minimum volume (higher than ambient pressure) and at the air-water interface as the bubble begins its contraction. These instabilities appear in experiments as a loss of axial symmetry (fingering of the secondary plumes) and make pointwise predictions impossible. Nevertheless, in many cases we were able to attain reasonable agreement with the experiments. A summary of comparisons of the computations to the measurements are listed below.

Plume Heights

Using an indented free surface as described above, excellent agreement was obtained between the computations and measured plume heights for the single charge cases. However, since we only used a two-dimensional model without an indented surface the computations underestimated the measured plume heights for the multiple shot cases.

Secondary Plumes

The computed secondary plumes ejected during the second bubble pulse are in good qualitative agreement with the observations. For many computational models this is a difficult feature to compute since it occurs well after the first bubble collapse. In addition to the relatively long time it takes to develop, the phenomenon is further complicated by the fact that the bubble may form one or more toroidal regions after this collapse. Neither of these factors is an issue for the model in *BUB2D* and no special modifications to the code were made concerning the prediction of these plumes.

Microwave Data

Considering the complexity of the problem and the lack of an independent validation for the measurements, comparisons between the computations and experiments were reasonably good. Despite the fact that the multiple shot plume heights were underpredicted, there was remarkable agreement between the computed and measured rise in *EWL* values at early times. This suggests that the visible peaks of the plumes contain a relatively insignificant mass of water.

Density Probe Data

The only significant match between the measured and computed probe data occurred with the multiple shot cases BP-12 and BP-14. The probes must be sufficiently close together and the data must be integrated to provide any meaningful comparisons.

One issue not addressed in detail in this report is the three-dimensional effects that occur when using multiple discrete charges. Several experiments were conducted at Dynamic Testing Incorporated in Rustberg, Virginia in June, 1995 to investigate these effects. This data will be used together with *BUB3D* and the empirical model presented in Figure 4-10 in a forthcoming publication.

The algorithm used for both codes *BUB2D* and *BUB3D* are continually being improved. One such improvement is to ensure the strict conservation of mass. A version of the codes that do not add mass when "numerical cavitation" occurs (see Chapter 2) is currently being tested. Since the mass is the most important variable for these shallow plume predictions, this modification can be expected to improve our predictive capability.

Based on the validations presented in this study, it is now possible to conduct optimality studies with some degree of confidence. For example, it may be possible to optimize the duration that the *EWL* is above some prescribed threshold value. Such studies will be the topic of future work.

REFERENCES

1. Cole, R. H., *Underwater Explosions*, Princeton University Press, Princeton, NJ, 1948, pp. 270-353, 392-402.
2. Young, G. A., *Plume and Ejecta Hazards from Underwater Explosions*, NOLTR 73-111, Dec 1973, Naval Surface Warfare Center, Silver Spring, MD.
3. Young, G. A., *Dispersions of Chemical Products of Underwater Explosions*, NSWC TR 82-404, Dec 1984, Naval Surface Warfare Center, Silver Spring, MD.
4. Blake, J. R., and Gibson, D. C., "Growth and Collapse of a Vapour Cavity near a Free Surface," *Journal of Fluid Mechanics*, Vol 111, 1981, pp. 123-140.
5. Kedrinskii, V. K., "Surface Effects from an Underwater Explosion (Review)," *Journal of Applied Mechanics and Technical Physics*, Vol. 19, No. 4, 1979, pp. 474-491.
6. Snay, H. G., "Hydrodynamics of Underwater Explosions," in *Symposium of Naval Hydrodynamics*, (Proceedings of the Symposium on Naval Hydrodynamics held in Washington, D.C., 24-28 September, 1956) Sherman, F. S., Ed., Publication 515, National Academy of Sciences - National Research Council, Washington, D. C., 1957, pp. 325-352.
7. Kolsky, H., Lewis, J. P., Sampson, M. T., Shearman, A. C., and Snow, C. I., "Splashes from Underwater Explosions," *Proceedings of the Royal Society, Series A*, Vol. 196, No. 1046, 1949, pp. 379-402.
8. Chahine, G. L., "Interaction Between an Oscillating Bubble and a Free Surface," *Journal of Fluids Engineering*, Vol. 99, 1977, pp. 709-716.
9. Rogers, J. C. W., Szymczak, W. G., Berger, A. E., and Solomon, J. M., "Numerical Solution of Hydrodynamic Free Boundary Problems," in *Free Boundary Problems, Proceedings of the Conference on Free Boundary Problems-Numerical Methods and Optimal Control, International Series of Numerical Mathematics*, Oberwolfach, Germany, 9-19 Jul 1989, Vol. 95., Hoffman, K.-H. and Sprekels, J., Eds., Birkhäuser Verlag Basel, 1990, pp. 241-266.
10. Szymczak, W. G., Rogers, J. C. W., Solomon, J. M., and Berger, A. E., "A Numerical Algorithm for Hydrodynamic Free Boundary Problems," *Journal of Computational Physics*, Vol. 106, No. 2, Jun 1993, pp. 319-336.
11. Szymczak, W. G., Solomon, J. M., Berger, A. E., and Rogers, J. C. W., "A Numerical Method Based on a Generalized Formulation of Hydrodynamic Free Surface Problems," paper no. AIAA-91-1541-CP, in *Proceedings of the AIAA 10th Computational Fluid Dynamics Conference*, Honolulu, Hawaii, 24-27 Jun 1991, pp. 155-165.
12. Szymczak, W. G., Solomon, J. M., and Berger, A. E., *BUB3D - Description of Mathematical Model, Algorithms, and User's Guide*, NSWCDD/TR-95/42, in preparation.

13. Rogers, J. C. W., "Stability, Energy Conservation, and Turbulence for Water Waves," *Seminaires IRIA Analyse et Contrôle de Systèmes* 1978, pp. 162-180.
14. Szymczak, W. G., "Energy Losses in Non-Classical Free Surface Flows," in, *Bubble Dynamics and Interface Phenomena*, (Proceedings of an IUTAM Symposium held in Birmingham, U.K., 6-9 September 1993) Blake, J. R., Boulton-Stone, J. M., and Thomas, N. H., Eds., Kluwer Academic Publishers, Dordrecht, The Netherlands, 1994, pp. 413-420.
15. Szymczak, W. G., Solomon, J. M., Berger, A. E., and Rogers, J. C. W., "Numerical Simulations of Cavitation Inception," in, *Proceedings of the International Symposium on Cavitation*, Deauville, France, 2-5 May 1995, pp. 399-406.
16. Friedman, B., "Theory of Underwater Explosion Bubbles," *Communications in Pure and Applied Mathematics*, Vol. 3, 1950, pp. 177-199.
17. Burden, R. L., and Faires, J. D., *Numerical Analysis*, Fourth Edition, PWS-KENT Publishing Company, Boston, MA, 1988, pp. 254-255.
18. Swift, E. Jr., Fye, P. M., Decius, J. C., and Price, R. S., *Photography of Underwater Explosions II High Speed Photographs of Bubble Phenomena*, NAVORD Report 95-46, Dec 1946.
19. Swift, E. Jr., and Decius, J. C., *Measurement of Bubble Pulse Phenomena, III Radius and Period Studies*, NAVORD Report 97-46, Sep 1947.
20. Arons, A. B., Slifko, J. P., and Carter, A., "Secondary Pressure Pulses Due to Gas Globe Oscillation on Underwater Explosions. I. Experimental Data," *The Journal of the Acoustical Society of America*, Vol. 20, No. 3, May 1948, pp. 271-276.
21. Arons, A. B., "Secondary Pressure Pulses Due to Gas Globe Oscillation on Underwater Explosions. II. Selection of Adiabatic Parameters in the Theory of Oscillation," *The Journal of the Acoustical Society of America*, Vol. 20, No. 3, May 1948, pp. 277-282.
22. Yennie, D. R. and Arons, A. B., *Secondary Pressure Pulses Due to Gas Globe Oscillation in Underwater Explosions, III. Calculation of Bubble Radius-Time Curve From Pressure-Time Record*, NAVORD Report 425, Oct 1949.
23. Price, R. S., *Studies of Explosions at Depths Greater than One Mile in the Ocean, V. Bubble Measurements*, NOLM 10947, Mar 1950.
24. Snay, H. G., and Christian, E. A., *Underwater Explosion Phenomena: The Parameters of a Non-Migrating Bubble Oscillating in an Incompressible Medium*, NAVORD Report 2437, Feb 1952.
25. Snay, H. G., Goertner, J. F., and Price, R. S., *Small Scale Experiments to Determine Migration of Explosion Gas Globes Towards Submarines*, NAVORD Report 2280, Jul 1952.
26. Jones, H. and Miller, A. R., "The Detonation of Solid Explosives: The Equilibrium Conditions in the Detonation Wave-Front and the Adiabatic Expansion of the Products of Detonation," *Proceedings of the Royal Society*, Vol A194, 1948, pp. 480-507.

27. Ornellas, D. L., "The Heat and Products of Detonation of Cyclotetramethylenetetranitramine, 2,4,6-Trinitrotoluene, Nitromethane, and Bis[2,2-dinitro-2-fluoroethyl]formal," *The Journal of Physical Chemistry*, Vol. 72, No. 7, Jul 1968, pp. 2390-2394.
28. Renner, R. H., and Short, J. M., *Chemical Products of Underwater Explosions*, NWSC/WOL TR 78-87, Feb 1980.
29. Snay, H. G., *Present Knowledge About the Change of the Bubble Parameters with Depth*, NOLTN-5596, Apr 1962.
30. Snay, H. G. *Model Tests and Scaling*, NOLTR 63-257, Dec 1964.
31. Holland, N. O., Caudle, K. F., Goertner, J. A., *Explosives--Effects and Properties (U)* NOLTR 65-218, Feb 1967 (CONFIDENTIAL).
32. Swisdak, M. J., Jr., Ed., *Explosion Effects and Properties: Part II - Explosion Effects in Water*, NSWC/WOL TR 76-116, Feb 1978.
33. Swisdak, M. J., private communication.
34. Blake, J. R., Taib, B. B., and Doherty, G., "Transient Cavities Near Boundaries: Part 2. Free Surface," *J. Fluid Mech.*, Vol. 181, 1987, pp. 197-212.
35. Connor, J. G., *Underwater Performance of PBXW-115 and PBXN-103*, (U) NSWC TR 89-202, Jul 1989, (CONFIDENTIAL).
36. Heathcote, T. B., Niffenegger, C. R., *Measurements of the Underwater Explosive Power of Small Charges of Composition C-4, PBX-9404, and PETN*, NOL TN 6967, Sep 1965.
37. Higdon, C. E., "Water Barrier Ship Self Defense Concept," *Naval Surface Warfare Center Dahlgren Division Technical Digest*, Sep 1994, pp. 140-153.
38. Lipton, L., D., *Probe for Measurement of Water Mass of Plumes Produced by Underwater Detonations* IHTR 1757, 17 Jul 1995, Naval Surface Warfare Center - Indian Head Division, Indian Head, MD.
39. Choe, J. Y., Boulais, K. A., Chun, S. T., and Irwin, K. A., *Microwave Probe for Mass Measurements of a Water Plume*, NSWCDD/TR-95/187, 30 Sep 1995, NSWCDD, Silver Spring, MD.
40. Lipton, L. D., *Water Barrier Concept for Ship Self-Defence: Field Tests*, IHTR 1758, 23 Dec 1994, Naval Surface Warfare Center - Indian Head Division, Indian Head, MD.
41. Connor, J. G., *Briar Point Water Barrier Photography*, IHTR 1815, 24 Jul 1995, Naval Surface Warfare Center - Indian Head Division, Indian Head, MD.
42. Stebnovskii, S. V., "Interaction of Shock Waves from the Successive Underwater Explosion of Spherical Charges," *Journal of Applied Mechanics and Technical Physics*, Vol. 19, No. 4, 1979, pp. 491-496.
43. Coleburn, N. L., and Roslund, L. A., "Interaction of Spherical Shock Waves in Water," in *Fifth International Symposium on Detonation*, Pasadena, California, 18-21 Aug 1970, pp. 581-588.

DISTRIBUTION

	<u>Copies</u>		<u>Copies</u>
DOD ACTIVITIES (CONUS):		ATTN TECHNICAL LIBRARY	1
		CODE 20M (H JEROSKI)	1
ATTN ONR 351 (D SIEGEL)	1	CODE 10 (M HYMAN)	1
ONR 311 (R LAU)	1	COMMANDING OFFICER	
ONR 333 (E ROOD)	1	COASTAL SYSTEMS STATION	
CHIEF OF NAVAL RESEARCH		DAHLGREN DIVISION	
800 NORTH QUINCY STREET		NAVAL SURFACE WARFARE CENTER	
ARLINGTON VA 22217		6703 W HIGHWAY 98	
		PANAMA CITY FL 32407-7001	
ATTN CODE PM7 (R KAVETSKY)	1		
CODE 40E (E JOHNSON)	1	DEFENSE TECHNICAL INFORMATION	
CODE 420 (R MCKEOWN)	1	CENTER	
CODE 4220 (W WALKER)	1	CAMERON STATION	
CODE 450 (L LIPTON)	1	ALEXANDRIA VA 22304-6145	12
CODE 460 (N HOLLAND)	1		
CODE 4630 (J GASPIN)	1	NON-DOD ACTIVITIES (CONUS)	
CODE 4620 (W MCDONALD)	1		
CODE 4630 (G HARRIS)	1	ATTN DR S ANTMAN	1
CODE 4610 (H MAIR)	1	UNIVERSITY OF MARYLAND	
CODE 590 (K GESSNER)	1	DEPARTMENT OF MATHEMATICS	
CODE 950T (M SWISDAK)	1	COLLEGE PARK MD 20742	
COMMANDER			
INDIAN HEAD DIVISION		ATTN DR R B KELLOGG	1
NAVAL SURFACE WARFARE CENTER		DR R H NOCHETTO	1
INDIAN HEAD MD 20640-5035		UNIVERSITY OF MARYLAND	
		INSTITUTE FOR PHYSICAL SCIENCE	
ATTN TECHNICAL LIBRARY	1	AND TECHNOLOGY	
CODE 67.1 (C MILLIGAN)	1	COLLEGE PARK MD 20742	
CODE 67.1 (S ZILLIACKUS)	1		
CODE 542 (J SLOMSKI)	1	ATTN H LUO	1
COMMANDER		SCIENCE APPLICATIONS	
CARDEROCK DIVISION		INTERNATIONAL INCORPORATED	
NAVAL SURFACE WARFARE CENTER		1710 GOODRIDGE DRIVE	
BETHESDA MD 20084-5000		MS2-3-1	
		MCLEAN VA 22102	

DISTRIBUTION (CONTINUED)

	<u>Copies</u>		<u>Copies</u>
ATTN G CHAHINE DYNAFLOW INC 7210 PINDELL SCHOOL ROAD FULTON MD 20759	1	ATTN TECHNICAL LIBRARY CENTER FOR NAVAL ANALYSES 4401 FORD AVE ALEXANDRIA VA 22302-0268	1
ATTN R LÖHNER INSTITUTE FOR COMPUTATIONAL SCIENCES AND INFORMATICS GEORGE MASON UNIVERSITY FAIRFAX VA 22030-4444	1	INTERNAL DISTRIBUTION: B (M LACEY)	1
		B053 (R STATON)	1
		B04 (G MOORE)	1
		B40	1
		B42 (K BOULAIS)	1
ATTN J T ODEN DIRECTOR TICAM THE UNIVERSITY OF TEXAS AT AUSTIN TAY 2.400 AUSTIN TX 78712	1	B42 (J CHOE)	1
		B42 (K IRWIN)	1
		B44 (T-F ZIEN)	1
		B44 (A BERGER)	1
		B44 (K-Y CHIEN)	1
		B44 (A WARDLAW)	1
		B44 (F PRIOLO)	1
		B44 (W SZYMCAK)	25
ATTN T HUGHES CHAIRMAN OF THE BOARD CENTRIC ENGINEERING SYSTEMS INC 3393 OCTAVIUS DRIVE SUITE 201 SANTA CLARA CA 95054-3004	1	E231	2
		E232	3
		F101 (T H MCCANTS JR.)	1
		G23 (C E HIGDON)	5
		K24 (S L DRINNON)	1
		N742 (GIDEP)	1
ATTN J SOLOMON ENIG ASSOCIATES INC 11120 NEW HAMPSHIRE AVE SUITE 500 SILVER SPRING MD 20904	5		
ATTN GIFT AND EXCHANGE DIV LIBRARY OF CONGRESS WASHINGTON DC 20540	4		

REPORT DOCUMENTATION PAGEForm Approved
OBM No. 0704-0188

Public reporting burden for this collection of information is estimated to average 1 hour per response, including the time for reviewing instructions, search existing data sources, gathering and maintaining the data needed, and completing and reviewing the collection of information. Send comments regarding this burden or any other aspect of this collection of information, including suggestions for reducing this burden, to Washington Headquarters Services, Directorate for Information Operations and Reports, 1215 Jefferson Davis Highway, Suite 1204, Arlington, VA 22202-4302, and to the Office of Management and Budget, Paperwork Reduction Project (0704-0188), Washington, DC 20503.

1. AGENCY USE ONLY (Leave blank)		2. REPORT DATE August 1996	3. REPORT TYPE AND DATES COVERED	
4. TITLE AND SUBTITLE Computations and Experiments of Shallow Depth Explosion Plumes			5. FUNDING NUMBERS	
6. AUTHOR(s) W. G. Szymczak				
7. PERFORMING ORGANIZATION NAME(S) AND ADDRESS(ES) Naval Surface Warfare Center Dahlgren Division (Code B44) 17320 Dahlgren Rd. Dahlgren, VA 22448-5100			8. PERFORMING ORGANIZATION REPORT NUMBER NSWCDD/TR-94/156	
9. SPONSORING/MONITORING AGENCY NAME(S) AND ADDRESS(ES)			10. SPONSORING/MONITORING AGENCY REPORT NUMBER	
11. SUPPLEMENTARY NOTES				
12a. DISTRIBUTION/AVAILABILITY STATEMENT Approved for public release; distribution is unlimited.			12b. DISTRIBUTION CODE	
13. ABSTRACT (Maximum 200 words) A mathematical model and computational code are validated for predicting shallow depth explosion plume behavior. The model is based on a generalized formulation of hydrodynamics and users an incompressible liquid assumption. This formulation is well suited for predicting long-time bubble and plume dynamics. Initial conditions for the model are derived from spherically symmetric bubble theory, combined with empirical measurements. The effects of the spray dome caused by the reflection of the initial shock wave off the free surface is modeled empirically as a recess in the surface above the charge. Comparisons to photographs of experiments provide qualitative agreement. Quantitative measurements of plume heights and plume densities using conductivity probes and microwave absorption are also compared to the computational data. Results for both single- and multiple-charge shots are included.				
14. SUBJECT TERMS two- and three-dimensional codes nonliquid region benchmark computations			15. NUMBER OF PAGES 87	
			16. PRICE CODE	
17. SECURITY CLASSIFICATION OF REPORT UNCLASSIFIED	18. SECURITY CLASSIFICATION OF THIS PAGE UNCLASSIFIED	19. SECURITY CLASSIFICATION OF ABSTRACT UNCLASSIFIED	20. LIMITATION OF ABSTRACT SAR	

GENERAL INSTRUCTIONS FOR COMPLETING SF 298

The Report Documentation Page (RDP) is used in announcing and cataloging reports. It is important that this information be consistent with the rest of the report, particularly the cover and its title page. Instructions for filling in each block of the form follow. It is important to **stay within the lines** to meet **optical scanning requirements**.

Block 1. Agency Use Only (Leave blank).

Block 2. Report Date. Full publication date including day, month, and year, if available (e.g. 1 Jan 88). Must cite at least the year.

Block 3. Type of Report and Dates Covered. State whether report is interim, final, etc. *If applicable, enter inclusive report dates (e.g. 10 Jun 87 - 30 Jun 88).

Block 4. Title and Subtitle. A title is taken from the part of the report that provides the most meaningful and complete information. When a report is prepared in more than one volume, repeat the primary title, add volume number, and include subtitle for the specific volume. On classified documents enter the title classification in parentheses.

Block 5. Funding Numbers. To include contract and grant numbers; may include program element number(s), project number(s), task number(s), and work unit number(s). Use the following labels:

C - Contract	PR - Project
G - Grant	TA - Task
PE - Program Element	WU - Work Unit Accession No.

Block 6. Author(s). Name(s) of person(s) responsible for writing the report, performing the research, or credited with the content of the report. If editor or compiler, this should follow the name(s).

Block 7. Performing Organization Name(s) and address(es). Self-explanatory.

Block 8. Performing Organization Report Number. Enter the unique alphanumeric report number(s) assigned by the organization performing the report.

Block 9. Sponsoring/Monitoring Agency Name(s) and Address(es). Self-explanatory.

Block 10. Sponsoring/Monitoring Agency Report Number. (If Known)

Block 11. Supplementary Notes. Enter information not included elsewhere such as: Prepared in cooperation with...; Trans. of ...; To be published in... . When a report is revised, include a statement whether the new report supersedes or supplements the older report.

Block 12a. Distribution/Availability Statement. Denotes public availability or limitations. Cite any availability to the public. Enter additional limitations or special markings in all capitals (e.g. NOFORN, REL, ITAR).

DOD - See DoDD 5230.24, "Distribution Statements on Technical Documents"
DOE - See authorities.
NASA - See Handbook NHB 2200.2
NTIS - Leave blank

Block 12b. Distribution Code.

DOD - Leave blank.
DOE - Enter DOE distribution categories from the Standard Distribution for Unclassified Scientific and Technical Reports.
NASA - Leave blank.
NTIS - Leave blank.

Block 13. Abstract. Include a brief (*Maximum 200 words*) factual summary of the most significant information contained in the report.

Block 14. Subject Terms. Keywords or phrases identifying major subjects in the report.

Block 15. Number of Pages. Enter the total number of pages.

Block 16. Price Code. Enter appropriate price code (*NTIS only*).

Block 17-19. Security Classifications. Self-explanatory. Enter U.S. Security Classification in accordance with U.S. Security Regulations (i.e., UNCLASSIFIED). If form contains classified information, stamp classification on the top and bottom of this page.

Block 20. Limitation of Abstract. This block must be completed to assign a limitation to the abstract. Enter either UL (unlimited or SAR (same as report). An entry in this block is necessary if the abstract is to be limited. If blank, the abstract is assumed to be unlimited.

NAVAL SEA SYSTEMS COMMAND

